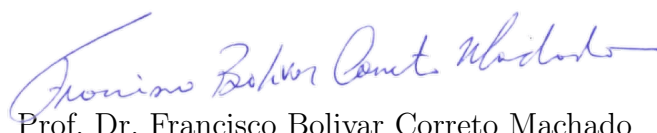


Dissertation presented to the Instituto Tecnológico de Aeronáutica, in partial fulfillment of the requirements for the degree of Master of Science in the Graduate Program of Physics, Field of Atomic and Molecular Physics.

Leonardo dos Anjos Cunha

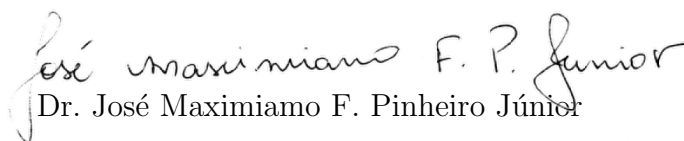
**INTERMOLECULAR INTERACTIONS IN
MOLECULAR MODELS OF POROUS
GRAPHENE: INSIGHTS ON PERMEABILITY
AND SELECTIVITY**

Dissertation approved in its final version by signatories below:



Prof. Dr. Francisco Bolivar Correto Machado

Advisor



Dr. José Maximiano F. Pinheiro Júnior

Co-advisor

Prof. Dr. Pedro Teixeira Lacava

Dean for Graduate Education and Research

Campo Montenegro
São José dos Campos, SP - Brazil
2018

Cataloging-in Publication Data
Documentation and Information Division

dos Anjos Cunha, Leonardo

Intermolecular Interactions in Molecular Models of Porous Graphene: Insights on Permeability and Selectivity / Leonardo dos Anjos Cunha.

São José dos Campos, 2018.

101f.

Dissertation of Master of Science – Course of Physics. Area of Atomic and Molecular Physics – Instituto Tecnológico de Aeronáutica, 2018. Advisor: Prof. Dr. Francisco Bolivar Correto Machado. Co-advisor: Dr. José Maximiano F. Pinheiro Júnior.

1. Grafeno. 2. Forças Intermoleculares. 3. Permeabilidade. 4. Estruturas bidimensionais. 5. Físico-Química. 6. Física. I. Instituto Tecnológico de Aeronáutica. II. Title.

BIBLIOGRAPHIC REFERENCE

DOS ANJOS CUNHA, Leonardo. **Intermolecular Interactions in Molecular Models of Porous Graphene: Insights on Permeability and Selectivity**. 2018. 101f. Dissertation of Master of Science – Instituto Tecnológico de Aeronáutica, São José dos Campos.

CESSION OF RIGHTS

AUTHOR'S NAME: Leonardo dos Anjos Cunha

PUBLICATION TITLE: Intermolecular Interactions in Molecular Models of Porous Graphene: Insights on Permeability and Selectivity.

PUBLICATION KIND/YEAR: Dissertation / 2018

It is granted to Instituto Tecnológico de Aeronáutica permission to reproduce copies of this dissertation and to only loan or to sell copies for academic and scientific purposes. The author reserves other publication rights and no part of this dissertation can be reproduced without the authorization of the author.



Leonardo dos Anjos Cunha
R. Cel. Rafael Tobias, 457
07053-040 – Guarulhos-SP

INTERMOLECULAR INTERACTIONS IN MOLECULAR MODELS OF POROUS GRAPHENE: INSIGHTS ON PERMEABILITY AND SELECTIVITY

Leonardo dos Anjos Cunha

Thesis Committee Composition:

| | | | | |
|-----------|-----------------------------------|---------------------|---|---------|
| Prof. Dr. | Luiz Fernando de Araújo Ferrão | President | - | ITA |
| Prof. Dr. | Francisco Bolivar Correto Machado | Advisor | - | ITA |
| Dr. | José Maximiano F. Pinheiro Júnior | Co-advisor | - | ITA |
| Prof. Dr. | Marcelo Marques | Internal Member | - | ITA |
| Prof. Dr. | Douglas Soares Galvão | External Member | - | UNICAMP |
| Prof. Dr. | Tobias Frederico | Internal Substitute | - | ITA |
| Prof. Dr. | Caetano Rodrigues Miranda | External Substitute | - | USP |

To my beloved parents, Vilmar and
Maria Inês, for their unconditional love
and unwavering support.

Acknowledgments

To my family and friends, who supported and encouraged me whenever I found myself in difficult times. In particular, I should be forever grateful to my parents, Maria Inês and Vilmar, and to my grandmother, Neide, for their love and support at all times.

To Prof. Dr. Francisco Bolivar and Luiz Ferrão, for giving me the opportunity to be part of their research group since my freshmen year and for helpful discussions, advice and uncountable recommendation letters over the last five years. To Prof. Dr. David Sherrill, Dr. Jérôme Gonthier and the members of the Sherrill group at Georgia Tech for granting me the opportunity to learn about the fascinating world of non-covalent interactions and for showing me that it is possible to combine quantum chemistry and computer science to make an extremely rewarding career out of it.

To Dr. José Maximiano for proposing such a challenging and exciting project and also for helping and motivating me to achieve our goals. The insightful long talks, despite keeping me awake sometimes wondering if I was choosing the right path, have helped broadening my perception about science and made me realize how much I love it.

Finally, to every member of the ETER group for their company. In this sense, it is only logical to thank Marcelo and Gabriel, who, despite annoying me all the time, helped me with amazing ideas and interesting discussions over lunch. It was truly hard for them to deal with my “vulcan” personality during the past couple years, but all their patience has finally paid off.

*“Be less curious about people
and more curious about ideas.”*
— MARIE SKŁODOWSKA CURIE

Abstract

Molecular engineering of porous membranes represents the frontier technology in gas separation processes. Owing to its intrinsic single-atomic layer thickness, nanoporous graphene allotropes are a promising class of compounds that fits the requirements for enhanced permeance and selectivity properties towards a specific target. Issues such as control of chemical stability and homogeneity of pore size and density grant an increasing central role to molecular modeling tools to guide the development of more efficient nanoporous devices. Previous works have provided some insight on possible strategies to devise pore structures for specific purposes. Their strategy, despite exploring different aspects such as structural changes, topological modification and functionalization, relied mostly on the influence of an ambiguous definition of pore size.

The main goal of this master dissertation is to shed light into the nature of the diffusion mechanism and, more importantly, understand and quantify the influence of pore size in this process. The novelty of this work relies on the physical decomposition of the total interaction energy between gas molecules and molecular pore structures. To this end, the Symmetry-Adapted Perturbation Theory (SAPT) methodology was explored. Based on this analysis, effects such as electron delocalization, charge distribution and polarization could contribute towards a mechanism that counterbalances the influence of the pore size. A second part of the study consisted on a comparative analysis between SAPT results and energy barriers computed at the density functional theory level. To this end, we have explored the interaction between a pore size and several gas molecules. It is interesting to notice that, for some systems, mixing of orbitals of each monomer might lead to unexpected results due to charge-transfer effects. Finally, we have also applied SAPT to explore the effects of chemical doping as a strategy for tailoring the total interaction energy.

The set of presented analysis aims to provide a meaningful picture posed by the diffusion process, emphasizing the importance of energy decomposition analysis (EDA) methods in order to comprehend such mechanism. The set of investigations present in this work provides a conceptual basis to understand the complex set of intermolecular interactions involved in the sieving process which is essential to promote new guidelines for a rational design of efficient molecular sieves.

List of Figures

| | |
|--|----|
| FIGURE 1.1 – Schematic representation of a graphene pore passivated with hydrogen. Reproduced from (JIANG <i>et al.</i> , 2009). | 21 |
| FIGURE 1.2 – Molecular model of an intrinsic porous graphene allotrope used in the investigation of tunneling effects towards the permeability of He. Reproduced from (SCHRIER, 2010). | 22 |
| FIGURE 1.3 – The sp -hybridized structure of graphdiyne, an experimentally synthesized porous membrane. The shaded area represents the van der Waals surface, showing the effective size of the pore. Reproduced from (JIAO <i>et al.</i> , 2011). | 22 |
| FIGURE 1.4 – Several sp - sp^2 pore structures: (a) graphyne; (b) graphdiyne; (c) rhombic-graphyne; (d) square-octagon layer. The blue regions indicate effective size of each pore. Reproduced from (ZHANG <i>et al.</i> , 2012). | 23 |
| FIGURE 1.5 – Structure of the N-substituted g- C_3N_3 pore, which presents an effective size of 5.46 Å. Reproduced from (MA <i>et al.</i> , 2014). | 24 |
| FIGURE 2.1 – Frequency of the radiation involved in each type of spectroscopy technique described in Table 2.1. Reproduced from (LIBRETEXTS, 2018). | 29 |
| FIGURE 2.2 – Generalized Self Consistent Procedure (SCF) applied to the Hartree-Fock methodology. Reproduced from (CRAMER, 2004). | 32 |
| FIGURE 2.3 – Jacob’s ladder of density functional approximations to the exchange-correlation energy. Reproduced from (PERDEW <i>et al.</i> , 2005). | 34 |

- FIGURE 2.4 – Basis set superposition error. (a) At large distances, the monomers A and B are isolated and their basis functions hardly overlap. (b) As the monomers get closer to each other, overlap increases and some of the functions centering on B start to be also available to describe A. (c) With a more complete set of functions, A is better described at closer distances and the interaction energy of the system is over-stabilized due to this artificial effect. 36
- FIGURE 2.5 – Composition of several levels of SAPT, explicitly showing the truncation order of the perturbation series for both intramolecular correlation and the intermolecular potential. In this work, we will attain to the SAPT0 level. Reproduced from (PARKER *et al.*, 2014). 38
- FIGURE 2.6 – Non-Covalent Index plot of RDG versus density for isolated systems. Reproduced from (JOHNSON *et al.*, 2010). 40
- FIGURE 2.7 – Non-Covalent Index plot of RDG versus density for interacting systems. Reproduced from (JOHNSON *et al.*, 2010). 40
- FIGURE 2.8 – Summary of the interpretation of the Non-Covalent Index analysis. Reproduced from (LU; CHEN, 2012). 41
- FIGURE 2.9 – Distances for the potential energy surfaces. 42
- FIGURE 3.1 – Model systems for the analysis of the H₂ diffusion through porous graphene-based pores: (a) C₂-square structure, which presents a circular pore with a C···C diameter of 5.45 Å; (b) C₂-pent structure, which presents a slightly distorted circular pore whose C···C diameter is 5.47 Å for axis highlighted in blue and 5.32 Å for other in red; (c) One-dimensional path to compute the total interaction energy between the pore system and hydrogen gas. 45
- FIGURE 3.2 – Total interaction energy computed at the SAPT0/jDZ level of theory for the C₂-square···H₂ (blue) and C₂-pent···H₂ (red) systems. . . . 46
- FIGURE 3.3 – Components of the total interaction energy for the systems C₂-square···H₂ (blue) and C₂-pent···H₂ (red): (a) Component of the interaction energy due to intermolecular exchange; (b) Component of the interaction energy due to electrostatics; (c) Component of the interaction energy due to induction; (d) Component of the interaction energy due to dispersion. 47

- FIGURE 3.4 – Electrostatic potential map (ESP) and π component of the electron localization function (ELF_π) descriptions of both pore structures. The isovalues used to plot both isosurfaces were, respectively, 0.02 and $0.6 \text{ e}\text{\AA}^{-3}$. For the electrostatic potential maps, regions in blue and red indicate, respectively, areas that generate a lower and higher electric potential: (a) ESP for C_2 -square; (b) ELF_π for C_2 -square; (c) ESP for C_2 -pent; (d) ELF_π for C_2 -pent. 49
- FIGURE 3.5 – Topological analysis for the interaction of C_2 -square with H_2 at a distance of 5 \AA : (a) Plot of the reduced density gradient (s); (b) Reduced Density Gradient Isosurface (cutoff of 0.5 e Bohr^{-3}); (c) Isosurface (cutoff of $0.0005 \text{ e Bohr}^{-3}$) of the density difference between the complexes and the two isolated systems. Blue and red regions indicate density gain and loss, respectively, in comparison to the isolated system. 50
- FIGURE 3.6 – Topological analysis for the interaction of C_2 -square with H_2 at a distance of 2.6 \AA : (a) Plot of the reduced density gradient (s); (b) Reduced Density Gradient Isosurface (cutoff of 0.5 e Bohr^{-3}); (c) Side view of the isosurface (cutoff of $0.0005 \text{ e Bohr}^{-3}$) of the density difference between the complexes and the two isolated systems; (d) Top view of the isosurface (cutoff of $0.0005 \text{ e Bohr}^{-3}$) of the density difference between the complexes and the two isolated systems. Blue and red regions indicate density gain and loss, respectively, in comparison to the isolated system. 51
- FIGURE 3.7 – Topological analysis for the interaction of C_2 -square with H_2 at a distance of 0.0 \AA : (a) Plot of the reduced density gradient (s); (b) Reduced Density Gradient Isosurface (cutoff of 0.5 e Bohr^{-3}); (c) Side view of the isosurface (cutoff of $0.001 \text{ e Bohr}^{-3}$) of the density difference between the complexes and the two isolated systems; (d) Top view of the isosurface (cutoff of $0.001 \text{ e Bohr}^{-3}$) of the density difference between the complexes and the two isolated systems. Blue and red regions indicate density gain and loss, respectively, in comparison to the isolated system. 52
- FIGURE 3.8 – Isosurface (cutoff of 0.5 e Bohr^{-3}) of the NCI index for the C_2 -pent $\cdots\text{H}_2$ complex when the monomers are separated by 5.0 \AA . . . 53

| | |
|---|----|
| FIGURE 3.9 – Analysis of the polarization of the electron density as a function of the separation distance between C ₂ -pent and H ₂ : (a) Separation of 2.6 Å; (b) Separation of 0.0 Å. The isovalue used was 0.001 e Bohr ⁻³ . Blue and regions regions indicate density gain and loss, respectively, in comparison to the isolated systems. | 54 |
| FIGURE 3.10 –H ₂ permeance versus temperature for C ₂ -square (blue) and C ₂ -pent pores (red). The dashed line represents the industrially acceptable permeance for gas separation with a separability of 6 (ZHU, 2006). | 55 |
| FIGURE 4.1 – The kekulene (C ₂) pore structure, with its internal H-H distance of 3.64 Å. | 56 |
| FIGURE 4.2 – C-C bond length of the C ₂ structure relative to 1.4 Å. Blue (red) regions indicate larger (shorter) bond when compared to the benzene resonant C-C bond length. | 57 |
| FIGURE 4.3 – C ₂ ⋯Ar Potential Energy Surface calculated at different methodologies. | 58 |
| FIGURE 4.4 – C ₂ ⋯Ar Potential Energy Surface around the minimum well region. | 59 |
| FIGURE 4.5 – C ₂ ⋯Ar SAPT0 and energy components PES | 60 |
| FIGURE 4.6 – C ₂ ⋯Ar total dipole moment computed with PBE0+vdW | 60 |
| FIGURE 4.7 – Interaction energy for the C ₂ ⋯Ar system using different schemes for the dispersion contribution. | 61 |
| FIGURE 4.8 – A closer look at the minimum well region of the potential energy surface of the total interaction energy for the C ₂ ⋯Ar system using different schemes for the dispersion contribution. | 62 |
| FIGURE 4.9 – C ₂ ⋯Ne Potential Energy Surface calculated at different methodologies. | 63 |
| FIGURE 4.10 –C ₂ ⋯Ne Potential Energy Surface around the minimum well region (2.5 Å). | 64 |
| FIGURE 4.11 –C ₂ ⋯Ne SAPT0 and energy components PES. | 65 |
| FIGURE 4.12 –C ₂ ⋯He Potential Energy Surface calculated at different methodologies | 66 |
| FIGURE 4.13 –C ₂ ⋯He minimum well around the 2.5 Åregion of the PES | 66 |
| FIGURE 4.14 –C ₂ ⋯He SAPT0 and energy components PES. | 67 |

| | |
|---|----|
| FIGURE 4.15 – $C_2 \cdots H_2$ Potential Energy Surface calculated at different methodologies. | 69 |
| FIGURE 4.16 – $C_2 \cdots H_2$ minimum well around the 2.5 Å region of the PES. | 69 |
| FIGURE 4.17 – $C_2 \cdots H_2$ SAPT0 and energy components PES. | 70 |
| FIGURE 4.18 – $C_2 \cdots N_2$ Potential Energy Surface calculated at different methodologies. | 71 |
| FIGURE 4.19 – $C_2 \cdots N_2$ minimum well around the 2.5 Å region of the PES. | 72 |
| FIGURE 4.20 – $C_2 \cdots N_2$ SAPT0 and energy components PES. | 72 |
| FIGURE 4.21 – ω B97X-D/jun-cc-pVDZ density of states (DOS) diagram of the $C_2 \cdots N_2$ system and its projection on the N_2 orbitals. | 74 |
| FIGURE 4.22 –SAPT0/jun-cc-pVDZ charge-transfer energy as a function of the distance for the $C_2 \cdots N_2$ system and the LUMO of the dimer at two different distances. | 74 |
| FIGURE 4.23 – ω B97X-D/jun-cc-pVDZ isosurfaces (cutoff of 0.001 e Bohr ⁻³) density difference between the $C_2 \cdots N_2$ and the two monomers: (a) $z = 2.8$ Å; (b) $z = 0.0$ Å. Blue regions indicate a density gain and red regions indicate a density loss. | 75 |
| FIGURE 4.24 –Charge distribution on the z-axis as a function of the separation between monomers for the $C_2 \cdots N_2$ system. The ω B97X-D density was used in order to calculate these charge distributions. | 76 |
| FIGURE 4.25 –HOMO-LUMO gap (in eV) as a function of the separation between the two monomers for the C_2 structure interacting with different gas molecules. | 77 |
| FIGURE 4.26 – $C_2 \cdots CO_2$ Potential Energy Surface calculated with different methodologies. | 78 |
| FIGURE 4.27 – $C_2 \cdots CO_2$ minimum well around the 3.0 Å region of the PES. | 78 |
| FIGURE 4.28 – $C_2 \cdots CO_2$ SAPT0 and energy components PES. | 79 |
| FIGURE 5.1 – Structures for the N-substituted pores based on the kekulene (C_2 backbone): (a) Substitution on the external edge (C_2-N_{ext}); (b) Substitution on the internal edge (C_2-N_{int}); (c) Substitution on both edges (C_2-NN). | 82 |
| FIGURE 5.2 – Total interaction energy between H_2 and the N-substituted pores | 82 |

- FIGURE 5.3 – Components of the total interaction energy for the B-substituted systems: (a) Component of the interaction energy due to intermolecular exchange; (b) Component of the interaction energy due to electrostatics; (c) Component of the interaction energy due to induction; (d) Component of the interaction energy due to dispersion. 83
- FIGURE 5.4 – NCI analysis for the C_2 pore structure at different separation distances between the monomers: (a) NCI plot for a distance of 5.0\AA ; (b) NCI isosurface for a distance of 5.0\AA ; (c) NCI plot for a distance of 2.6\AA ; (d) NCI isosurface for a distance of 2.6\AA ; (e) NCI plot for a distance of 0.0\AA ; (f) NCI isosurface for a distance of 0.0\AA 85
- FIGURE 5.5 – NCI analysis for the C_2 -NN pore structure at different separation distances between the monomers: (a) NCI plot for a distance of 5.0\AA ; (b) NCI isosurface for a distance of 5.0\AA ; (c) NCI plot for a distance of 2.6\AA ; (d) NCI isosurface for a distance of 2.6\AA ; (e) NCI plot for a distance of 0.0\AA ; (f) NCI isosurface for a distance of 0.0\AA . 86
- FIGURE 5.6 – Density difference isosurfaces for a separation distance of 0.0\AA between the pore and the gas: (a) C_2 pore system; (b) C_2 -NN pore system. 87
- FIGURE 5.7 – Density difference isosurfaces for a separation distance of 5.0\AA between the pore and the gas: (a) C_2 pore system; (b) C_2 -NN pore system. 87
- FIGURE 5.8 – Structures for the B-substituted pores based on the kekulene (C_2 backbone): (a) Substitution on the external edge (C_2 - B_{ext}); (b) Substitution on the internal edge (C_2 - B_{int}); (c) Substitution on both edges (C_2 -BB). 88
- FIGURE 5.9 – Total interaction energy between H_2 and the B-substituted pores . . 89
- FIGURE 5.10 – Components of the total interaction energy for the B-substituted systems: (a) Component of the interaction energy due to intermolecular exchange; (b) Component of the interaction energy due to electrostatics; (c) Component of the interaction energy due to induction; (d) Component of the interaction energy due to dispersion. 90

| | |
|--|----|
| FIGURE 5.11 –Structures for the BN-substituted pores based on the kekulene (C_2 backbone): (a) B-substitution on the external edge and N-substitution on the internal edge (C_2 -BN); (b) N-substitution on the external edge and B-substitution on the internal edge (C_2 -NB); (c) Alternated BN-substitution on external edge (C_2 -BN ^{alt} _{ext}); (d) Alternated BN-substitution on internal edge (C_2 -BN ^{alt} _{int}); (e) Alternated BN-substitution on both edges (C_2 -BN ^{alt}). | 91 |
| FIGURE 5.12 –Total interaction energy between H_2 and the BN-substituted pores . | 92 |
| FIGURE 5.13 –Components of the total interaction energy for the BN-substituted systems: (a) Component of the interaction energy due to intermolecular exchange; (b) Component of the interaction energy due to electrostatics; (c) Component of the interaction energy due to induction; (d) Component of the interaction energy due to dispersion. | 92 |

List of Tables

| | |
|---|----|
| TABLE 2.1 – Commonly used spectroscopic techniques, the type of electromagnetic radiation involved, as well as the type of matter which can be observed. | 28 |
| TABLE 2.2 – Regions and respective behaviors used in the Non-Covalent Index Analysis. The cells describe the range of values that each property (density, gradient and reduced gradient) could assume in a specific region. | 39 |
| TABLE 4.1 – Summary for the interaction energy between C ₂ and Ar: diffusion energy barrier (ΔE_{diff}), minimum well position (r_{vdW}) and minimum well depth (ΔE_{vdW}) | 62 |
| TABLE 4.2 – Summary for the interaction energy between C ₂ and Ne: diffusion energy barrier (ΔE_{diff}), minimum well position (r_{vdW}) and minimum well depth (ΔE_{vdW}) | 65 |
| TABLE 4.3 – Summary for the interaction energy between C ₂ and He: diffusion energy barrier (ΔE_{diff}), minimum well position (r_{vdW}) and minimum well depth (ΔE_{vdW}) | 68 |
| TABLE 4.4 – Summary for the interaction energy between C ₂ and H ₂ : diffusion energy barrier (ΔE_{diff}), minimum well position (r_{vdW}) and minimum well depth (ΔE_{vdW}) | 70 |
| TABLE 4.5 – Summary for the interaction energy between C ₂ and N ₂ : diffusion energy barrier (ΔE_{diff}), minimum well position (r_{vdW}) and minimum well depth (ΔE_{vdW}) | 73 |
| TABLE 4.6 – Summary for the interaction energy between C ₂ and CO ₂ : diffusion energy barrier (ΔE_{diff}), minimum well position (r_{vdW}) and minimum well depth (ΔE_{vdW}) | 79 |

| | |
|---|----|
| TABLE 6.1 – Summary for the SAPT0/jDZ interaction energy between C_2 and different gas molecules: diffusion energy barrier (ΔE_{diff}), minimum well position (r_{vdW}) and minimum well depth (ΔE_{vdW}) | 94 |
|---|----|

Contents

| | | |
|-------|---|----|
| 1 | INTRODUCTION | 19 |
| 1.1 | Overview of previous studies | 20 |
| 1.2 | Objectives and Structure | 24 |
| 2 | THEORETICAL BACKGROUND | 27 |
| 2.1 | Theoretical Discussion | 27 |
| 2.1.1 | The Born-Oppenheimer Approximation | 27 |
| 2.1.2 | The many-electron problem - Wavefunction Approach | 28 |
| 2.1.3 | The many electron problem - Density Approach | 33 |
| 2.1.4 | Supramolecular approach | 35 |
| 2.1.5 | Intermolecular Forces | 35 |
| 2.1.6 | Symmetry-Adapted Perturbation Theory - SAPT | 37 |
| 2.1.7 | Visualizing Non-Covalent Interactions (NCI) | 37 |
| 2.2 | Computational Details | 41 |
| 3 | UNRAVELING THE IMPORTANCE OF PORE SIZE | 43 |
| 3.1 | Motivation | 43 |
| 3.2 | C ₂ -square and C ₂ -pent Structure | 44 |
| 3.3 | Diffusion Energy Barrier | 44 |
| 3.4 | Physical Decomposition of the Interaction Energy | 45 |
| 3.5 | NCI and Density Analysis of the Interaction | 48 |
| 3.5.1 | C ₂ -square | 48 |
| 3.5.2 | C ₂ -pent | 52 |
| 3.6 | Permeance and Selectivity | 53 |

| | | |
|-------|---|-----|
| 4 | BARRIER HEIGHT AND DFT FLAVORS | 56 |
| 4.1 | Kekulene Structure | 56 |
| 4.2 | Interaction with gas molecules | 56 |
| 4.2.1 | $C_2 \cdots Ar$ | 57 |
| 4.2.2 | $C_2 \cdots Ne$ | 63 |
| 4.2.3 | $C_2 \cdots He$ | 64 |
| 4.2.4 | $C_2 \cdots H_2$ | 68 |
| 4.2.5 | $C_2 \cdots N_2$ | 71 |
| 4.2.6 | $C_2 \cdots CO_2$ | 76 |
| 5 | CHEMICAL DOPING | 80 |
| 5.1 | Motivation | 80 |
| 5.2 | Nitrogen substituted structures | 81 |
| 5.3 | Boron substituted structures | 84 |
| 5.4 | Mixed BN substituted structures | 89 |
| 6 | CONCLUSIONS | 93 |
| | BIBLIOGRAPHY | 96 |
| | ANNEX A – PUBLISHED WORKS | 101 |

1 Introduction

Gas separation plays a key role in various industrial processes. For instance, excess CO_2 has to be removed to meet pipeline and heating value specifications in the natural gas sweetening (LIU *et al.*, 2015). Moreover, one of the most challenging environmental issues is related to the proposal of efficient techniques to separate the components of a N_2/CO_2 mixture, also known as “flue gas”. This is an important way to tackle global climate change and curb the carbon footprint of electricity generated by coal-fired power plants (ROCHELLE, 2009). Furthermore, the growing demand for hydrogen production, as it is considered a potential source of clean energy has been appealing to development of efficient gas purification methods. From aerospace application as liquid fuel of space shuttles, to power more common appliances as efficient fuel-cells, one should recognize the importance of hydrogen gas as effective energy source nowadays.

Given the scenario described above, finding an effective and low-cost strategy for gas purification represents an important economical challenge. In this context, membrane separation is viewed as the outstanding method due to convenience of operation, energy saving and environmentally friendly (JIAO *et al.*, 2013). It is known that the permeability of a membrane is inversely proportional to its thickness (OYAMA *et al.*, 2004) and multi-layer membrane could present a permeance 10 to 100 times lower than “single-layer” membranes. Therefore, development of an “ultraphin” and selective membrane is highly expected for gas separation. Our contribution in this direction is to propose possible guidelines, based on an extensive and detailed theoretical analysis of molecular electronic structure properties, for the engineering of new nanoscale membrane structures that could be used to separate the components of a gaseous mixture.

Graphene is a two-dimensional material consisting of a sp^2 -hybridized carbon network which presents unique chemical, electronic and mechanical properties. Despite being a good candidate for gas separation due to its single atomic layer structure, pristine graphene membranes are impermeable even to small gas molecules, due to the delocalized π system responsible for Pauli repulsion in hollow sites (LEENAERTS *et al.*, 2008). Hence, the need of nanoporous graphene structures appears as a natural consequence in order to tackle the problem of gas separation through membranes. Synthetic strategies to create porous graphene membranes have already been developed, encompassing top-down approaches

such as heavy ion bombardment or focused electron beams to "drill holes" and bottom-up techniques based on molecular assembling (BUNCH *et al.*, 2008; FISCHBEIN; DRNDIĆ, 2008). However, experimental control of pore size and pore density poses a challenge to achieve efficient structures, thus increasing their cost and complexity. Theoretically, there is much more flexibility in devising possible nanoporous structures based on the graphene lattice. In this sense, understanding the complex set of intermolecular interactions that take place during the diffusion process might be accomplished by computational tools, such as density functional theory (DFT) or molecular dynamics (MD). Moreover, theoretical studies also provide insightful data on aspects concerning reactivity and stability of the compounds, thus serving as powerful guidelines for the experimental synthesis of nanoporous membranes. In this sense, several strategies, ranging from functionalization to topological changes have already been devised by theoreticians in order to propose membranes with enhanced selectivity and permeability for a given target gas molecule. These previously reported investigations will be discussed in detail on the next section.

1.1 Overview of previous studies

Sint and co-workers carried out classical molecular dynamics (CMD) simulations to analyze the diffusion mechanism of hydrated ions through two functionalized graphene nanopores (SINT *et al.*, 2008). The study pointed out that F-N terminated pores were more selective towards cations such as Li^+ , Na^+ and K^+ , whereas H-terminated pores were only passed by Cl^- and Br^- anions. Despite the lack of a systematic discussion about how pore size and/or structure could lead to such observations, this was the first study that highlighted the viability of nanoporous systems based on graphene allotropes as separation membranes.

The first study combining information of the electronic structure from periodic DFT calculations with statistical analysis from CMD simulations was presented later by Jiang and co-workers (JIANG *et al.*, 2009). In this work, the influence of pore structure on diffusion barriers through nanoporous graphene and their selectivity for gas molecules such as H_2 and CH_4 were analyzed. The estimated selectivity ratio between H_2 and CH_4 for a fully hydrogen-passivated pore (Figure 1.1) was found to be 10^{23} .

After the seminal paper published by Jiang, several other studies were carried out using similar methodologies. For instance, water transport through ultraphin porous graphene membranes was analyzed by Suk and co-workers (SUK; ALURU, 2010). Based on molecular dynamics simulations, the water flux through porous graphene with diameters ranging from 0.75 to 2.75 nm was compared with that of carbon nanotubes (CNT) membranes of different thicknesses. The conclusion is that, for small pore diameters, the efficiency

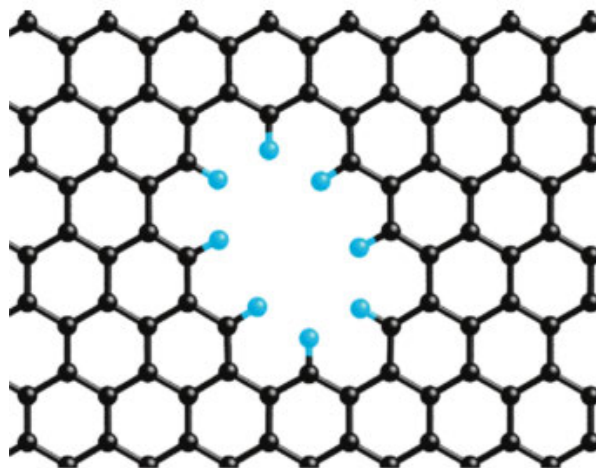


FIGURE 1.1 – Schematic representation of a graphene pore passivated with hydrogen. Reproduced from (JIANG *et al.*, 2009).

of graphene membranes towards water transport is compromised and CNT membranes would be preferable in this scenario.

Blankenburg and co-workers reported the first work on the estimation of selectivities and permeances of a porous graphene membrane towards a set of 9 gas molecules (BLANKENBURG *et al.*, 2010). Density Functional Theory simulations were conducted in a periodic cell to obtain interaction energies between the gas molecules and the planar membrane. These barriers were used as input in the Arrhenius equation to estimate diffusion rates. The determined separabilities for hydrogen and helium range from 10^3 up to 10^{23} at room temperature with a permeance larger than $10^{-6} \text{ m}^{-2} \text{ s}^{-1} \text{ Pa}^{-1}$ and are superior to those of classical membranes.

To accurately describe the potential energy surfaces involving the gas permeation through a pore system, Schrier and co-workers reported the first theoretical study applying the correlated wavefunction method MP2 to a finite molecular model of porous graphene with fixed geometry (SCHRIER, 2010). Comparing quantum and classical approaches to estimate the transmission rate through the pore (Figure 1.2), the authors came to the conclusion that quantum effects such as tunneling play a major role in the permeability of helium through the pore. However, these effects were found to be insufficient to achieve practical He isotope separation. Despite the importance of the study proposed by Schrier, it did not focus on finding an explanation for the origin of the high selectivity of the pore towards Helium gas. By comparing the electron density distribution of the same polyphenylene pore system, Li and coworkers argued this structure could also be used for H_2 separation (LI *et al.*, 2010b).

All the paper reviewed so far presented porous membranes that were based on a sp^2 backbone structure similar to graphene. Jiao and co-workers proposed a sp -hybridized carbon lattice called graphdiyne (Figure 1.3) (JIAO *et al.*, 2011), which has already been

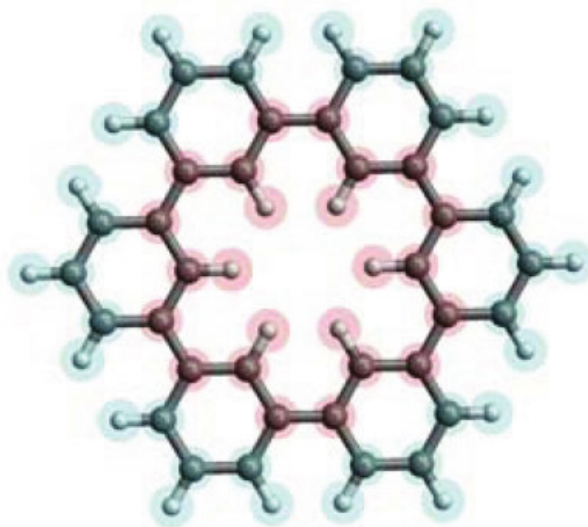


FIGURE 1.2 – Molecular model of an intrinsic porous graphene allotrope used in the investigation of tunneling effects towards the permeability of He. Reproduced from (SCHRIER, 2010).

successfully synthesized via cross-linking reaction on top of copper surface (LI *et al.*, 2010a). Analyzing the electronic structure of the periodic membrane and the energy results with the hybrid exchange-correlation functional HSE06, the authors were able to compute diffusion rates and selectivity using the Arrhenius equation as a function of temperature for H_2 , CO and CH_4 .

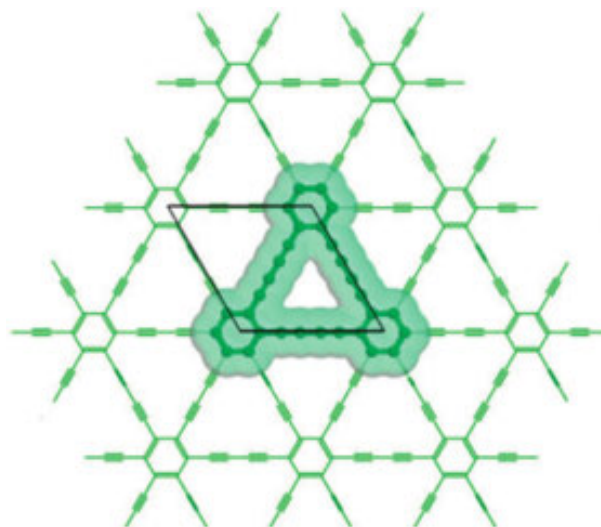


FIGURE 1.3 – The sp-hybridized structure of graphdiyne, an experimentally synthesized porous membrane. The shaded area represents the van der Waals surface, showing the effective size of the pore. Reproduced from (JIAO *et al.*, 2011).

An extension of the previous work was proposed by Zhang and co-workers as shown in Figure 1.4 (ZHANG *et al.*, 2012). Four structures based on sp-sp² network with pore size

ranging from 3.38 to 5.42 Å were based on periodic DFT computations. Notwithstanding the standard methodology used to compute interaction energies and diffusion rates between gas molecules and different pore structures, the importance of this work relies on the proposal of an exponential relation between pore size and diffusion energy barrier. Moreover, the authors argue that two pores of those proposed (graphdiyne and rhombic-graphyne) presented reasonable permeability and high selectivity towards H_2 .

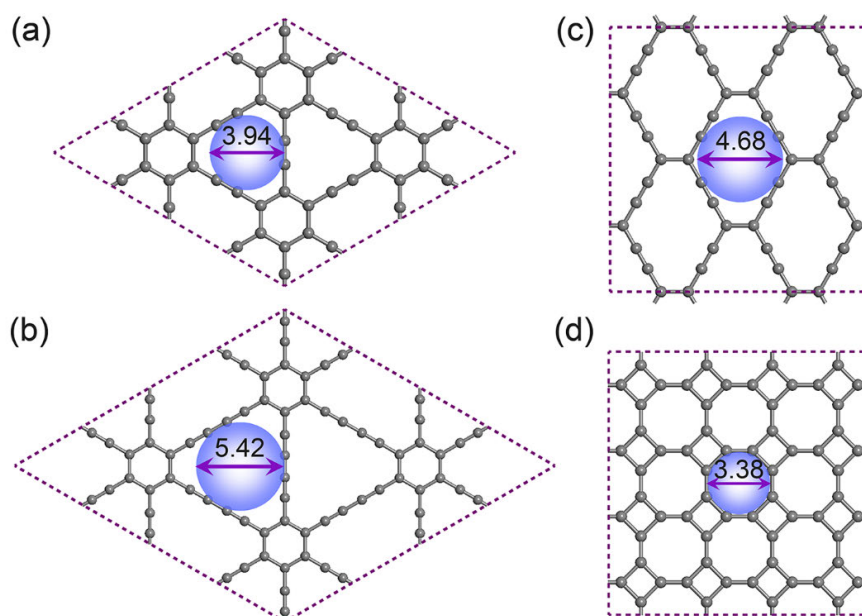


FIGURE 1.4 – Several sp - sp^2 pore structures: (a) graphyne; (b) graphdiyne; (c) rhombic-graphyne; (d) square-octagon layer. The blue regions indicate effective size of each pore. Reproduced from (ZHANG *et al.*, 2012).

Most of the work presented by now focused on the role of pore size for structures based on carbon atoms only. What would happen if a few carbon atoms were exchanged by nitrogen atoms? A study proposed by Ma and co-workers tackled this question (MA *et al.*, 2014). Using a porous membrane named $g-C_3N_3$, which has also been realized experimentally, (see Figure 1.5), the authors investigated how charge partitioning on the atoms of the pore could influence selectivity parameters towards different gas molecules. The results also suggest that the diffusion energy barrier for Hydrogen gas would be smaller for this pore structure when compared to the polyphenylene monolayer from Schrier *et al.*

Several other studies followed the previous described ones and also proposed other types of pore structures (TAO *et al.*, 2014; AMBROSETTI; SILVESTRELLI, 2014; YANG *et al.*, 2016; ZHU *et al.*, 2015b; JIAO; XU, 2015; WANG *et al.*, 2016a; WANG *et al.*, 2016b). While providing a relevant and insightful collection of data about the electronic structure of the pores and diffusion rates for a wide range of gas molecules, these studies are still quite restricted to a common methodology, *i.e.*, Density Functional Theory and Molecular

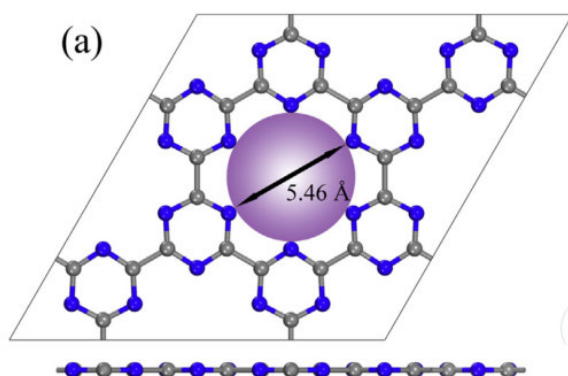


FIGURE 1.5 – Structure of the N-substituted g-C₃N₃ pore, which presents an effective size of 5.46 Å. Reproduced from (MA *et al.*, 2014).

Dynamics. Moreover, it is worth pointing out that there are only a few studies that use the molecular approach to study such systems.

To the best of our knowledge, there has not been reported in the literature any study that investigates the underlying physical mechanisms involved in the interaction barriers between gas molecule and pore structure. Relevant questions such as “what is the most relevant intermolecular force acting between the two systems?” remain unanswered, even though most reported results use van der Waals (vdW) corrected functionals to perform their computations. In spite of the efforts to analyze in depth how and why gas molecules would diffuse through different proposed membranes, it has to be noted that few remarks are made about the interplay between pore structure and its chemical affinity towards a specific molecule. Finally, a last question still to be addressed concerns the role played by the structural deformation of the pore when gas molecules approach it. None of the papers presented previously described the influence of the deformation effects on the profile of the potential energy surfaces related to the interaction of the membrane with the approaching systems.

Thus, the detailed analysis of the aforementioned questions should provide insights for the proposal of new gas-specific porous membranes designed at the molecular and atomic levels.

1.2 Objectives and Structure

The goal of this work is to understand how different porous graphene membranes could be used to separate different components of gaseous or even aqueous solutions. As stated previously, although several studies tried to cover the same subject, there are some questions that remain unanswered.

For instance, even considering several different π networks, none of the reported studies

focused specifically on the influence of the π -electron arrangement and its response to the interaction with a gas specie for structures having almost the same pore size. In particular, this approach could put into evidence how important are the effects of intermolecular interactions compared to pore size in the permeation process. The main purpose of the present study is to highlight such problems and find an explanation for them based on the analysis of which intermolecular forces play the most relevant role on the interaction of the membrane and the approaching systems.

To summarize the ideas presented in last sections, the objectives of the present work are as follows:

- Study different structures that could be used as a porous membrane
- Analyze the intermolecular energy components (electrostatic, exchange, induction and dispersion) that are the most relevant to the interaction of the pore with the approaching molecule/ion.
- Understand the interplay between these intermolecular energy components to physical observables, such as the molecular electrostatic potential and polarizabilities.
- Use concepts of chemical topology, such the electron localization function (ELF) and non-covalent index (NCI), to comprehend the behavior of the electron density and how it is related to the energy decomposition analysis.

In order to achieve the goals stated above, this work will be divided into the following six chapters. On chapter 2, the methodology employed in the study will be discussed. After a brief discussion about the general theory of intermolecular forces, Symmetry-Adapted Perturbation Theory (SAPT) will be presented as a possible way to break down the different energy components related to the interaction of two systems. Special attention will be given to the dispersion component of the interaction energy and how it could be calculate from *ab initio* methods or from empirical parameters, such as the D3 approach by Grimme. To asses the validity of SAPT in our calculations, the results will be compared to Density Functional Theory (DFT) applied to molecular systems.

Chapter 3 contains the mains results concerning the importance of pore size towards the diffusion process of H_2 . Here, we discuss how two different pore topologies but with similar pore sizes could lead to different diffusion energy barriers due to subtleties on their electron density distribution. These features are thoroughly analyzed by means of the concepts borrowed from chemical topology. The electron localization function and the non-covalent index (NCI) are complementary analysis that illustrates how knowledge of the chemical structure of a given pore could give us valuable insight on how such structure would polarize during the diffusion process.

On chapter 4, a comparison between SAPT and DFT results will be drawn. The idea is to study the chemical affinity aspect of the diffusion process from the perspective of the target gas molecule. In this sense, the potential energy surfaces will be computed for six approaching systems: Ar, Ne, He, H₂, N₂ and CO₂. The role of different schemes for dispersion corrections will be analyzed. Finally, for the system involving the N₂ molecule, an investigation about charge-transfer effects between the gas molecule and the pore system will also be presented.

The effects concerning chemical doping on the diffusion of H₂ through a given pore will be described on chapter 5. Three different substitution schemes have been proposed: carbon atoms on both edges of a given pore system were exchanged by nitrogen only, boron only and both centers. In this chapter, we show that it is possible to tune the diffusion energy barrier by choosing the appropriate doping scheme. Finally, chapter 6 contains the conclusions to the present work, as well as a brief overview of the next steps.

2 Theoretical Background

2.1 Theoretical Discussion

2.1.1 The Born-Oppenheimer Approximation

Quantum Mechanics is a groundbreaking theory to describe the dynamical evolution of particles in a microscopic level. It associates a mathematical operator to which observable quantity and the uncertainty principle is intrinsic to the mathematics associated to such operators. Therefore, instead of specifying the state of a system by its position and momenta, the state of quantum-mechanical system is completely specified by a function $\Psi(\mathbf{r}, t)$, where \mathbf{r} is the collection of the positions of all particles (electrons and nuclei) of the system. Such function is called *wavefunction*. Since we are not interested in the dynamics associated to the development of such wavefunction, one has to solve the time-independent Schrödinger equation (Equation. 2.1, where \mathbf{R} and \mathbf{r} indicate, respectively, the collection of the positions of all nuclei and all electrons) in order to obtain the stationary states.

$$\hat{H}\Psi(\mathbf{R}, \mathbf{r}) = E_{total}\Psi(\mathbf{R}, \mathbf{r}) \quad (2.1)$$

The Hamiltonian operator (Equations 2.2 and 2.3) is completely known since all particles interact through a Coulomb potential, and it involves terms that depends on the position of the nuclei and the electrons. Due to the nuclei-electron potential term, Equation 2.1 is not separable and, formally, $\Psi(\mathbf{R}, \mathbf{r})$ can not be written as a product of two functions depending only on \mathbf{R} and \mathbf{r} . Nonetheless, spectroscopy indicates a possible way from which one could approximate the behavior of the quantum-mechanical state of the system. Due to the huge energy difference associated to the dynamics of nuclei and electrons (see Table 2.1 and Figure 2.1) and the fact that the nuclei are much more massive than the electrons allows us to draw the following picture: the timescale for the rearrangement of the electrons due to a change of the configuration of the nuclei is almost instantaneous. In this sense, the electronic motion is determined by the field generated at each “clamped” nuclei configuration. This is the basis of the so called Born-Oppenheimer (BO) approximation. Mathematically, such approximation implies that the total wave-

function of the system can be decoupled into its electronic and nuclear (translational, vibrational and rotational) components, $\Psi(\mathbf{R}, \mathbf{r}) \approx \chi(\mathbf{R})\psi(\mathbf{r}; \mathbf{R})$, where $\chi(\mathbf{R})$ represents the wavefunction that describes the behavior of the nuclei and $\psi(\mathbf{r}; \mathbf{R})$ is the electronic wavefunction parametrized by a given set of nuclear coordinates. Therefore, in the framework of the BO approximation, the problem is now decomposed into two: one is related to the solution of the electronic Schrödinger equation for each clamped (parametric) nuclear configuration and then solve the nuclear part by considering the potential energy surface obtained at the electronic part. Our main effort in this study is to solve the electronic problem and understand the effects of the molecular electronic structure on features such as permeability, selectivity and intermolecular interactions of nanoporous membranes based on graphene allotropes.

$$\hat{H} = \sum_A^{nuc} -\frac{1}{2M_A} \nabla_A^2 + \sum_i^{elec} -\frac{1}{2} \nabla_i^2 + \sum_A \sum_{B < A} \frac{1}{|R_A - R_B|} + \sum_i \sum_{j < i} \frac{1}{|r_i - r_j|} - \sum_A \sum_i \frac{1}{|r_i - R_A|} \quad (2.2)$$

$$\hat{H} = \hat{T}_{nuc} + \hat{T}_{elec} + \hat{V}_{nuc-nuc} + \hat{V}_{elec-elec} + \hat{V}_{nuc-elec} \quad (2.3)$$

TABLE 2.1 – Commonly used spectroscopic techniques, the type of electromagnetic radiation involved, as well as the type of matter which can be observed.

| Technique | Radiation | Matter Observed |
|---------------------------|-------------------------|-------------------------------------|
| NMR Spectroscopy | Radiowaves | Nuclear Structure |
| IR Spectroscopy | Infrared | Molecular Rovibrational Transitions |
| UV-VIS Spectroscopy | Ultraviolet and Visible | Electronic Excitations |
| Fluorescence Spectroscopy | Ultraviolet and Visible | Electronic Transitions |
| X-Ray Crystallography | X-rays | Electronic Densities |

2.1.2 The many-electron problem - Wavefunction Approach

The main goal of electronic structure theory is to solve the electronic part of the Schrödinger equation of a problem with N electrons and N_{atoms} nuclei (Equation 2.4 and Equation 2.5). With the exception of a few systems (one-electron systems), this equation can not be solved exactly and several numerical approaches have already been devised for this purpose. A starting point approximation to solve the many-electron problem is Hartree-Fock theory (HF). Although a complete and formal derivation of the Hartree-Fock theory might be found in (SZABO; OSTLUND, 1996), we should highlight some of the main points that will help us draw some of the analysis presented on the next chapter of this

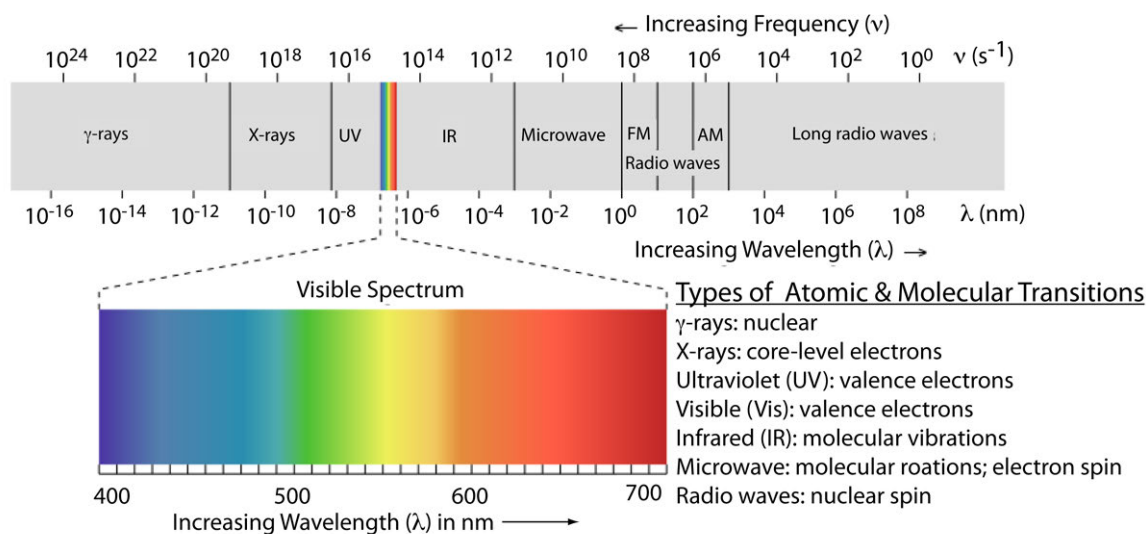


FIGURE 2.1 – Frequency of the radiation involved in each type of spectroscopy technique described in Table 2.1. Reproduced from (LIBRETEXTS, 2018).

work.

$$\hat{H}_{elec}\psi(r_1, r_2, \dots, r_N; \mathbf{R}) = E_{elec}(\mathbf{R})\psi(r_1, r_2, \dots, r_N; \mathbf{R}) \quad (2.4)$$

$$\hat{H}_{elec} = \sum_{i=1}^N -\frac{1}{2}\nabla_i^2 + \sum_{A=1}^{N_{atom}} \sum_{j=1}^N \frac{Z_A}{r_{Ai}} + \sum_{i=1}^N \sum_{j=i+1}^N \frac{1}{r_{ij}} + \sum_{A=1}^{N_{atom}} \sum_{B=A+1}^{N_{atom}} \frac{Z_A Z_B}{R_{AB}} \quad (2.5)$$

Based on the variational principle, Equation 2.6 illustrates the quantity that one should minimize to obtain the best estimate for the real electronic wavefunction and, therefore, energy. If it was not for the electronic repulsion term in Equation 2.5, the electronic Schrödinger equation would be separable in each of the electronic coordinates and an antisymmetrized combination of products of hydrogenoid one-electron wavefunctions (*i.e.*, molecular orbitals) would represent the exact electronic wavefunction for our problem. Such wavefunction could be written as a Slater determinant (Equation 2.7). Despite the non-separability behavior of the electronic Schrödinger equation, the Slater determinant will be our starting point for the HF method. The main idea is to find the best set of molecular spin-orbitals that minimizes the energy of the system according to Equation 2.6, where ε_0 is the exact energy of the system in the Born-Oppenheimer framework.

$$E_0 = \langle \psi(r_1, r_2, \dots, r_N; \mathbf{R}) | \hat{H}_{elec} | \psi(r_1, r_2, \dots, r_N; \mathbf{R}) \rangle \geq \varepsilon_0 \quad (2.6)$$

$$\psi(r_1, r_2, \dots, r_N; \mathbf{R}) = \frac{1}{\sqrt{N!}} \begin{vmatrix} \phi_1(r_1) & \phi_2(r_1) & \dots & \phi_N(r_1) \\ \phi_1(r_2) & \phi_2(r_2) & \dots & \phi_N(r_2) \\ \vdots & \vdots & \ddots & \vdots \\ \phi_1(r_N) & \phi_2(r_N) & \dots & \phi_N(r_N) \end{vmatrix} = |\phi_1, \phi_2, \dots, \phi_N\rangle \quad (2.7)$$

Substitution of Equation 2.7 into Equation 2.6 and evaluating the one and two-electron expectation values using the so called Slater-Condon Rules (SZABO; OSTLUND, 1996), one is able to derive Equation 2.8 that defines the Hartree-Fock energy as a functional of a set of molecular spin-orbitals $\{\phi_i(r)\}$. The first term in Equation 2.8 represents the one-electron integrals ($\hat{h} = -\frac{1}{2}\nabla^2 - \sum_A \frac{1}{r_{iA}}$ is the one-electron Hamiltonian) computed over all the occupied molecular orbitals. The second term represents the two-electron integrals, and it can be decomposed into a Coulombic term that arises from the interaction between the charge densities of two molecular orbitals and an Exchange term that arises from the antisymmetric nature intrinsic to the quantum description of fermions. A constrained minimization of Equation 2.8 leads to the canonical Hartree-Fock equation (Equations 2.9 and 2.10), that results in the best set of molecular orbitals within the framework of a mean-field approximation.

$$E_0 = \sum_i^{occ} \langle i | \hat{h} | i \rangle + \sum_i^{occ} \sum_{j < i}^{occ} \langle ij | ij \rangle - \langle ij | ji \rangle \quad (2.8)$$

$$\hat{f}\phi_i(r) = \epsilon_i\phi_i(r) \quad (2.9)$$

$$\hat{f}(r) = \hat{h}(r) + v^{HF}(r) \quad (2.10)$$

The Hartree-Fock potential (v^{HF} in Equation 2.10) is given by a combination of Coulomb and Exchange operators (Equations 2.11 and 2.12, respectively) based on the set of occupied molecular orbitals, as shown in Equation 2.13. It can be noted from Equation 2.9 represents the interaction of each electron in with an average potential caused by the other electrons of the systems. Due to such characteristic of the Hartree-Fock equations, such approximation is also known as the mean-field approximation.

$$J_j(r_1)\phi_i(r_1) = \int dr_2 \phi_j^*(r_2) \frac{1}{r_{12}} \phi_j(r_2) \phi_i(r_1) \quad (2.11)$$

$$K_j(r_1)\phi_i(r_1) = \int dr_2 \phi_j^*(r_2) \frac{1}{r_{12}} \phi_i(r_2) \phi_j(r_1) \quad (2.12)$$

$$v^{HF}(r) = \sum_j J_j(r) - K_j(r) \quad (2.13)$$

Despite the availability of several numerical methods to solve Equation 2.9, we shall only consider, in the present work, the formalism introduced by Roothaan and Hall. The assumption that one could expand the molecular orbitals as a combination of known atom-centered functions (Equation 2.14) hugely simplifies the procedure towards the solution of the Hartree-Fock equations. Ideally, such expansion would require an infinite and complete set of functions. However, in order to make the problem computationally attainable, one usually chooses a set that contains an appropriate number of functions that behave in an expected fashion, such as a slowly decaying exponential behavior (which represents a diffuse function), higher angular momentum functions (indicating polarizability) or the ability to include correlation to the innermost (core) electrons.

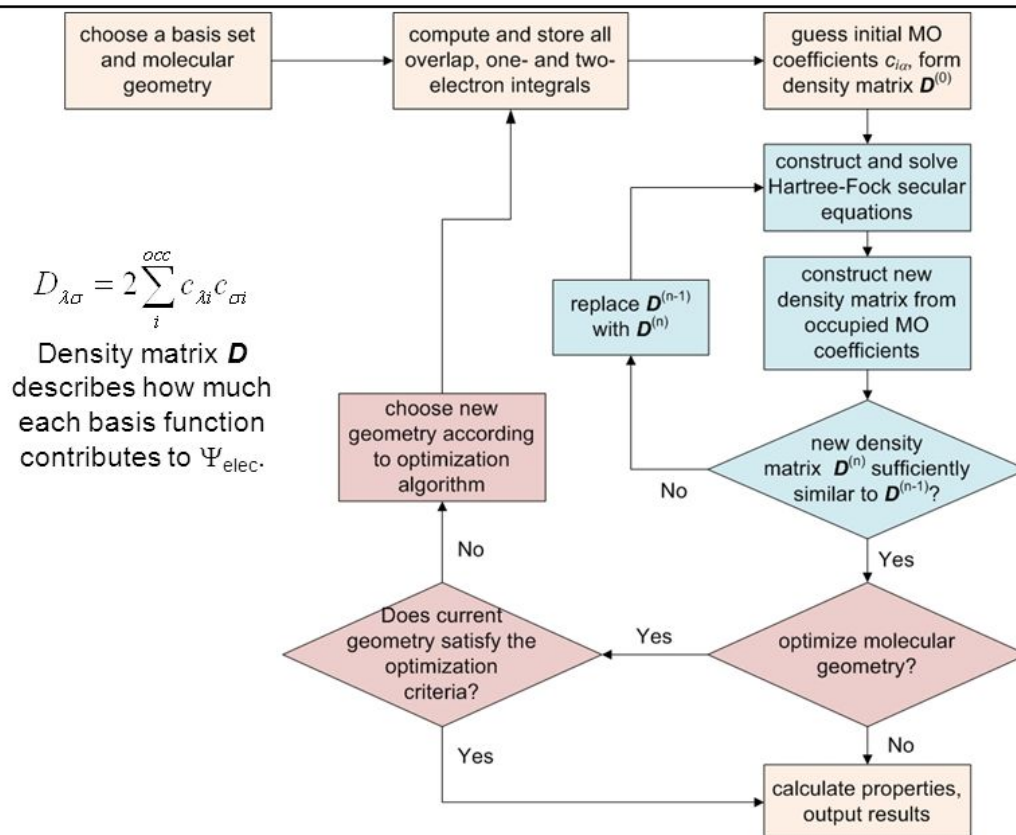
$$\phi_i = \sum_{\mu=1}^K C_{\mu i} \chi_{\mu} \quad (2.14)$$

The Roothaan-Hall procedure allows us to write the integro-differential Hartree-Fock equations as a pseudo-eigenvalue problem (Equation 2.15, where \mathbf{F} represents the Fock operator projected into the basis set, \mathbf{S} is the overlap matrix of the elements of the basis set, \mathbf{C} is the expansion coefficients matrix and ϵ is a diagonal matrix containing the energies of the molecular orbital), whose solution is achieved in an iterative manner: the Self Consistent Procedure, or simply SCF equations, which is illustrated in Figure 2.2. Although the SCF procedure will result in the same number of molecular orbitals as elements in the basis set, only the occupied ones will be used to update the new Fock matrix at each iteration cycle. Such update is done by computing the density matrix of the system, which is defined as $D = C_{occ}^T C_{occ}$. The density matrix also gives us information about the electron density of the system and, by analyzing such quantity, one can obtain valuable information about the charge distribution of the system.

$$\mathbf{FC} = \epsilon \mathbf{SC} \quad (2.15)$$

Even though it provides a useful chemical insights about the nature of a system, the description provided by Hartree-Fock methodology is incomplete due to the mean-field approximation. The difference between the exact energy of the system and the best estimated achieved at the HF level is called the correlation energy ($E_{corr} = E_{exact} - E_{HF}$) and usually represent less than 1% of the total energy of system, which is roughly of the same order of the magnitude of the energy involved in breaking and forming chemical bonds. In order to get a better estimate for the energy of the system and its wavefunction,

The SCF Procedure and Geometry Optimization



Adapted from Cramer, C. J., *Essentials of Computational Chemistry, Theories and Models*. Second ed.; Wiley: 2004.

FIGURE 2.2 – Generalized Self Consistent Procedure (SCF) applied to the Hartree-Fock methodology. Reproduced from (CRAMER, 2004).

we should consider not only the occupied molecular orbitals, but somehow also use the virtual orbitals that we get free of charge from the SCF procedure. Post Hartree-Fock correlated methods are based on such idea. The first approach would be to consider the difference between the exact electronic Hamiltonian and the approximate correspondent operator that arises from HF theory as a small perturbation and use Møller-Plesset Perturbation Theory to get energy corrections. It is common to truncate the perturbation expansion series at the second order (MP2) that accounts for double excitations from occupied to virtual orbitals from the Hartree-Fock reference wavefunction. Finally, it is also possible to expand the exact wavefunction of the system as a combination of several Slater determinants based of the HF reference. Such approach leads to the family of Configuration-Interaction and Coupled-Cluster theory based methods. Despite their huge importance to quantum chemistry nowadays and their formidable mathematical and physical underlying foundation, these methodologies are out of the scope of the present work and a detailed derivation could be find in the literature (SZABO; OSTLUND, 1996; HELGAKER *et al.*, 2004).

2.1.3 The many electron problem - Density Approach

An alternative approach would be to describe the system and all its properties by the electronic density, instead of the wavefunction. It is important to notice that the wavefunction represents an abstract mathematical concept that depends on multiple coordinate variables and, itself, is not physically meaningful. On the other hand, the electron density depends only on the position vector and could be used to explain several phenomena, such as charge-transfer process. The theoretical background that allows us to use the electron density to describe all the properties of a system was originally proposed by Hohenberg and Kohn (HOHENBERG; KOHN, 1964) and is summarized in the form of two theorems, which are stated below.

Theorem 1 *The external potential $v_{ext}(r)$, and hence the total energy, is a unique functional of the system's electron density $\rho(r)$.*

Theorem 2 *The groundstate energy can be obtained variationally: the density that minimizes the energy is the exact groundstate density.*

In the density functional approach the strategy is to minimize the energy functional, which can be decomposed into a kinetic term (T), a coulombic interaction term (U) and an exchange-correlation term (V), with respect to the electronic density of the system (Equation 2.16). Once again, due to the interaction between the electrons, the form of the third term in Equation 2.16 is unknown, and one would have to find an approximate way to write the energy components as a true functional of the system's density. The practicality of DFT was developed by Kohn-Sham and is known as the KS-DFT approximation (KOHNSH; SHAM, 1965). The Kohn-Sham equations are derived by assuming that the true density of the system is equal to the density of a system of non-interacting electrons. In this non-interacting model, the wavefunction of the system is also represented by a Slater determinant and the Kohn-Sham equations are similar, in form, to those presented in the previous section. In fact, both HF and DFT could be considered mean-field theories: the first aims to find the best set of molecular orbitals, whereas the later aims to find the best electronic density to describe the real system. The main difference lies on the effective potential, or Kohn-Sham in the context of DFT, term. As pointed out previously, one of the limitations of density functional theory is that, despite being able to write the ground state electronic energy as a functional of the density, such expression is still unknown. Therefore, a plethora of these exchange-correlation functionals have been devised to approximately solve the Kohn-Sham equations.

$$E[n] = \langle \Psi[n] | \hat{T} + \hat{U} + \hat{V} | \Psi[n] \rangle = T[n] + U[n] + V[n] \quad (2.16)$$

The first and most natural approach would be to use the homogeneous electron gas (HEG) model expression derived by Thomas-Fermi-Dirac for the Exchange component of the energy. Such approach led to the development of the Local Density Approximation (LDA) to the exchange-correlation functional, which depends solely on the electron density at each point in space. LDA has found a highly applicability in the field of solid-state physics, given the highly delocalized feature of metallic systems. The chemical community, on the other hand, has not been fond of this class of functionals due to their compromises accuracy to describe some of the properties of chemical interest. An increased accuracy could be observed for DFT simulations when the exchange-correlation functionals were dependent not only on the local density, but also its higher derivatives (gradient, laplacian, etc). Such use of higher derivatives of the density in the construction of the DFT functionals led to the GGA (gradient generalized approximation) and meta-GGA class of exchange-correlation functionals. Still, DFT has an intrinsic issue. The self-interaction problem arises from the fact that the exchange potential, due to its approximate form, does not cancel out the coulomb potential, leading to a unbalanced description of the electronic energy. The class of hybrid-functionals is based on including a fraction of exact (HF) exchange energy to the local exchange-correlation term of the density functional. Finally, so far we have only mentioned classes of functionals that only considered the occupied KS orbitals. Other approaches, such as random-phase approximation (RPA) and double hybrid functionals use the virtual orbitals to correct the ground state electronic energy. Figure 2.3 briefly summarizes the hierarchy towards chemical accuracy of the approximations for the exchange-correlation term in the KS-DFT equations that were mentioned in this section (PERDEW *et al.*, 2005).

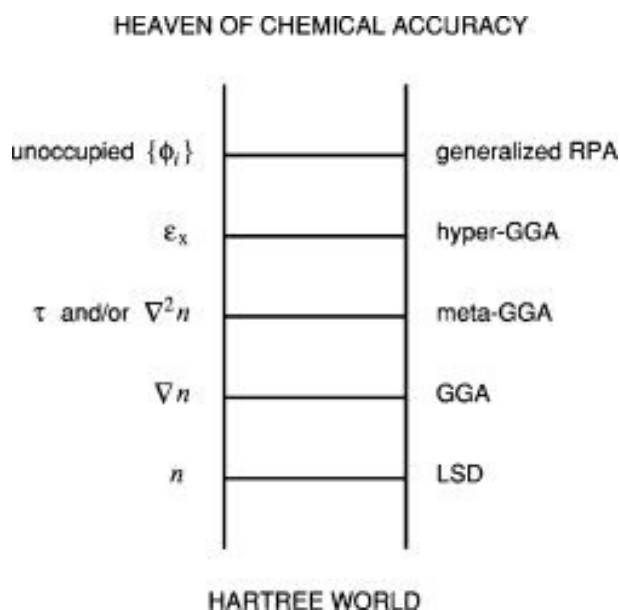


FIGURE 2.3 – Jacob’s ladder of density functional approximations to the exchange-correlation energy. Reproduced from (PERDEW *et al.*, 2005).

2.1.4 Supermolecular approach

Both Hartree-Fock (HF) based and density functional methods can be used to compute interaction energies between two complexes by the so called supermolecular approach (Equation 2.17, in which $E_{A...B}$ represents the total energy of the dimer, and E_A and E_B corresponds to the energies of each isolated monomer). The importance of such approach relies on a way to quantitatively understand the interaction between two monomers. However, the supermolecular approach does not allow us to comprehend the nature of the interaction between the two systems. It only computes the value of the total interaction energy, which contains contributions of a complex set of intermolecular interactions. Finding the weight in which each component of these interactions contributes to the total energy may reveal quite important features of the molecular system. Moreover, an intrinsic problem of the supermolecular approach relies on the fact that, if the set of atomic-centered functions (basis set) used to represent the molecular orbitals of each individual monomer is not suitable and provides an unbalanced description of the monomers (Figure 2.4), basis set superposition error (BSSE) might play an important role and the interaction energy and other properties will be incorrectly described (DUIJNEVELDT *et al.*, 1994).

$$E_{int} = E_{A...B} - E_A - E_B \quad (2.17)$$

2.1.5 Intermolecular Forces

Non-covalent interactions play a central role in many applications of biological and materials chemistry. A complete physical understanding of the interactions between non-bonded chemical groups is necessary to achieve the goals of optimizing drug binding or controlling the structure of organic crystals and nano self-assemblies. The combined progress of computational hardware and software development in recent years have allowed ab initio quantum chemistry methods to be applied to a wide variety of complex systems, including many that can provide insight into the nature of non-covalent interactions. Classical polarization theory claims that there are three groups of intermolecular forces:

- **Electrostatic (Elst.):** is the energy component that arises from the mutual interaction between the electron densities of two molecular species (monomers) in its ground-state. It includes Coulombic multipole-multipole-type interactions as well as the interpenetration of charge clouds.
- **Induction (Ind.):** the electron density of one of the monomers creates an electric field that can excite the density of the other monomer. The interaction between an excited monomer with the other unexcited monomer is known as induction.

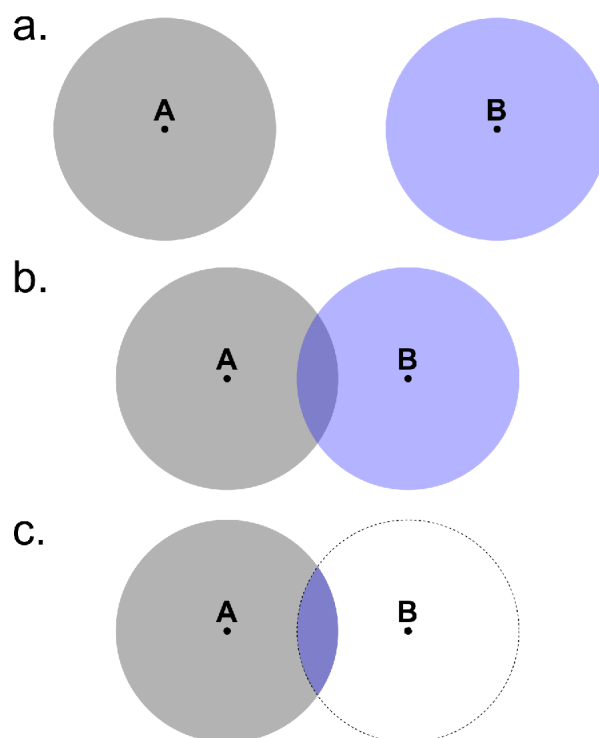


FIGURE 2.4 – Basis set superposition error. (a) At large distances, the monomers A and B are isolated and their basis functions hardly overlap. (b) As the monomers get closer to each other, overlap increases and some of the functions centering on B start to be also available to describe A. (c) With a more complete set of functions, A is better described at closer distances and the interaction energy of the system is over-stabilized due to this artificial effect.

This type of interaction could be divided into two parts: the first corresponds to the ability of one monomer to be polarized by the other one, and the second corresponds to charge-transfer between the two monomers, that arises from the excitation of the electrons from an occupied orbitals of one the monomer to the virtual orbitals of the other.

- Dispersion (Disp.): the interaction between the monomers that have been excited due to the electric field created by the other monomer's perturbed charge distribution. It can also be represented by the attractive force resulting from the dynamical correlation between electrons on different sub-systems.

Due to fermionic antisymmetry requirements for the wavefunction of the whole system, there is also the Exchange-repulsion (Exch.) energy component. It arises from the overlap of the wavefunction of each sub-system and also represents the steric hindrance when the wavefunctions or charge densities of the two monomers start to overlap.

2.1.6 Symmetry-Adapted Perturbation Theory - SAPT

As mentioned previously, one of the approaches used to compute interaction energies between non-bonded systems is the supermolecular approach. Perturbation theory can also be used to compute the interaction energy as a perturbation to the Hamiltonian of the individual monomers as shown by Equation 2.18, where \hat{F} and \hat{W} represent the Fock and the intramolecular correlation operator, respectively, for each monomer, whereas the intermolecular interaction is modeled by the \hat{V}_{AB} operator. The most widespread of such approaches is Symmetry-Adapted Perturbation Theory (SAPT). A key advantage over supermolecular approaches is that in addition to the interaction energy, SAPT provides a decomposition of the interaction into physical components of electrostatics, exchange, induction, and dispersion (JEZIORSKI *et al.*, 1994).

$$\hat{H} = \hat{F}_A + \hat{F}_B + \hat{W}_A + \hat{W}_B + \hat{V}_{AB} \quad (2.18)$$

Since the total interaction energy will be expanded as a double perturbation theory on the intramolecular correlation and intermolecular interaction, one could choose to truncate the series at different orders, leading to different levels of SAPT. Figure 2.5 illustrates the truncation scheme for several levels of symmetry-adapted theory. In this work, to obtain a reasonable trade-off between accuracy and computational cost, we will only employ the zeroth-order SAPT, which expands the intermolecular potential through second-order perturbation theory, but does not account for intramolecular correlation. The efficiency of SAPT0 for closed-shell systems has already been reported on the literature and, when this method is associated with the jun-cc-pVDZ basis set, performs relatively well due to error compensation for a wide range of systems (PARKER *et al.*, 2014).

2.1.7 Visualizing Non-Covalent Interactions (NCI)

So far, we have only discussed methods that would be able to assess the interaction energy between two systems. The Symmetry-Adapted Perturbation Theory also gives us valuable information about the physical nature of such property by decomposing it into meaningful components such as electrostatics, exchange, induction and dispersion. However, the question remains: does knowing the total interaction energy, or its components, provide sufficient “insight”? Chemists tend to rely upon intuitive concepts, such as repulsion of electron pairs and polarization, and a mathematical description might not be able to describe the nature of a given phenomenon. In this sense, questions such as “Which region of the system is affected by this interaction” still remains to be properly addressed.

Given that NCI arise from electrical forces acting on charge distributions, it is logical to analyze the behavior of the electron density, which is naturally assessed through quan-

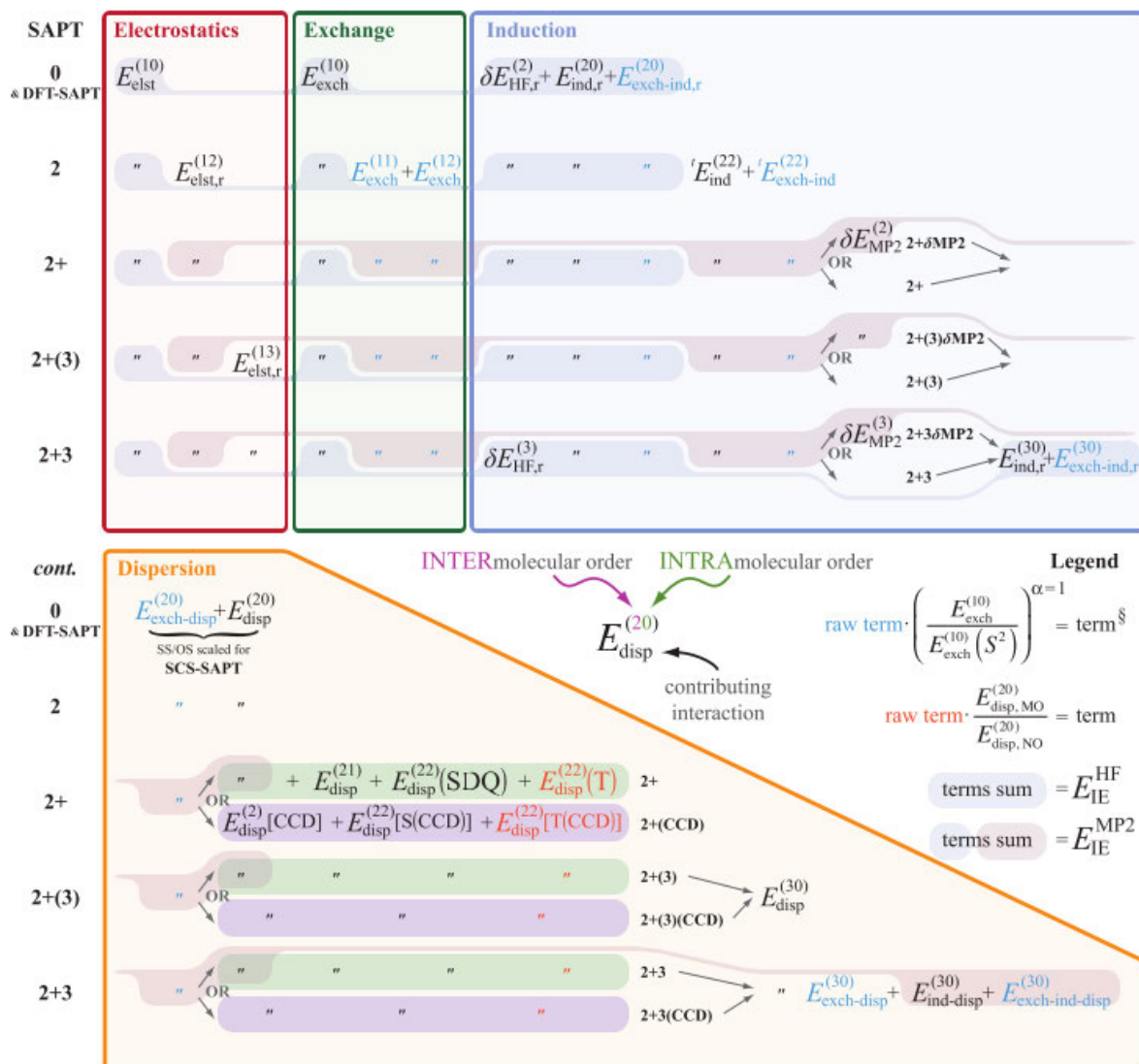


FIGURE 2.5 – Composition of several levels of SAPT, explicitly showing the truncation order of the perturbation series for both intramolecular correlation and the intermolecular potential. In this work, we will attain to the SAPT0 level. Reproduced from (PARKER *et al.*, 2014).

tum mechanics by solving the electronic Schrödinger equation. In this sense, several scalar field descriptors have already been proposed to understand the behavior of the electronic density. The electron localization function (ELF) (SAVIN *et al.*, 1997), for instance, is associated with same-spin pair densities of electrons and is useful to assess both bonding and atomic shell structures. Unfortunately, ELF, while being extremely valuable to characterize covalent bonding, does not allow the full recognition on non-covalent interactions, especially weak ones such as van der Waals dispersion. Another example would be the analysis of the density topology, which is the central idea behind Bader’s Quantum Theory of Atoms in Molecules (QTAIM) (BADER, 1991), which exploits the topology of the density, *i.e.* its gradient and hessian fields, to redefine atoms and bonds in molecules

in a rigorous framework.

Another tool also capable of detecting and visualizing weak interactions is the Non-Covalent Index (NCI) (JOHNSON *et al.*, 2010), which is partially inspired by QTAIM. In this case, the main quantity analyzed is the reduced density gradient (s), which is defined by Equation 2.19 and describes the deviation from a homogeneous electron distribution. As described in Table 2.2, in density tails (*i.e.* regions far from the molecule, in which the density is decaying to zero exponentially), the reduced gradient will have very large positive values. Conversely, a vanishing reduced gradient is observed for regions of both covalent bonding and non-covalent interactions.

$$s = \frac{1}{2(3\pi^2)^{\frac{1}{3}}} \frac{|\nabla\rho|}{\rho^{\frac{4}{3}}} \quad (2.19)$$

TABLE 2.2 – Regions and respective behaviors used in the Non-Covalent Index Analysis. The cells describe the range of values that each property (density, gradient and reduced gradient) could assume in a specific region.

| | Around Nuclei | Chemical Bond | Weak Interaction | Boundary |
|--|----------------------|----------------------|-------------------------|-----------------|
| $ \nabla\rho(r) $ | Large | 0 ~ Minor | 0 ~ Small | Small |
| $\rho(r)$ | Large | Medium | Small | 0 |
| RDG ($\mathbf{s}(\mathbf{r})$) | Medium | 0 ~ Minor | 0 ~ Medium | Very Large |

Hence, a plot of s versus ρ can provide a valuable information about the topology of the electron density and the dominating interactions through different regions of the system. For isolated systems, the following behavior is expected (Figure 2.6): the top left corner of Figure 2.6 represents the molecular boundaries, whereas the bottom right corner indicates covalent bond regions. It is worth noticing that there are no spikes in the low-density region. These peaks will appear when the system considered presents intra and/or intermolecular weak interactions, such as in the case of water, methane, benzene and formic acid dimers (Figure 2.7).

To this point, we have found that noncovalent interactions can be isolated as regions with low density and low reduced gradient. The density values of the low-gradient spikes also appear to be an indicator of the interaction strength. However, very different types of interactions (*i.e.*, hydrogen-bonding and steric crowding) appear in the same region of density/reduced- gradient space. To distinguish between these interactions, we consider second derivatives of the density. On the basis of the divergence theorem, the sign of the Laplacian ($\nabla^2\rho$) of the density indicates whether the net gradient flux of density is entering ($\nabla^2\rho < 0$) or leaving ($\nabla^2\rho > 0$) an infinitesimal volume around a reference point. Hence, the sign of $\nabla^2\rho$ determines whether the density is concentrated or depleted at that point, relative to the surroundings. To distinguish between different types of weak interactions, one cannot use the sign of the Laplacian itself, because the sign is dominated by negative

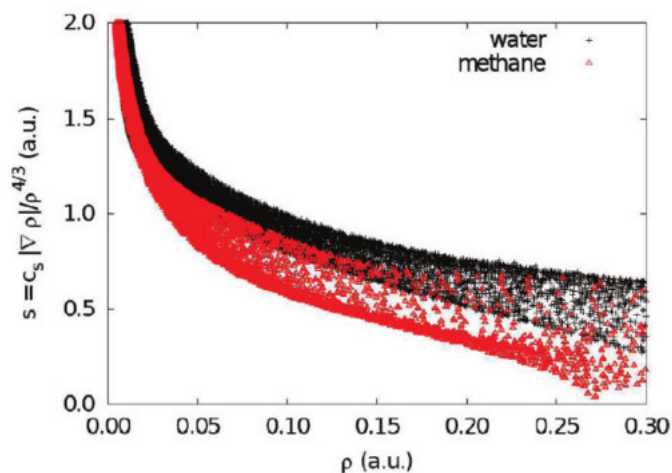


FIGURE 2.6 – Non-Covalent Index plot of RDG versus density for isolated systems. Reproduced from (JOHNSON *et al.*, 2010).

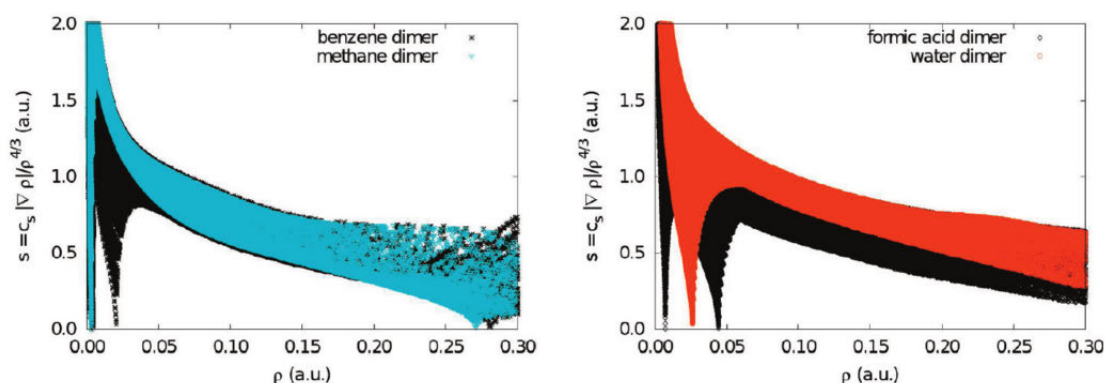


FIGURE 2.7 – Non-Covalent Index plot of RDG versus density for interacting systems. Reproduced from (JOHNSON *et al.*, 2010).

contributions from the nuclei. Instead, contributions to the Laplacian along the axes of its maximal variation must be analyzed. These contributions are the eigenvalues λ_i of the electron-density Hessian (second derivative) matrix, such that $\nabla^2\rho = \sum_i \lambda_i$, ($\lambda_1 < \lambda_2 < \lambda_3$). At the nuclei, all of the eigenvalues are negative, while away from them, $\lambda_3 > 0$. In molecules, the λ_3 values vary along the internuclear direction, while λ_1 and λ_2 report the variation of density in the plane normal to the λ_3 eigenvector. Interestingly, the second eigenvalue (λ_2) can be either positive or negative, depending on the interaction type. On the one hand, bonding interactions, such as hydrogen bonds, are characterized by an accumulation of density perpendicular to the bond, and $\lambda_2 < 0$. Non-bonded interactions, such as steric repulsion, produce density depletion, such that $\lambda_2 > 0$. Finally, vdW interactions are characterized by a negligible density overlap that gives $\lambda_2 \leq 0$. Thus, analysis of the sign of λ_2 enables us to distinguish different types of weak interactions, while the density itself enables us to assess the interaction strength. Figure 2.8 summarizes this behavior of both density, reduced-density gradient and sign of the the Hessian eigenvalues that will be used in the analysis of the Non-Covalent Index (NCI).

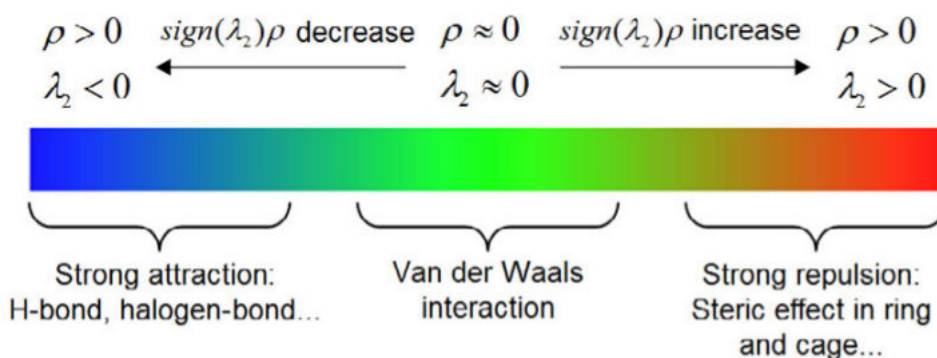


FIGURE 2.8 – Summary of the interpretation of the Non-Covalent Index analysis. Reproduced from (LU; CHEN, 2012).

2.2 Computational Details

In the present study, we employed SAPT0(HF) and several approximations for the exchange-correlation term in DFT, such as B3LYP (BECKE, 1988; LEE *et al.*, 1988), B2PLYP (GRIMME, 2006), ω B97X-D (CHAI; HEAD-GORDON, 2008), ω PBE (PERDEW *et al.*, 1996a), PBE0 (PERDEW *et al.*, 1996b) to analyze the interaction of two different carbon-based pore structures with several gas molecules/atoms (Ar, Ne, He, H₂, N₂, CO₂), associated with the jun-cc-pVDZ basis set for atomic orbitals (PAPAJAK; TRUHLAR, 2011). Moreover, in order to analyze the influence of dispersion effects on the total interaction energy between the two systems, we also applied Grimme’s D3 dispersion corrections (GRIMME, 2011; SMITH *et al.*, 2016) to some of the functionals previously listed. All the computations were performed using the Psi4 computational suite for quantum chemistry (PARRISH *et al.*, 2017). The Tkatchenko-Scheffler (vdW-TS) (TKATCHENKO; SCHEFFLER, 2009) and Many-Body Dispersion (MBD) (TKATCHENKO *et al.*, 2012) dispersion corrections were also used to evaluate the dispersion component of the total interaction energy. Computations using such methods were carried out with the FHI-AIMS computational package (BLUM *et al.*, 2009).

Figure 2.9 represent the methodology applied to obtain the potential energy surfaces described in the next chapter of the present work. In the case of diatomic molecules, the distance was taken from the pore center to the center of mass of the homonuclear diatomic molecule. Finally, for CO₂, the distance was taken from the carbon atom to the pore plane.

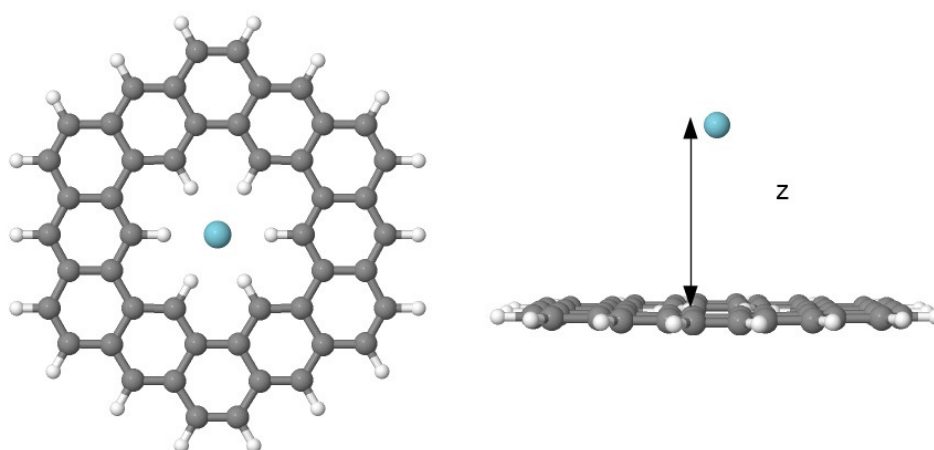


FIGURE 2.9 – Distances for the potential energy surfaces.

3 Unraveling the Importance of Pore Size

3.1 Motivation

It is important to emphasize that previous works, despite the mechanistic approach towards the computation of diffusion energy barriers and permeance rates, focused mainly on assessing the effect of pore size on such features. In the previously cited studies, a change on pore structure, such as topology and functionality, also meant modifying its physical pore diameter, giving rise to a plethora of systems with consistently different pore sizes. Consequently, it is not possible to account for the influence of each of these effects to the diffusion energy barrier in a separate and systematic fashion. Hence, a detailed understanding of all intermolecular interactions that take place in the sieving process is of paramount importance to design porous membranes with enhanced and tunable permeability and selectivity.

In the present study, our aim is to address the challenge posed by the design of efficient gas-separation membranes from a molecular perspective, shedding light into the puzzling question: how much does pore size contribute towards diffusion barriers? Moreover, another fundamental question concerns the ambiguous definition of pore itself in a quantum mechanical perspective. As pointed out previously, authors usually define pore size based on considerations about isosurfaces of the electron density, leaving it up to different interpretations of the which isovalue should be used in order to visualize the pore size. To tackle these questions, as model systems, we select two molecular graphene-like porous structures (Figure 3.1) having slightly different pore size and consistently distinct sp^2 carbon network to investigate whether they could exhibit different energy barriers towards the diffusion of hydrogen gas by means of a comprehensive analysis of the nature of the diffusion energy barrier.

3.2 C₂-square and C₂-pent Structure

A molecular model of a single pore was used to carry out all the quantum-theoretical treatments. Second-Order Møller-Plesset Perturbation Theory (MP2) (MØLLER; PLESSET, 1934) was used to carry out the relaxation step and assess the initial geometrical parameters of each pore. The def2-TZVP basis set (WEIGEND; AHLRICHS, 2005) was used in all atoms to perform this optimization process. The first structure investigated can be viewed as a topological derivation of Kekulene, in which some hexagonal rings are replaced by cyclobutadiene (square) moieties (Figure 3.1a). In this structure, each side of the whole hexagonal pore is constituted by biphenylene units (BRUNETTO *et al.*, 2012). The second structure selected for this study is a two-dimensional sp² carbon allotrope consisting of fused pentagon rings (MARUYAMA; OKADA, 2013). They will be denoted henceforth by C₂-square and C₂-pent, respectively. C₂-square presents a uniform C···C distance of 5.45 Å between the atoms along the pore diameter. On the other hand, C₂-pent display a slightly distorted circular geometry having approximately the same C···C distance as in C₂-square (5.47 Å) along the blue axis and 5.32 Å along the pore diameters in red (Figure 3.1b). Analyzing this feature alone, one would expect, for the C₂-pent pore, a higher energy barrier towards H₂ diffusion.

3.3 Diffusion Energy Barrier

Given the structural rigidity of the sp² carbon network, it is reasonable to assume that the energy barrier for the H₂ diffusion is not strongly affected by geometrical distortions. Therefore, the pore geometries were kept frozen in a follow-up scan to evaluate the interaction energy between H₂ and each porous membrane. Hence, the diffusion energy profile was computed by varying the perpendicular distance of the center of mass of H₂ to the plane of the porous structure (Figure 3.1c). Symmetry-Adapted Perturbation Theory (SAPT) (JEZIORSKI *et al.*, 1994) was the method of choice to compute the total interaction energy between the proposed porous structures and the hydrogen molecule at a range of distances between 0.0 Å and 5.0 Å. The perturbation series was truncated at the zeroth-order with respect to intramolecular correlation effects and at the second-order with respect to the intermolecular interaction, which corresponds to the SAPT0 approach. Following the suggestion from Parker *et al.*, the partially augmented jun-cc-pVDZ basis set (PAPAJAK; TRUHLAR, 2011) was used, since it provides the best trade-off between accuracy and computational cost (PARKER *et al.*, 2014). These calculations were performed using PSI4 computational suite (PARRISH *et al.*, 2017).

Figure 3.2 shows the potential energy surface representing the diffusion of H₂ through the two different pore types. At a first glance, these results reveal a counter-intuitive

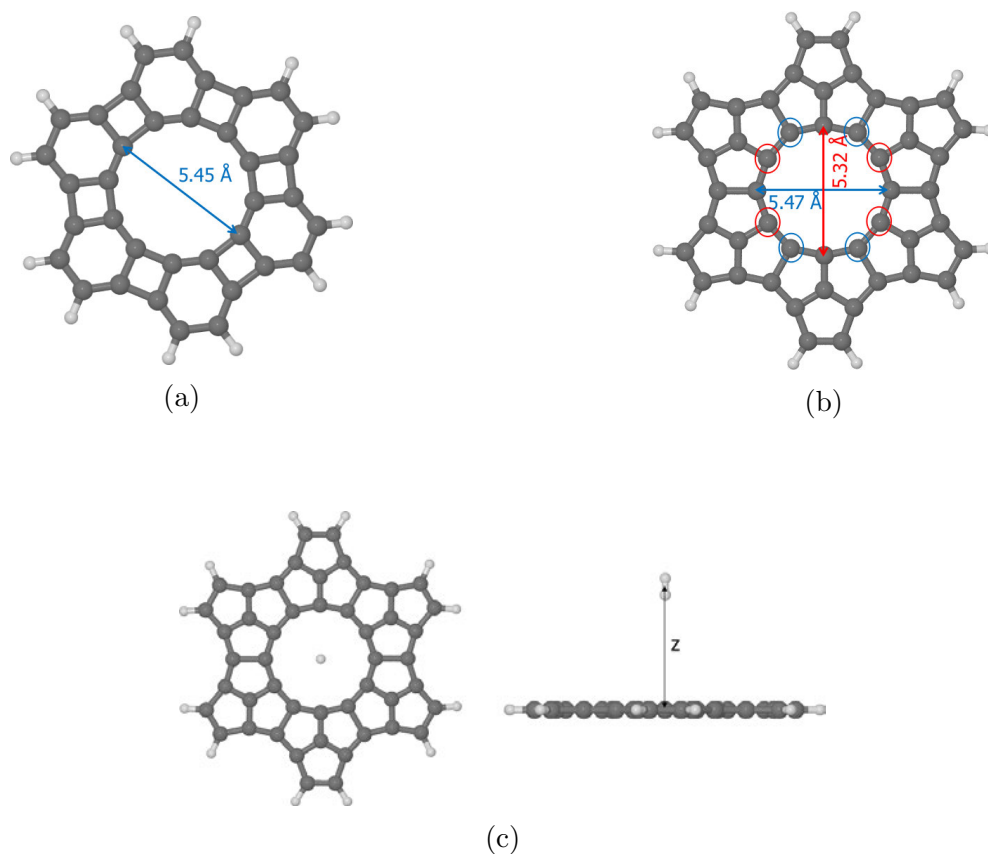


FIGURE 3.1 – Model systems for the analysis of the H₂ diffusion through porous graphene-based pores: (a) C₂-square structure, which presents a circular pore with a C···C diameter of 5.45 Å; (b) C₂-pent structure, which presents a slightly distorted circular pore whose C···C diameter is 5.47 Å for axis highlighted in blue and 5.32 Å for other in red; (c) One-dimensional path to compute the total interaction energy between the pore system and hydrogen gas.

behavior, since the slightly smaller pore C₂-pent has an energy barrier 1.2 kcal mol⁻¹ lower than the one obtained for the C₂-square. On the other hand, both structures present a well of roughly 1.0 kcal mol⁻¹ in depth for a z height (Figure 3.1c) between 2.0 Å and 3.0 Å.

3.4 Physical Decomposition of the Interaction Energy

The total energy of a gas molecule interacting with a pore system can be viewed as a result of a complex set of interactions derived from different physical mechanisms. In this sense, the SAPT method offers an important advantage compared to supermolecular approaches, since it allows to unfold the energy of the interacting systems into meaningful components, *i.e.*, contributions from electrostatics, induction, dispersion and exchange-

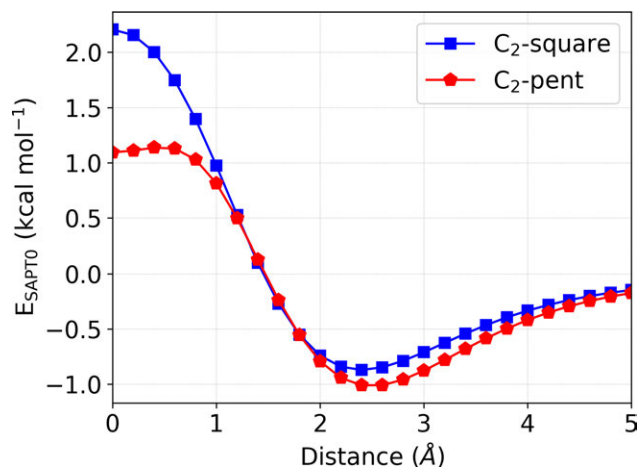


FIGURE 3.2 – Total interaction energy computed at the SAPT0/jDZ level of theory for the C₂-square···H₂ (blue) and C₂-pent···H₂ (red) systems.

repulsion are identified and quantified, as detailed previously in chapter 2. Figure 3.3 represents such decomposition scheme. Given the nature of the exchange-repulsion interaction, represented in Figure 3.3a, it could be understood as a possible measurement of the real size of the porous structure. In this sense, the fact that such component is about 0.9 kcal mol⁻¹ higher for the C₂-pent pore than for the C₂-square structure reflects the geometrical dissimilarities discussed above. This feature is consistent with the electron density profiles (Figures 3.4a and 3.4c) that seems more diffused into the pore center in the case of C₂-pent than in the C₂-square, thus granting a smaller effective pore size and a larger exchange-repulsion contribution towards the total interaction energy. Once more, it is important to emphasize the ambiguity in defining pore size by this strategy: different isovalues would lead to slightly different density profiles. The exchange-repulsion component could be used as a simple estimate for the diameter of the pore, in spite of not being enough to describe the diffusion process. Hence, the other three components should compensate the exchange contribution in order to account for the unexpected total interaction energy shown in Figure 3.2.

From the electrostatic component (Figure 3.3b), one can notice that such term alone almost completely balances the effect of the exchange-repulsion. Indeed, the electrostatic interaction between C₂-pent and H₂ is about 0.8 kcal mol⁻¹ lower than the one presented by the C₂-square. We turn to Figures 3.4a and 3.4c that represents the electrostatic potential for both membranes to rationalize such behavior. According to classical electrodynamics, the interaction between two charge distributions behaves inversely proportional with the distance between the electron densities. In this case, we notice that, given the smaller pore of C₂-pent, the electron clouds of H₂ and the pore would be closer to each other and their interaction would be stronger. Moreover, it is worth noticing that the inner edge of C₂-pent presents, on average, a higher potential than C₂-square, which also accounts for the observed behavior of the electrostatic component.

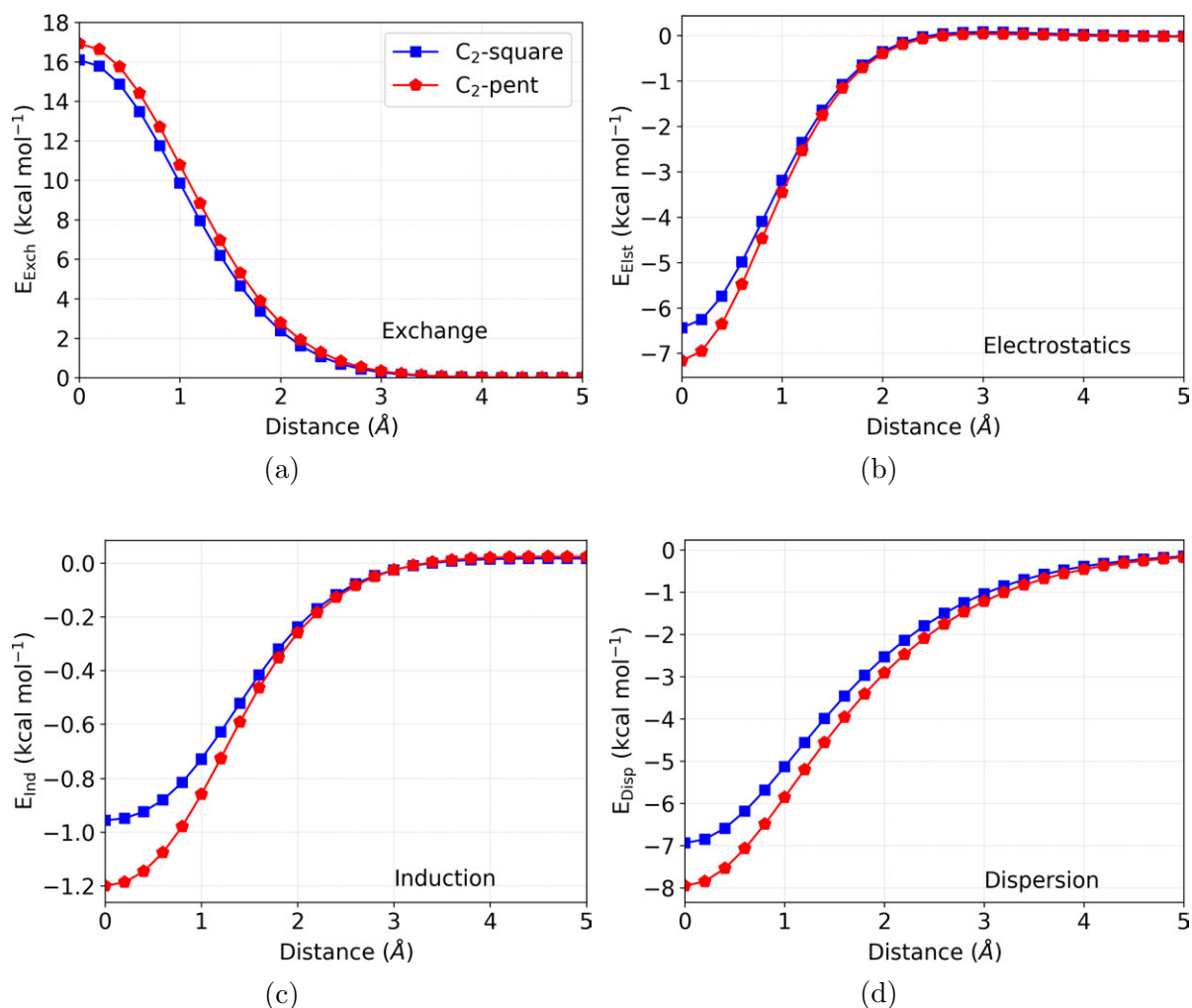


FIGURE 3.3 – Components of the total interaction energy for the systems C₂-square···H₂ (blue) and C₂-pent···H₂ (red): (a) Component of the interaction energy due to intermolecular exchange; (b) Component of the interaction energy due to electrostatics; (c) Component of the interaction energy due to induction; (d) Component of the interaction energy due to dispersion.

Figures 3.3c and 3.3d represent, respectively, the induction and dispersion components of the total interaction energy. These two components are stronger for the C₂-pent···H₂ complex than for the C₂-square counterpart: induction for C₂-pent is roughly 0.25 kcal mol⁻¹ lower than C₂-square, whereas the dispersion component grants an additional stability of about 1.0 kcal mol⁻¹ for the pore characterized by the fused pentagons. These results can be interpreted by analyzing the characteristics of the electronic structure for each pore. For instance, as a general rule, the lower the HOMO-LUMO energy gap (ΔE_{HL}) of a given π -conjugated structure, more delocalized its π electron cloud is expected to be; consequently, the stiffness of the π system should be higher, *i.e.*, its ability to polarize under the influence of an external electrical field, such as the one generated by the multipole charge distribution of H₂, is enhanced. ΔE_{HL} and isotropic polarizabilities were estimated using the range-separated hybrid functional with dispersion correction

ω B97X-D3 (LIN *et al.*, 2013) implemented in the ORCA computational package (NEESE, 2018). These computations predict a ΔE_{HL} value of 6.31 eV for the C₂-square structure and 4.70 eV for C₂-pent, suggesting a higher π -electron delocalization for the later. Complementary to this analysis, the π component of the electron localization function (ELF _{π}) (SAVIN *et al.*, 1997) (Figures 3.4b and 3.4d) reveals that the π -electrons of the C₂-square molecule are mostly localized on the six hexagonal rings separated by the anti-aromatic square moieties, while a large (π -electron) delocalization is found along the inner and external carbon circuits of the C₂-pent structure. Thus, it is expected a higher isotropic polarizability for the pentagonal pore when compared to the system containing square units. In fact, the isotropic polarizabilities for C₂-pent and C₂-square are 858 u.a. and 469 u.a., respectively. These features are reflected on the inductive and dispersive components of the total interaction energy: due to the higher degree of delocalization of the electron cloud and its higher polarizability, C₂-pent is more susceptible to the effects of the disturbed electron density of H₂, hence the marginally larger influence towards the total interaction energy when compared to the C₂-square pore.

3.5 NCI and Density Analysis of the Interaction

Additionally to the structural investigation presented in the previous section, a thorough analysis of the electronic fingerprints of the intermolecular interactions based on the topology and variations (ρ_D , $\rho_D = \rho_{AB} - (\rho_A + \rho_B)$) of the electron density was carried out. Our goal is to understand which part of both molecules contribute the most for the interaction between the two systems.

3.5.1 C₂-square

We start by analyzing the behavior of the NCI indicator and the density difference when the systems are far part from each other (Figure 3.5). At a separation distance of 5 Å, the interaction between the two systems could be considered negligible and polarization effects should be expected to play a minor role. Figure 3.5a illustrates the plot of the reduced density gradient (s) versus the signed density as described in the previous chapter. It is possible to notice that the peaks associated with weak attractive interactions (regions with blue and green colors) are vanishing. On the other hand and contrary to expected predictions, a repulsive red peak around 0.025 is present. An analysis of the reduced density gradient isosurface (Figure 3.5b) indicates that this peak originates from the interactions between the hexagons of the C₂-square structure. It is important to recall that, from the ELF analysis presented previously in this chapter, the square moieties of the pore structure play an important role in “isolating” these hexagon units. Although

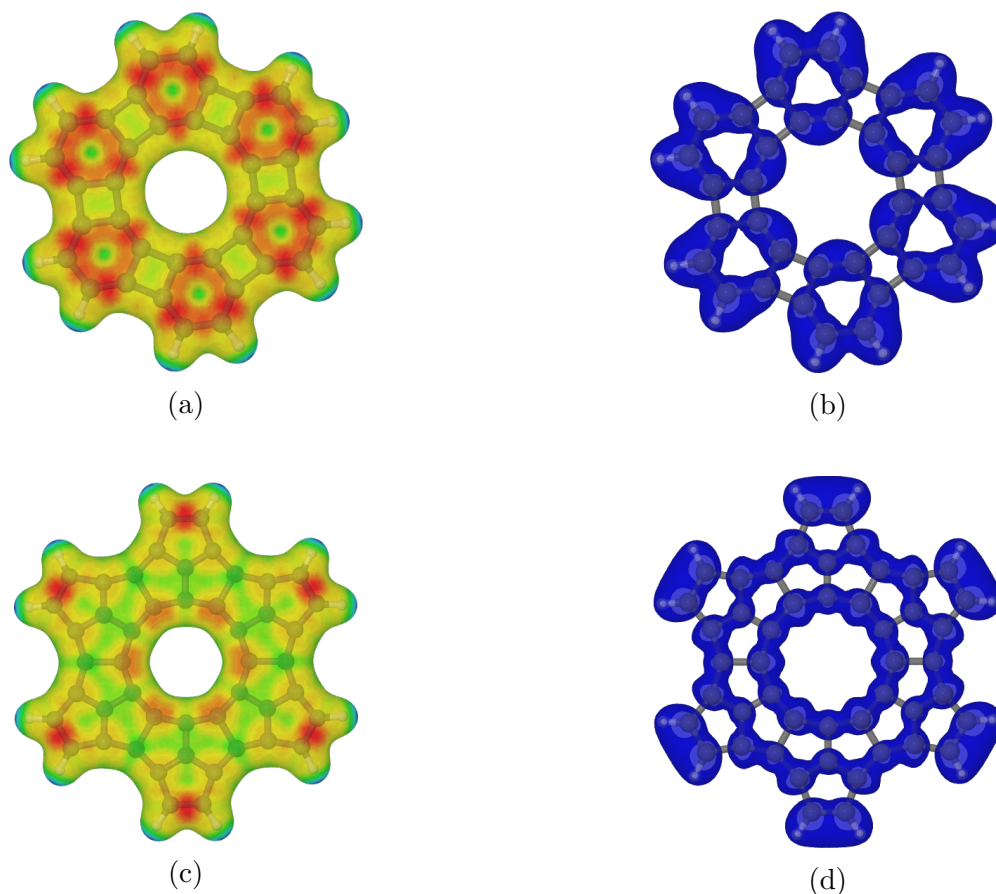


FIGURE 3.4 – Electrostatic potential map (ESP) and π component of the electron localization function (ELF_π) descriptions of both pore structures. The isovalues used to plot both isosurfaces were, respectively, 0.02 and $0.6 \text{ e}\text{\AA}^{-3}$. For the electrostatic potential maps, regions in blue and red indicate, respectively, areas that generate a lower and higher electric potential: (a) ESP for C_2 -square; (b) ELF_π for C_2 -square; (c) ESP for C_2 -pent; (d) ELF_π for C_2 -pent.

the SAPT0 method does not account for weak intramolecular interactions, such as the one just described, this behavior could also be viewed as an indicator of the importance of the exchange-repulsion towards the description of the physical pore size of each structure. Finally, Figure 3.5c shows the density difference between the complex and the isolated systems. In this case, we see that there is a density depletion in the H_2 region closest to the pore, which could be explained by the influence of histeric repulsion.

As the H_2 molecule approaches the pore structure, we see, from the total interaction energy (Figure 3.2) that an attractive interaction dominated by the dispersion component plays an increasing role. In this sense, Figure 3.6 represents the NCI and density behavior when the H_2 molecule and the C_2 -square pore are separated by a distance of 2.6 \AA , which corresponds to the minimum well on the potential energy surface. The plot of the reduced density gradient versus the signed density and its corresponding isosurface (Figures 3.6a and 3.6b) show that, once again, the majority of the repulsive interaction is originated

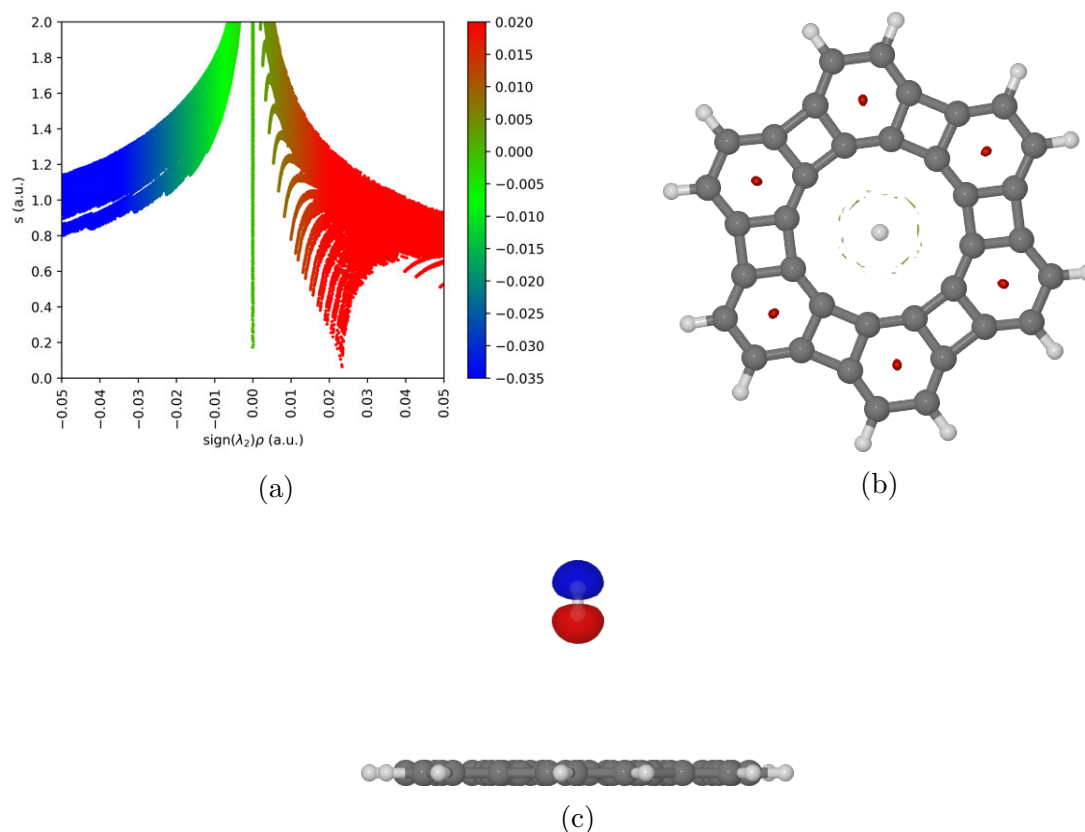


FIGURE 3.5 – Topological analysis for the interaction of C_2 -square with H_2 at a distance of 5 Å: (a) Plot of the reduced density gradient (s); (b) Reduced Density Gradient Isosurface (cutoff of $0.5 e \text{ Bohr}^{-3}$); (c) Isosurface (cutoff of $0.0005 e \text{ Bohr}^{-3}$) of the density difference between the complexes and the two isolated systems. Blue and red regions indicate density gain and loss, respectively, in comparison to the isolated system.

from the interaction between hexagon units, whereas the attractive part of the interaction is mostly dominated by the dispersion component that is distributed in a frustum's shape (cone truncated by a plane parallel to its base) around the region between the pore and the gas molecule. At this minimum well distance, it is also important to notice the behavior of the electron density difference (Figures 3.6c and 3.6d): instead of a depletion in the region closest to the pore due to steric effects, there is an increase in the electron density of the bottom atom of H_2 , which indicates a polarization of the molecule towards a bonding pattern with the pore.

Finally, we will also analyze the topological behavior of the electron density when the gas molecule is passing through the pore system (Figure 3.7). Once again, the repulsive peak around density values of 0.025 u.a. that corresponds to the intramolecular interactions of the pore remains and there is also an appearance of a second repulsive peak that is related to steric hindrance effects due to the passage of the H_2 molecule through the pore. Moreover, Figure 3.7b also shows the region affected by the interaction: the outermost parts of the plotted isosurface is colored in red, which indicates that this region

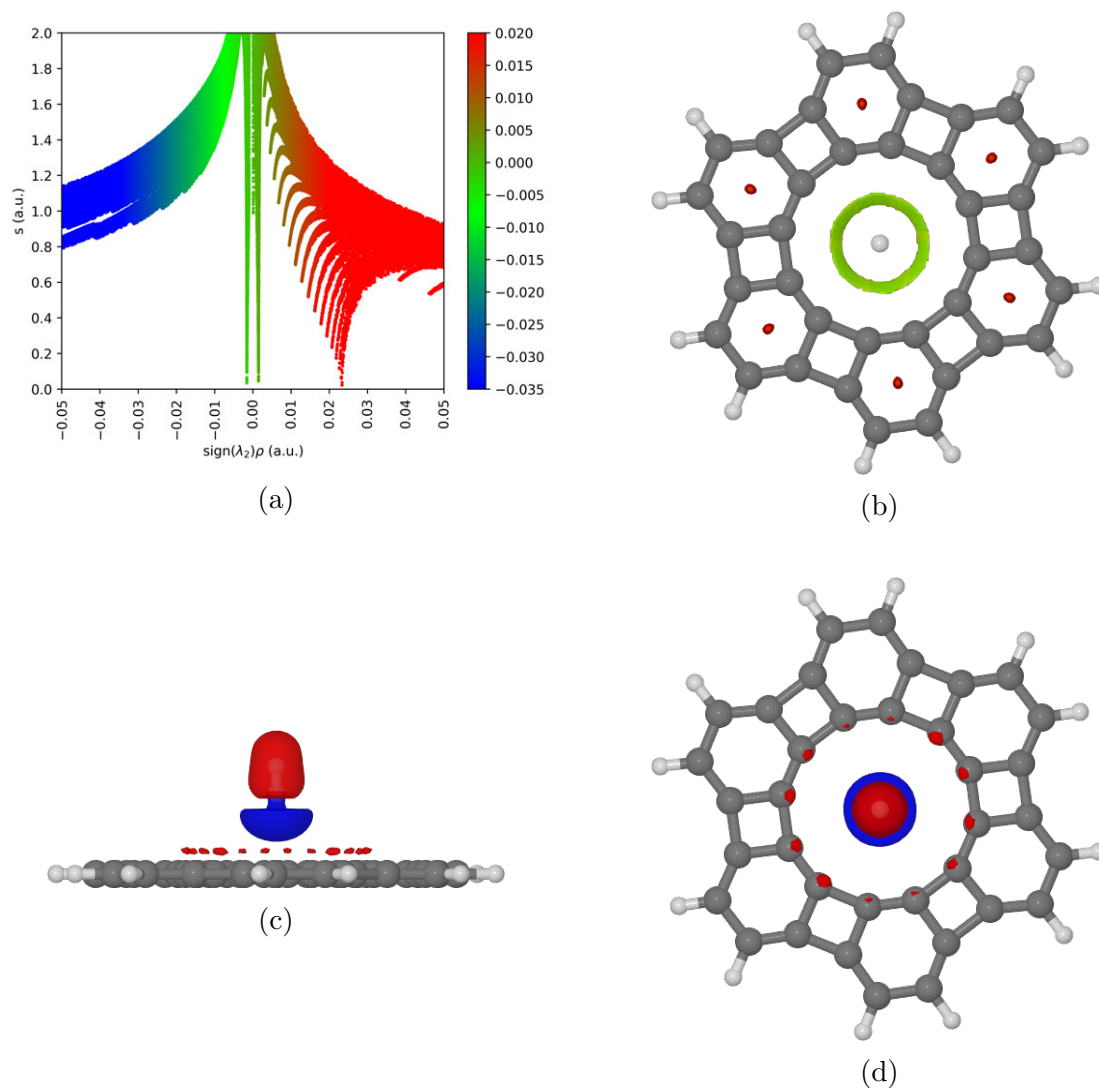


FIGURE 3.6 – Topological analysis for the interaction of C₂-square with H₂ at a distance of 2.6 : (a) Plot of the reduced density gradient (s); (b) Reduced Density Gradient Isosurface (cutoff of 0.5 e Bohr^{-3}); (c) Side view of the isosurface (cutoff of $0.0005 \text{ e Bohr}^{-3}$) of the density difference between the complexes and the two isolated systems; (d) Top view of the isosurface (cutoff of $0.0005 \text{ e Bohr}^{-3}$) of the density difference between the complexes and the two isolated systems. Blue and red regions indicate density gain and loss, respectively, in comparison to the isolated system.

is contributing towards the repulsive component, whereas the inner region is colored in a light green, corresponding to an interaction dominated by dispersion effects. This behavior is also reflected by the analysis of the density difference. Figures 3.7c and 3.7d illustrates the polarization of the external diameter of the pore and the gas molecules, and a depletion in the electron density between the two systems. This also validates the application of the SAPT methodology, once there seems to be no covalent bonding pattern.

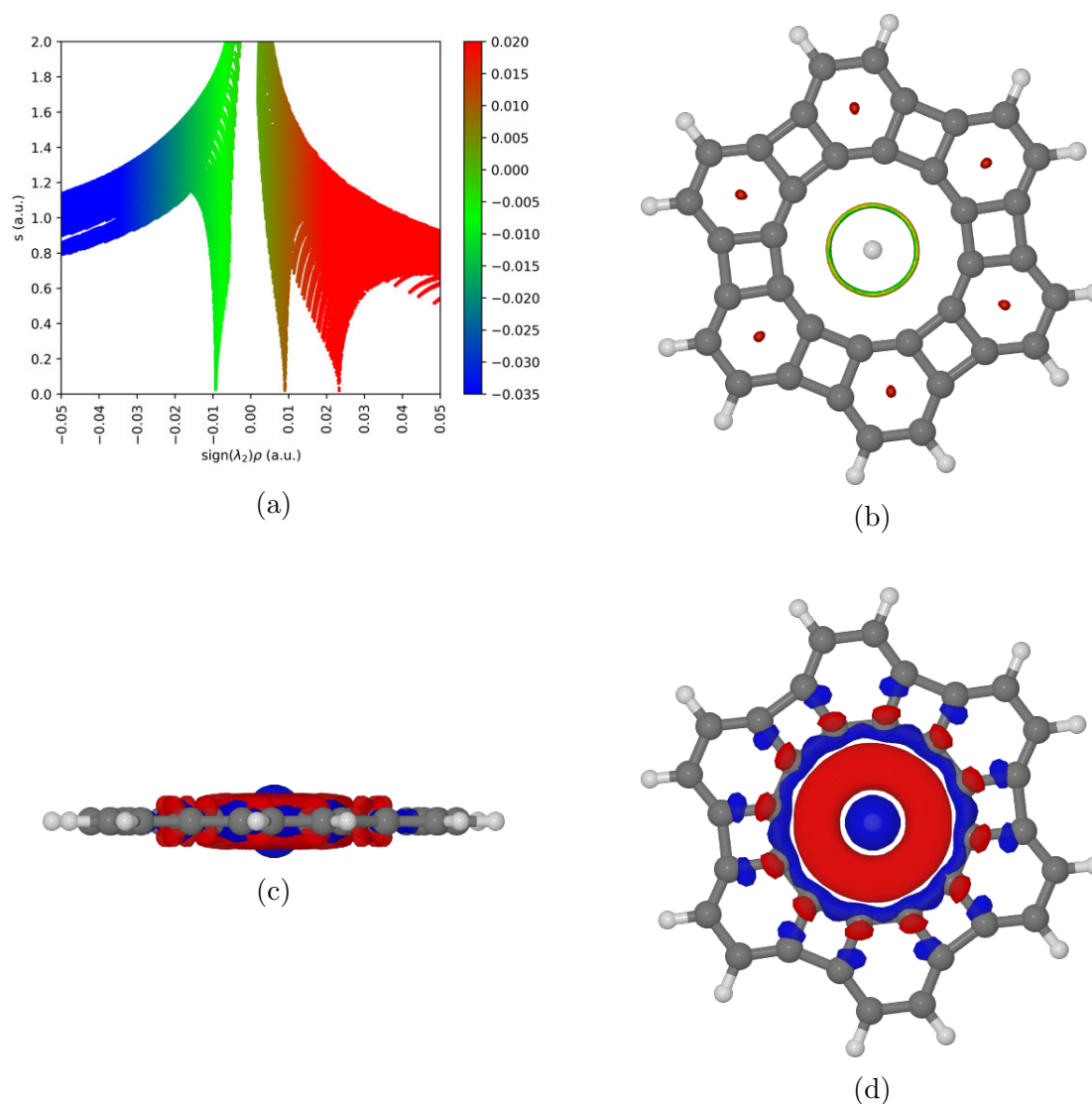


FIGURE 3.7 – Topological analysis for the interaction of C₂-square with H₂ at a distance of 0.0 Å: (a) Plot of the reduced density gradient (s); (b) Reduced Density Gradient Isosurface (cutoff of 0.5 e Bohr⁻³); (c) Side view of the isosurface (cutoff of 0.001 e Bohr⁻³) of the density difference between the complexes and the two isolated systems; (d) Top view of the isosurface (cutoff of 0.001 e Bohr⁻³) of the density difference between the complexes and the two isolated systems. Blue and red regions indicate density gain and loss, respectively, in comparison to the isolated system.

3.5.2 C₂-pent

The behavior described previously for the C₂-square pore structure is similar to the one observed here for C₂-pent. The NCI index indicate the existence of intramolecular interactions between the pentagon units of the pore structure that contributes to the repulsive effects. However, this behavior is now distributed over the whole molecule (Figure 3.8) and it could be viewed as a consequence of the higher electron delocalization, as shown by the ELF analysis. Furthermore, another difference arises in the case of C₂-pent when analyzing the electron density polarization when the two systems (H₂ and

pore) are brought together: it is possible to notice that, at the distance corresponding to the van der Waals minimum in the potential energy surface (2.6 Å), the whole H₂ molecule loses electron density (which is represented by the red color in the figure), which is accumulated in the region between the the pore and the gas, as indicated by the blue region (Figure 3.9a). Finally, at a distance of 0.0 Å, the polarization of the inner diameter of the C₂-pent structure is not homogenous: bonds between carbon atoms receive electron density that is removed from these atomic centers.

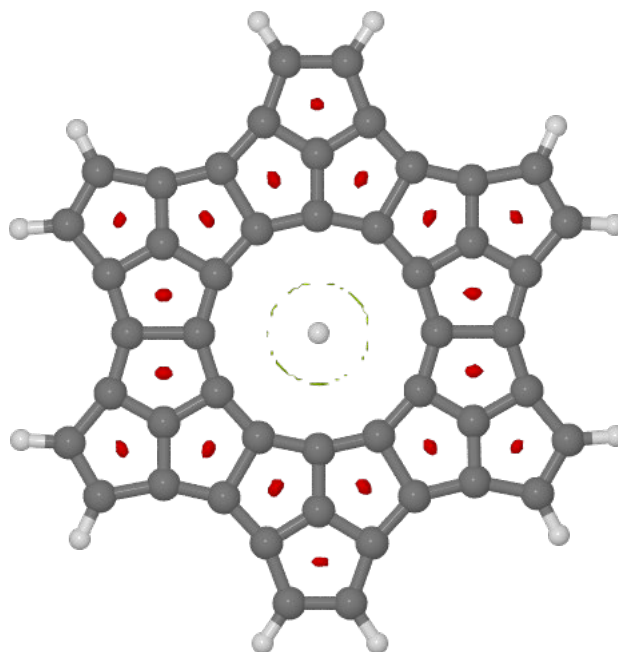


FIGURE 3.8 – Isosurface (cutoff of 0.5 e Bohr⁻³) of the NCI index for the C₂-pent···H₂ complex when the monomers are separated by 5.0 Å.

3.6 Permeance and Selectivity

The contribution from electrostatic, inductive and dispersive effects towards the stabilization of the interaction between the pore structure and the gas molecule counterbalance the influence of the exchange-repulsion. In this case, this feature seems to suggest an inversion of the expected behavior: the diffusion barrier towards hydrogen is 1.0 kcal mol⁻¹ lower in energy for the C₂-pent pore compared to C₂-square, whose structure presents a larger pore size. This small difference between the diffusion energy barriers is enough to grant specific permeability and selectivity properties for each porous membrane. Using the calculated diffusion energy barriers (E_{diff}) and the Arrhenius Equation ($A = A_0 \exp(-E_{\text{diff}}/RT)$), in which we considered the same prefactor A_0 for both membranes (LI *et al.*, 2010b; BLANKENBURG *et al.*, 2010)), it is possible to estimate the selectivity ($S = A_{\text{pent}}^{\text{H}_2} / A_{\text{square}}^{\text{H}_2}$) towards H₂ between the proposed porous structures. At 298 K, C₂-pent presents a performance 6.5 better than C₂-square towards the diffusion of H₂.

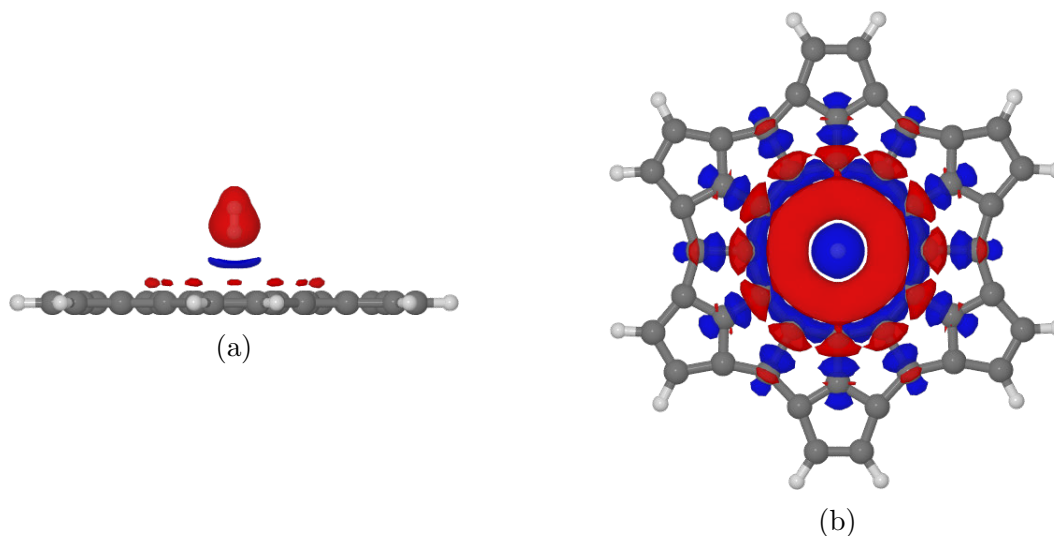


FIGURE 3.9 – Analysis of the polarization of the electron density as a function of the separation distance between C₂-pent and H₂: (a) Separation of 2.6 Å; (b) Separation of 0.0 Å. The isovalue used was 0.001 e Bohr⁻³. Blue and red regions indicate density gain and loss, respectively, in comparison to the isolated systems.

Finally, this feature is illustrated in Figure 3.10, which displays the permeance of H₂ for both pores as a function of temperature according to the kinetic theory of gases, considering an incoming H₂ pressure of 300 kPa and a pressure difference of 100 kPa between the two sides of the membranes (MENG *et al.*, 2016). Despite the apparently small difference of only 1.0 kcal mol⁻¹ between the diffusion barriers of C₂-pent and C₂-square, their permeance, at 298 K, are 0.16 and 0.03 mol m⁻² s⁻¹ Pa⁻¹, respectively. These results indicate that the fused-pentagon structure presents a permeance five times higher than the C₂-square pore, despite having a smaller pore size. Furthermore, compared to the industrially acceptable permeance for gas separation (6.7×10^{-9} mol m⁻² s⁻¹ Pa⁻¹, dashed line in Figure 3.10) (ZHU, 2006), one can see that both membranes are promising for industrial applications, given that, for the whole range of temperatures analyzed, such minimum criteria for permeance is met.

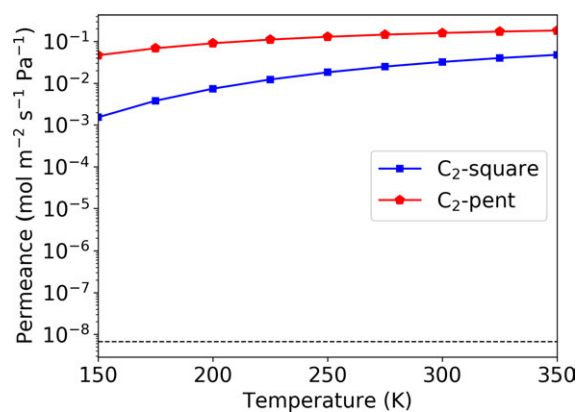


FIGURE 3.10 – H₂ permeance versus temperature for C₂-square (blue) and C₂-pent pores (red). The dashed line represents the industrially acceptable permeance for gas separation with a separability of 6 (ZHU, 2006).

4 Barrier Height and DFT Flavors

4.1 Kekulene Structure

As stated on the previous chapters of, we optimized the kekulene (C_{24}) structure at the MP2/def2-tzvp level of methodology (Figure 4.1). In this section we will concentrate on the how different flavors of exchange-correlation functionals, as well as the inclusion of Hartree-Fock exchange, might influence the diffusion energy barrier. Moreover, we will compare the DFT results, which already include intramolecular correlation effects, to the interaction energy computed at the SAPT0 level. The C_{24} membrane will interact with six different approaching systems: Ar, Ne, He, H_2 , N_2 and CO_2 .

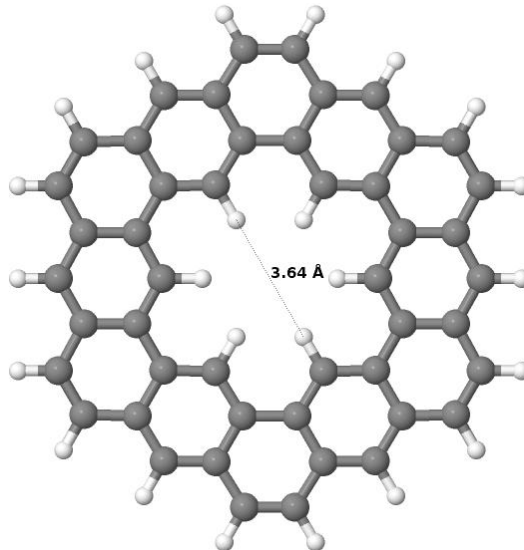


FIGURE 4.1 – The kekulene (C_{24}) pore structure, with its internal H-H distance of 3.64 Å.

4.2 Interaction with gas molecules

Before presenting the analysis of the interaction energy of the $C_{24} \cdots$ gas complex, a few remarks on the optimized geometry of the pore are necessary. As a geometrical measure of

the π -electron delocalization, we analyse in Figure 4.2 how much each C-C bond deviates from the resonance bond length in benzene (which is around 1.4 Å). The more red (blue) the color of the bond, the shorter (larger) the length of it when compared to 1.4 Å. Based on these results, the interior and exterior of the pore seem to be conjugate, which might be an indicative that the C_2 structure is characterized by a strongly polarizable π -electron cloud, similarly to other extended conjugated systems such as graphene.

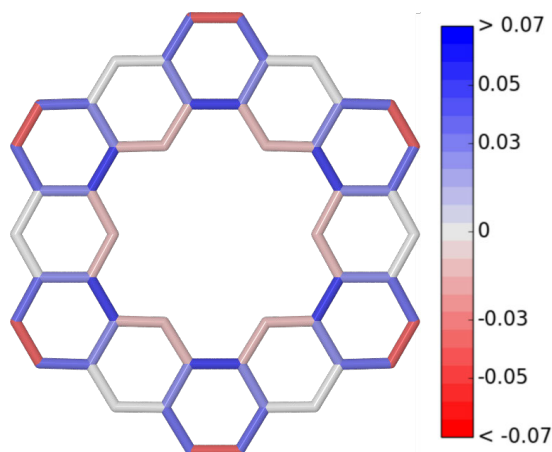


FIGURE 4.2 – C-C bond length of the C_2 structure relative to 1.4 Å. Blue (red) regions indicate larger (shorter) bond when compared to the benzene resonant C-C bond length.

4.2.1 $C_2 \cdots Ar$

4.2.1.1 SAPT and DFT results

The first approaching system that will be analyzed in the present study is the argon gas. Despite being too large (its van der Waals radius is estimated to be 1.88 Å), it could be considered as a limiting case and will be used as a model for the analysis and discussion drawn in this section. It is important to emphasize that, as a first approximation, structural relaxation effects have been accounted, such that the whole geometry of each pore-gas molecular complex was kept fixed during the calculations of the potential energy surface.

Performing DFT calculations with several different functionals (PBE0, B2PLYP-D3, B3LYP-D3, wB97X-D, wPBE-D3, PBE0+vdW-TS and PBE0+MBD) associated to the jun-cc-pVDZ basis set and SAPT0(HF)/jun-cc-pVDZ, we were able to obtain the potential energy surface (Figure 4.3) as described in chapter 2. It has to be noted that, in general, there is a good agreement between the results obtained at different levels methodologies and energy barrier for the diffusion process through the membrane is roughly 90 kcal mol⁻¹ (or 3.83 eV), which is an impractical value for industrial separation purposes. According to (JIAO *et al.*, 2013), an acceptable diffusion energy barrier would be 0.6-0.7 eV (14-16.5

kcal mol⁻¹).

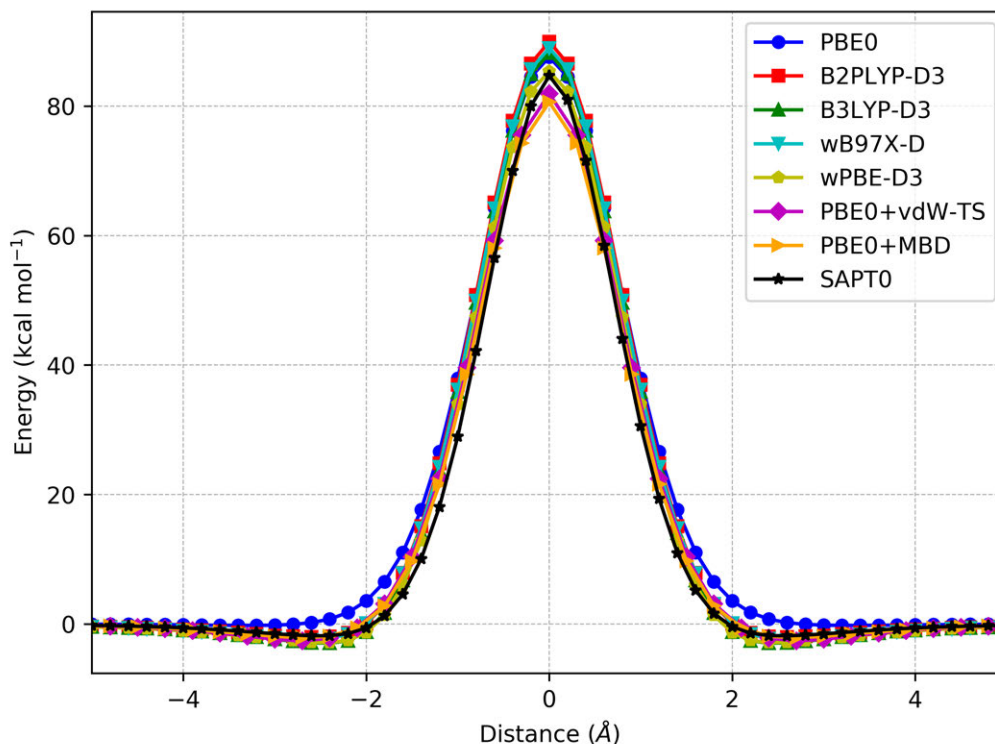


FIGURE 4.3 – $C_2 \cdots Ar$ Potential Energy Surface calculated at different methodologies.

A closer look at the 2.5 Å region of the Figure 4.3 suggest the existence of a local minimum (Figure 4.4). It can also be pointed out that the PBE0/jun-cc-pVDZ curve is the only one that does not seem to predict the existence of such well. Since this is the only functional that does not account for dispersion corrections, it is likely that the nature of this minimum is due to, or at least dominated by, van der Waals interactions between the two complexes (hence forth namely monomers). The other methodologies in the present analysis suggest that the minimum well is about -2.0 kcal mol⁻¹. It has to be pointed out that, the nature of such minimum well has never been discussed in depth.

In order to study the nature of the minimum, the total SAPT0(HF)/jun-cc-pVDZ interaction energy has been decomposed in its main components (electrostatics, exchange, induction and dispersion), as illustrated in Figure 4.5. The red curve indicates the exchange energy component of the total interaction energy and it could also be interpreted as the steric hindrance to the spatial overlap of the wavefunctions of the two monomers. In our case, when the two complexes are at the same plane, the exchange is the most relevant component of the interaction energy and is, as expected, highly repulsive (more than 150.0 kcal mol⁻¹). Despite this, the other energy components, specially the electrostatics term (-50.0 kcal mol⁻¹), play a major role in trying to stabilize and bind the two systems together. This behavior could be explained by the huge electron density concentrated on the argon atom due to its size. A closer examination of the region of the

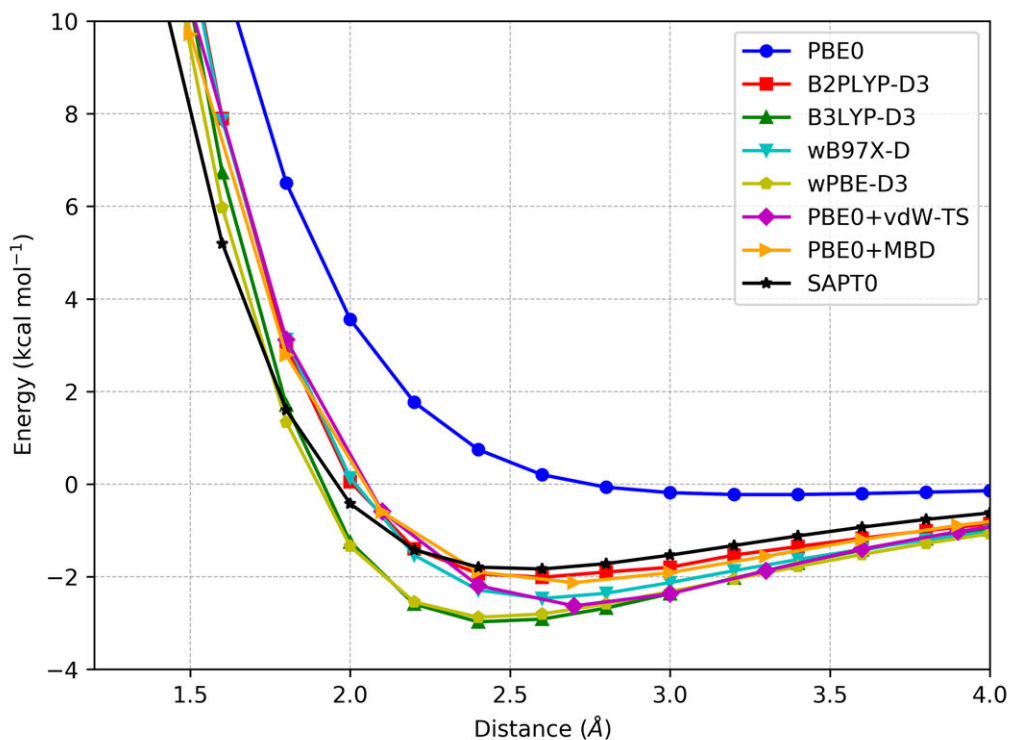


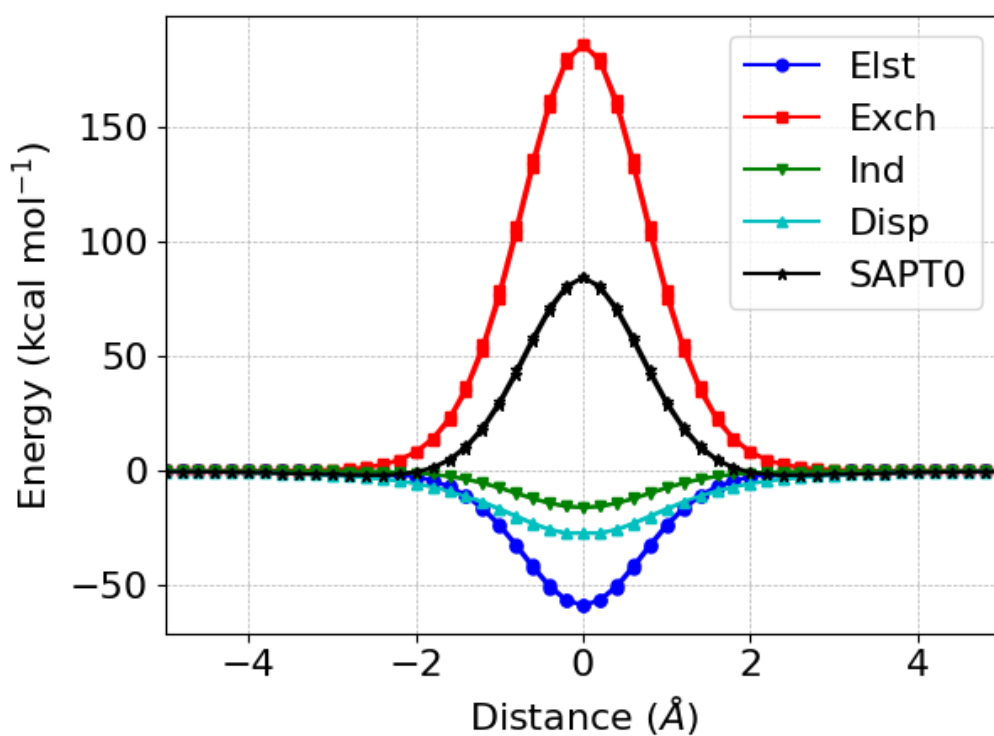
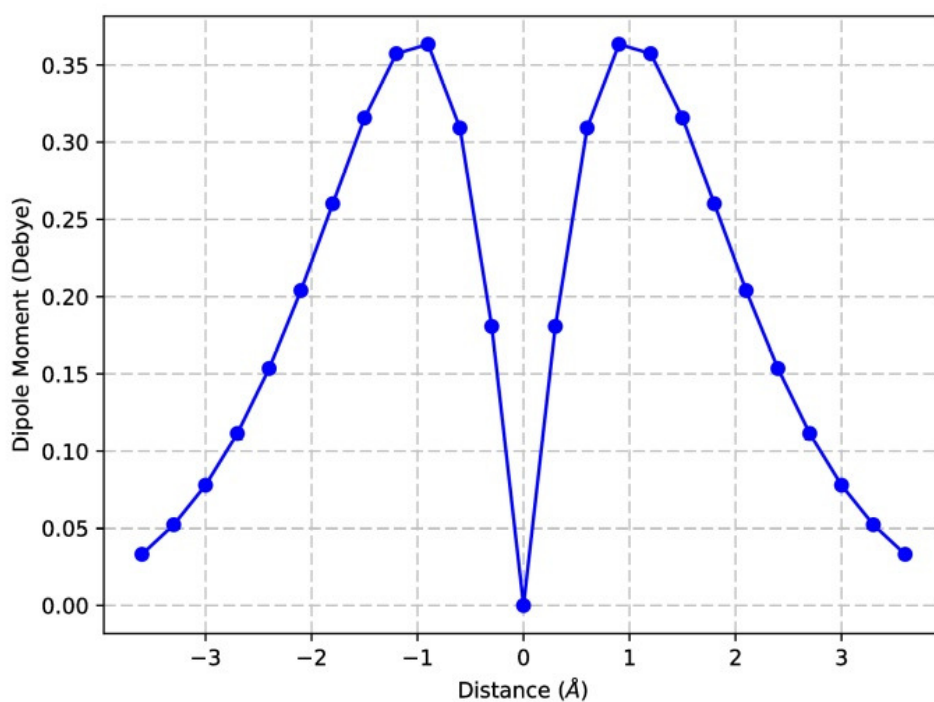
FIGURE 4.4 – $C_2 \cdots Ar$ Potential Energy Surface around the minimum well region.

potential energy surface around 2.5 \AA indicates that the attractive dispersion component of the total energy is still present, whereas the other ones have almost been completely smeared out. Therefore, in this case, the balance between the exchange and dispersion components is the most relevant quantity to explain the existence of the minimum well observed in Figure 4.3).

Furthermore, due to the behavior presented by the induction component (green curve on Figure 4.5), one could expect that the dipole moment of the supermolecule composed by the two complexes (henceforth namely as dimer) would reproduce the existence of the minimum on the potential energy surface. Figure 4.6 illustrates the behavior of the dipole moment, calculated at the PBE0+vdW level of theory, of the dimer as the two monomers are brought together. Although there is no clear correlation between the minimum well at the 2.5 \AA and the dipole moment, it could be observed a peak of 0.35 Debye at 0.9 \AA .

4.2.1.2 Dispersion corrections for $C_2 \cdots Ar$ system

For the $C_2 \cdots Ar$ system in particular, we have also tried to analyze the influence of different schemes for the dispersion correction. Within the density functional theory framework, we have employed types of correction: the vdW-TS scheme is based on empirical factors and, in this sense, it could be considered similar to the approach developed by Grimme and co-workers. In fact, it is formally identical to the DFT-D2 method, but

FIGURE 4.5 – $C_2 \cdots Ar$ SAPT0 and energy components PESFIGURE 4.6 – $C_2 \cdots Ar$ total dipole moment computed with PBE0+vdW

the dispersion coefficients and damping functions are charge-density dependent. Hence, the vdW-TS approach is able to account for contributions of atoms due to their local chemical environment. The second approach used is the many-body dispersion (MBD)

method., which exploits the coupled Quantum Harmonic Oscillator model Hamiltonian to compute the the contribution of van der Waals effects to the total energy. Figure 4.7 and 4.8 illustrates the results obtained at the PBE0, PBE0+vdW-TS, PBE0+MBD and SAPT0 levels of theory. It is worth-noticing that, while the inclusion of the dispersion component is of utmost importance in order to correctly describe the behavior of the total interaction energy, especially at the minimum well region, where, from the SAPT0 analysis, we see that the other components play only a minor role and vdW effects are most prominent, the type (empirical of *ab initio*) of the scheme used does not seem to affect the interaction energy in a significant manner.

Moreover, it is worthy of attention the fact that, within the SAPT formalism, the computation of the coupled-perturbed terms to account for the dispersion component is the main bottleneck that accounts for the total computational cost of the methodology. Thus, substitution of *ab initio* dispersion by the empirical schemes might be a possible strategy to reduce computational time, which would allow the methodology to be applicable to even larger systems.

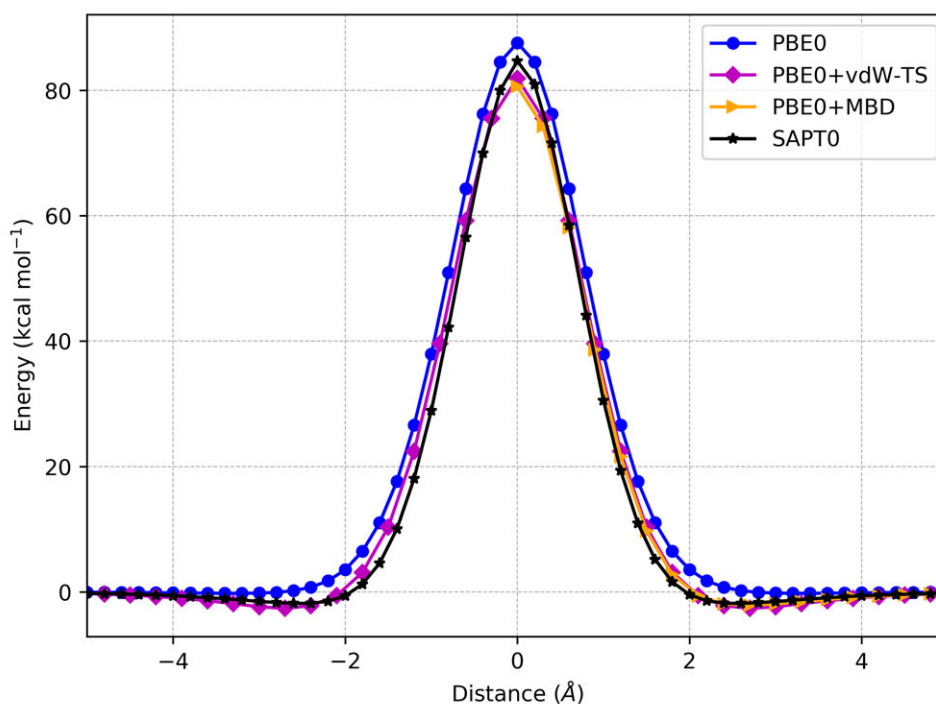


FIGURE 4.7 – Interaction energy for the $C_2 \cdots Ar$ system using different schemes for the dispersion contribution.

4.2.1.3 Summary

Table 4.1 presents the summarized results for the interaction between the C_2 pore structure and argon, obtained at different levels of theory. Here, we show the diffusion

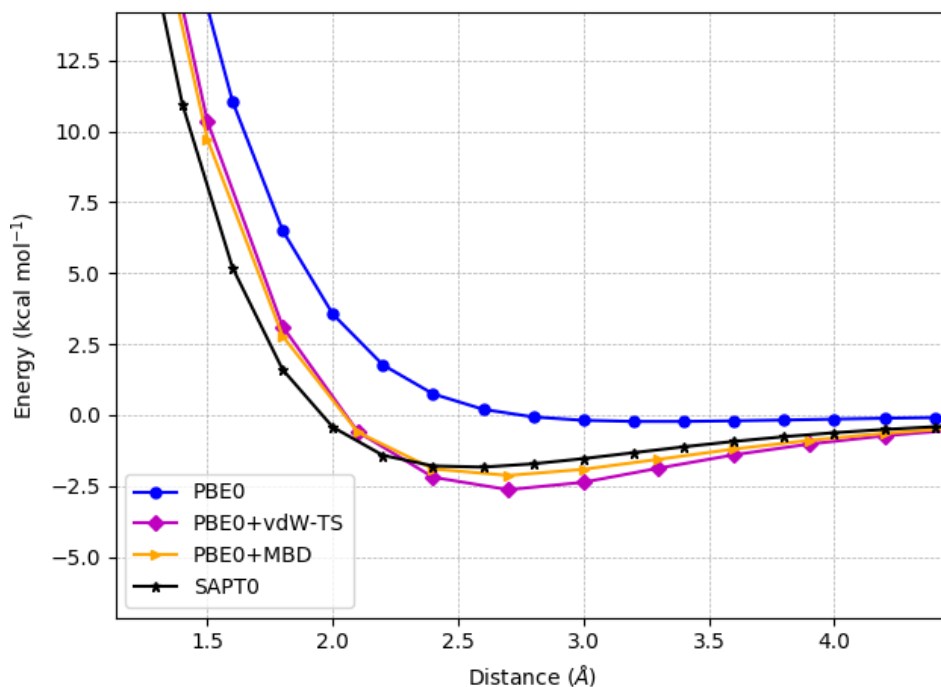


FIGURE 4.8 – A closer look at the minimum well region of the potential energy surface of the total interaction energy for the $C_2 \cdots Ar$ system using different schemes for the dispersion contribution.

energy barrier, the position of the minimum well on the potential energy surface as well as the depth of such minimum. All methods tested resulted in a minimum well around the region between 2.4 Å and 2.6 Å, except for PBE0, which does not account for dispersion effects. The diffusion energy barrier maximum deviation was around 10 kcal mol⁻¹, corresponding to a deviation of 12.5% with respect to the SAPTO value.

TABLE 4.1 – Summary for the interaction energy between C_2 and Ar: diffusion energy barrier (ΔE_{diff}), minimum well position (r_{vdW}) and minimum well depth (ΔE_{vdW})

| Method | ΔE_{diff} (kcal mol ⁻¹) | r_{vdW} (Å) | ΔE_{vdW} (kcal mol ⁻¹) |
|-----------------|---|---------------|--|
| PBE0 | 87.6 | 3.2 | -0.22 |
| PBE0+vdW-TS | 81.9 | 2.7 | -2.63 |
| PBE0+MBD | 80.6 | 2.7 | -2.13 |
| ω PBE-D3 | 85.4 | 2.4 | -2.87 |
| B3LYP-D3 | 88.2 | 2.4 | -2.97 |
| B2PLYP-D3 | 89.9 | 2.6 | -2.01 |
| ω B97X-D | 89.0 | 2.6 | -2.47 |
| SAPTO | 80.0 | 2.6 | -1.83 |

4.2.2 $C_2 \cdots Ne$

From this point forward, we will try to draw the same analysis for the other systems focused on the previous subsections of this chapter. Neon (Ne) is characterized by van der Waals radius of 1.54 Å, which is about 22% smaller than the vdW radius of the Argon atom. Figure 4.9 illustrates the potential energy surface for the $C_2 \cdots Ne$ system at different levels of theory. Figure 4.9 illustrates the results for the potential energy curve obtained at different levels of methodology. It is possible to notice that, despite predicting the same qualitative behavior, quantitatively there seems to be a disagreement between the SAPT0/jun-cc-pVDZ results and the ones obtained with the dispersion corrected functionals in the region of the minimum well (Figure 4.10). Initially this differences of about 0.6-0.7 kcal mol⁻¹ could be explained by the limitations of each level of theory used. However, the good agreement of the PBE0/jun-cc-pVDZ (which does not include dispersion) and SAPT0(HF)/jun-cc-pVDZ (which includes *ab initio* dispersion through second-order perturbation theory) might also suggest a mechanism of error compensation and a deeper analysis of the effects of exact exchange on the polarization of each monomer is required to understand this “anomalous” behavior.

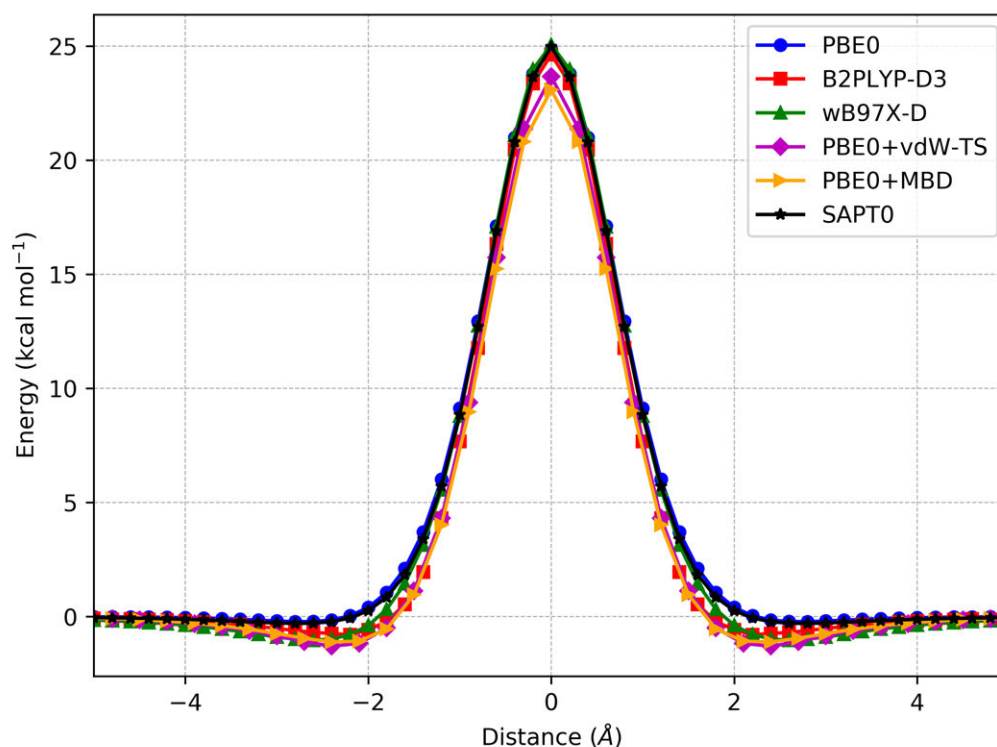


FIGURE 4.9 – $C_2 \cdots Ne$ Potential Energy Surface calculated at different methodologies.

The total energy barrier towards diffusion through the pore, shown in Figure 4.11m is about 25.0 kcal mol⁻¹, representing a reduction of almost 70% compared when compared to the results obtained for the $C_2 \cdots Ar$ system, despite the reduction of only 22% on the vdW radius of the approaching system. Moreover, it has to be pointed out that

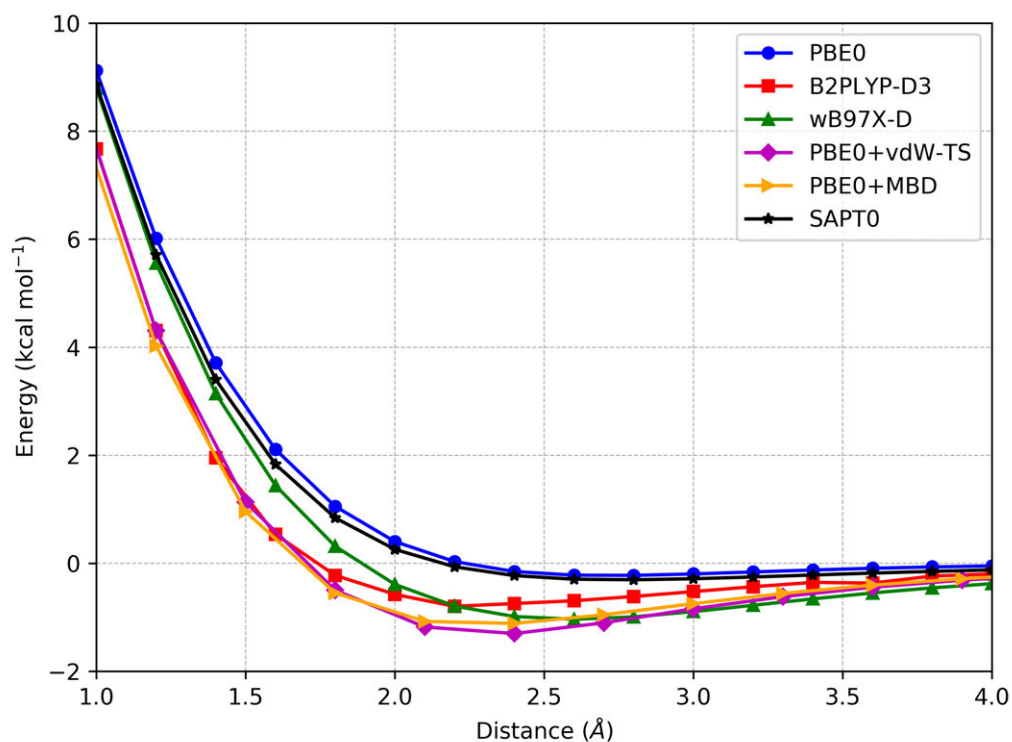


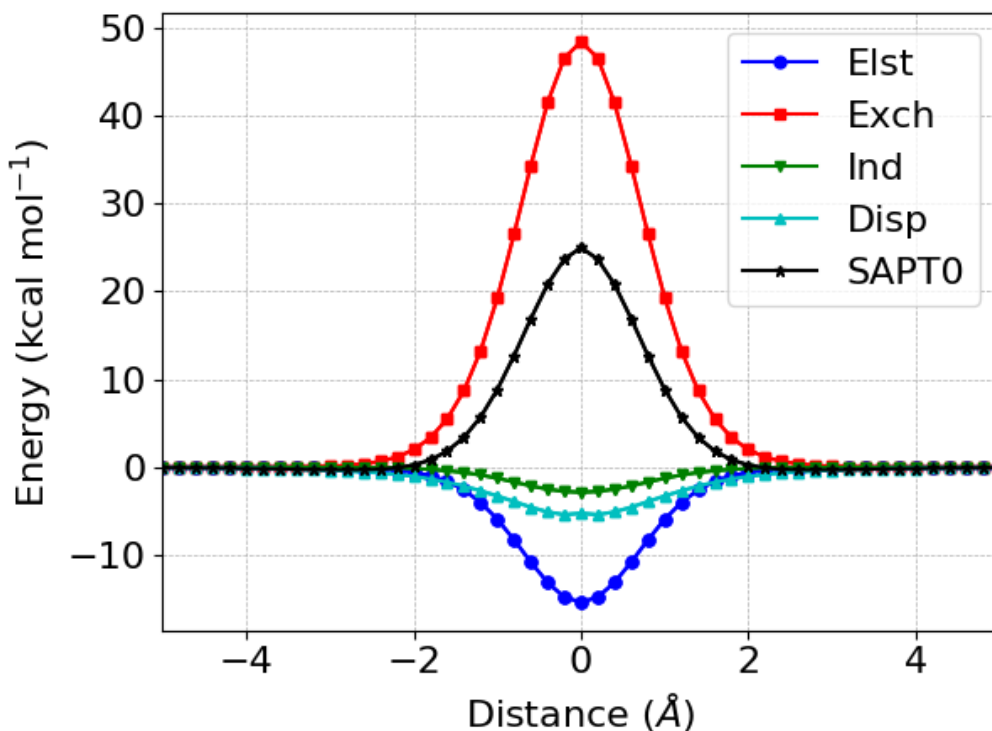
FIGURE 4.10 – $C_2 \cdots Ne$ Potential Energy Surface around the minimum well region (2.5 Å).

attractive electrostatic effects are the most relevant energy component contributing for the stabilization of the system. Induction and dispersion terms can not be neglected, especially the dispersion at long distances, as shown by a closer inspection of Figure 4.11 around the region of the minimum well (2.5 Å).

Table 4.2 presents the summarized results for the interaction between the C_2 pore structure and neon, obtained at different levels of theory. Here, we show the diffusion energy barrier, the position of the minimum well on the potential energy surface as well as the depth of such minimum. All methods tested resulted in a minimum well around the region between 2.4 Å and 2.8 Å. The diffusion energy barrier maximum deviation was around $1.9 \text{ kcal mol}^{-1}$, corresponding to a deviation of 8% with respect to the SAPT0 value. In this case, we also see a maximum deviation of $0.8 \text{ kcal mol}^{-1}$ for the well depth value with respect to SAPT0.

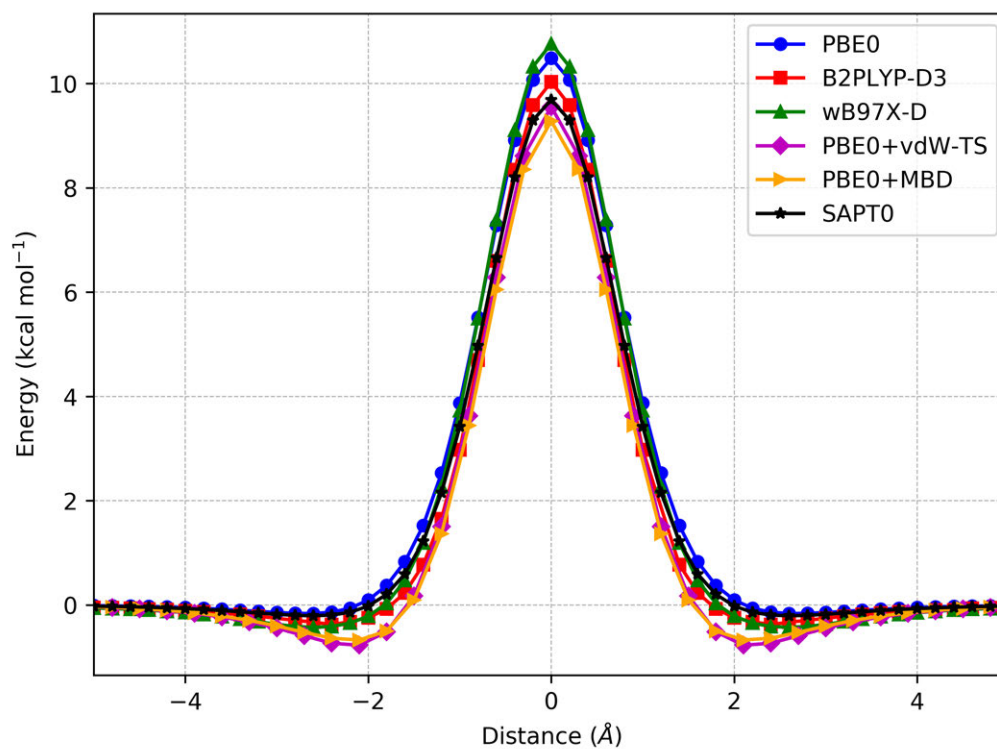
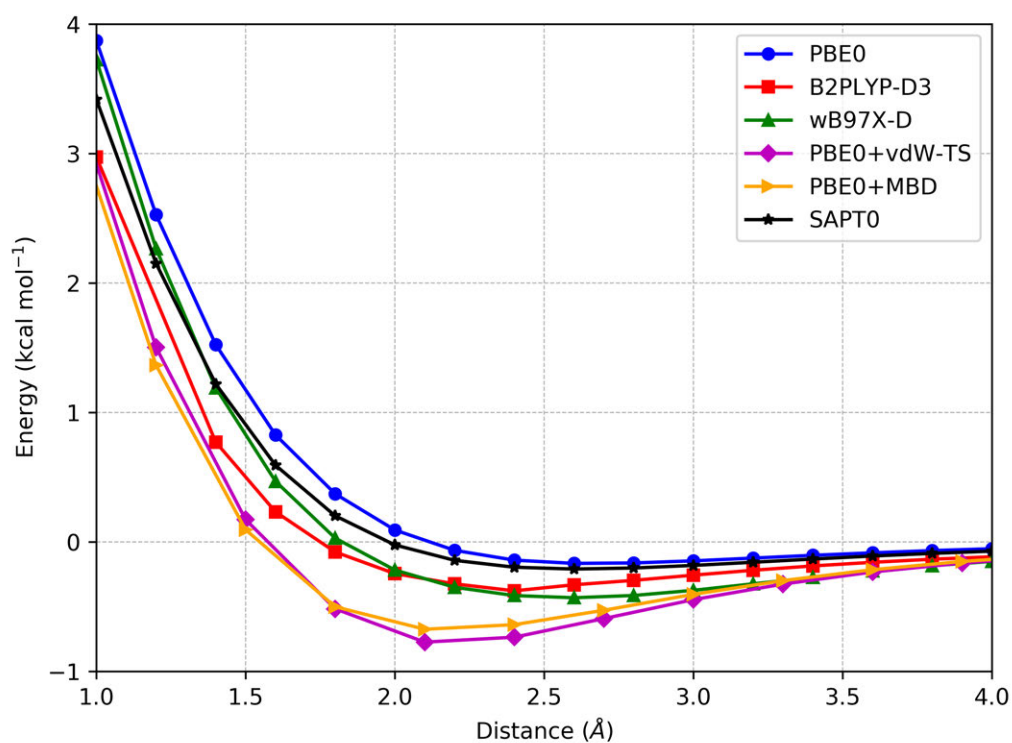
4.2.3 $C_2 \cdots He$

Figure 4.12 represents the total interaction energy for the $C_2 \cdots He$ calculated at several levels of theory. The comparison between SAPT0(HF)/jun-cc-pVDZ and the PBE0+vdW-TS shows that, at the plane of the membrane (which corresponds to $z = 0.0 \text{ Å}$), the predicted energy barriers are in good agreement. On the other hand, the

FIGURE 4.11 – $C_2 \cdots Ne$ SAPT0 and energy components PES.TABLE 4.2 – Summary for the interaction energy between C_2 and Ne : diffusion energy barrier (ΔE_{diff}), minimum well position (r_{vdW}) and minimum well depth (ΔE_{vdW})

| Method | ΔE_{diff} (kcal mol $^{-1}$) | r_{vdW} (Å) | ΔE_{vdW} (kcal mol $^{-1}$) |
|-----------------|---------------------------------------|---------------|--------------------------------------|
| PBE0 | 24.8 | 2.8 | -0.22 |
| PBE0+vdW-TS | 23.7 | 2.4 | -1.30 |
| PBE0+MBD | 23.1 | 2.4 | -1.11 |
| B2PLYP-D3 | 24.6 | 2.2 | -0.80 |
| ω B97X-D | 25.1 | 2.6 | -1.03 |
| SAPT0 | 25.0 | 2.8 | -0.30 |

SAPT0 barrier seems to be $1.0 \text{ kcal mol}^{-1}$ lower than the ones obtained at the PBE0 and B2PLYP-D3 levels of theory. This behavior, however, is inverted at long distances: at the regions near the minimum well, SAPT0 predicts almost the same value as PBE0, whereas it is $0.5 \text{ kcal mol}^{-1}$ off from the PBE0+vdW-TS and PBE0+MBD results (Figure 4.13). One might argue that such small differences could be neglected, once they are below the accuracy of most quantum chemistry methods. Another possible argument, however, would be the particular effects introduced by several parameters used to construct a given functional. For instance, the double-hybrid with dispersion correction B2PLYP-D3 functional contains terms to account for a fraction of the HF exchange and for a fraction of the MP2 correlation on the total energy of the system. Tuning such coefficients might affect in a different fashion the polarization of the electron density the separation distance between the monomers is changed.

FIGURE 4.12 – $C_2 \cdots He$ Potential Energy Surface calculated at different methodologiesFIGURE 4.13 – $C_2 \cdots He$ minimum well around the 2.5 Å region of the PES

Finally, the decomposition of the SAPTO(HF)/jun-cc-pVDZ total interaction energy is pictured on Figure 4.14. Also in this case, the most relevant energy component is

the exchange, indicating that the electron density is able to crowd the pore of the C_2 structure in such a way to result in a diffusion barrier of about $20.0 \text{ kcal mol}^{-1}$ towards He (which present a vdW radius of 1.40 \AA). Even though, the literature indicates that such barrier would not be an obstacle to the industrial application of this membrane for He separation (JIAO *et al.*, 2013). Differently from what has been observed for the other systems analyzed so far, electrostatic and dispersion components of the total interaction energy account almost with the same weight towards the stabilization of the complex when the He atom is on the same plane as the unrelaxed pore structure. Moreover, although He is the less polarizable specie between the noble gases studied here, the induction term can not be neglected. It is also important to point out that, as the we moved from Ar to He, *i.e.*, as the probe gas was becoming smaller, the weight of the exchange-repulsion towards the total interaction energy has also decreased. On the other hand, the contribution from the other components increased and became a major factor to stabilize the dimer complex. In this sense, our idea of using the exchange-repulsion term as an estimate of the size of the pore is consistent and, as noticed in chapter 3, tuning the electrostatic, induction and dispersion contributions is a powerful strategy in order to achieve enhanced performance for nanoporous membranes.

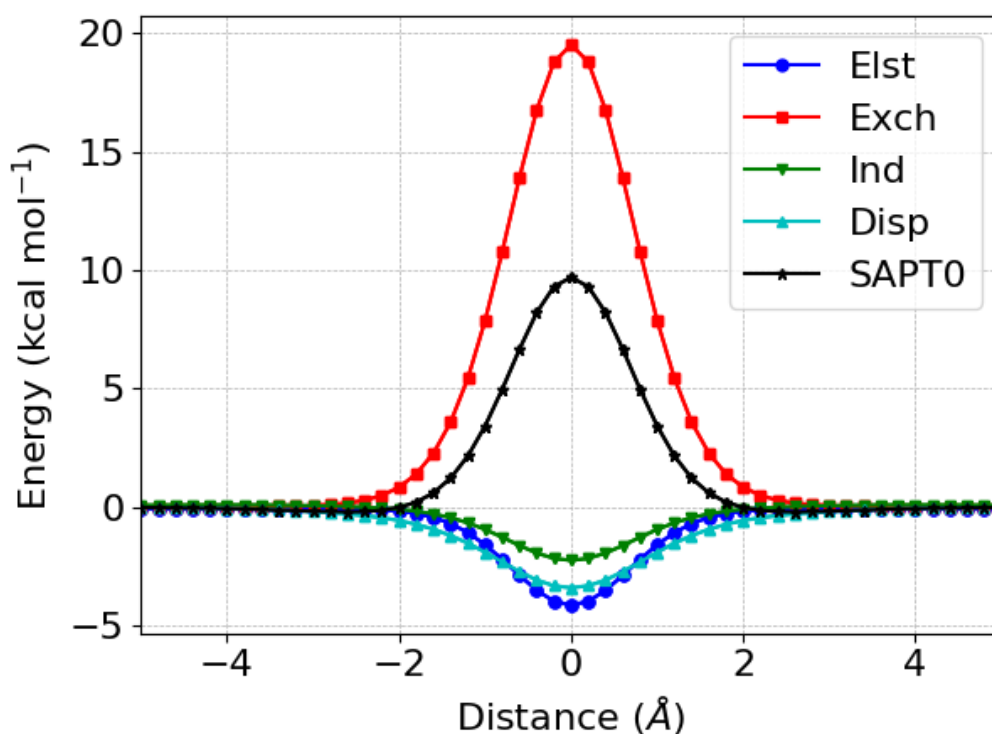


FIGURE 4.14 – $C_2 \cdots \text{He}$ SAPT0 and energy components PES.

Table 4.3 presents the summarized results for the interaction between the C_2 pore structure and helium, obtained at different levels of theory. Here, we show the diffusion energy barrier, the position of the minimum well on the potential energy surface as well as the depth of such minimum. All methods tested resulted in a minimum well around the

region between 2.1 Å and 2.6 Å. The diffusion energy barrier maximum deviation was around 1.5 kcal mol⁻¹, corresponding to a deviation of 15% with respect to the SAPT0 value. In this case, we also see a maximum deviation of 0.5 kcal mol⁻¹ for the well depth value with respect to SAPT0.

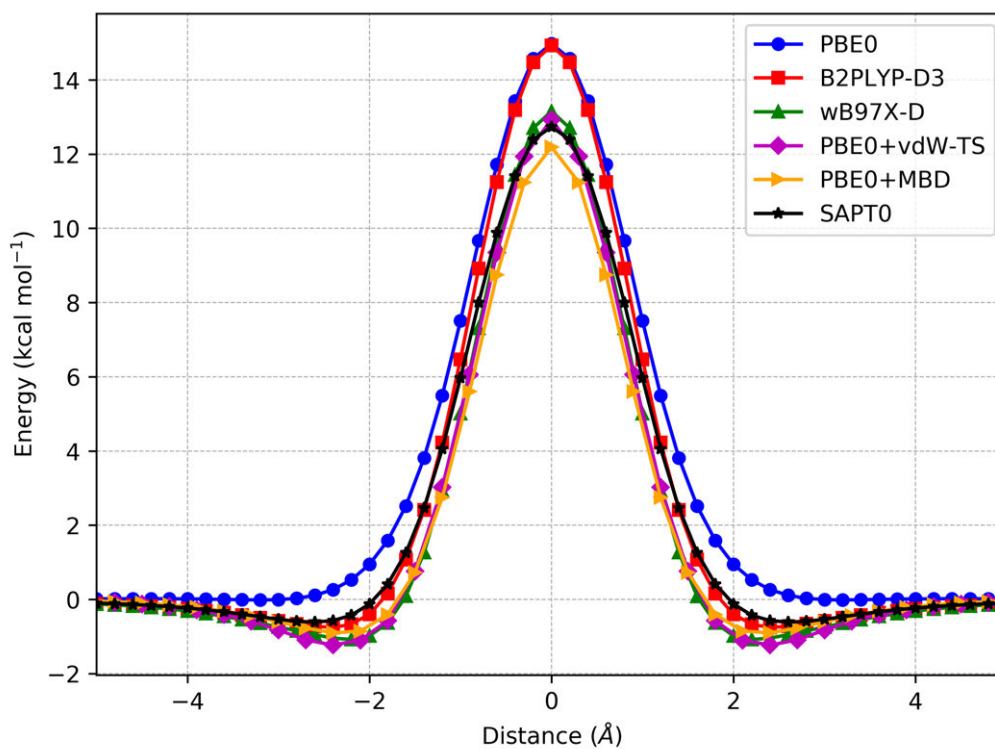
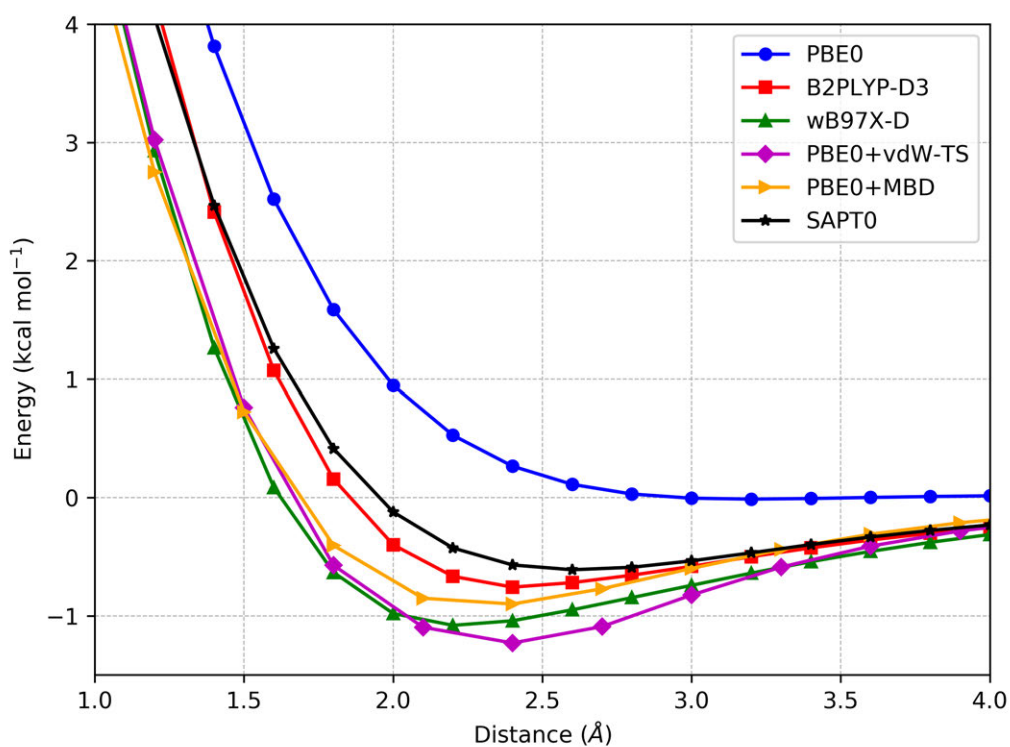
TABLE 4.3 – Summary for the interaction energy between C₂ and He: diffusion energy barrier (ΔE_{diff}), minimum well position (r_{vdW}) and minimum well depth (ΔE_{vdW})

| Method | ΔE_{diff} (kcal mol ⁻¹) | r_{vdW} (Å) | ΔE_{vdW} (kcal mol ⁻¹) |
|-----------------|---|---------------|--|
| PBE0 | 10.5 | 2.6 | -0.17 |
| PBE0+vdW-TS | 9.6 | 2.1 | -0.77 |
| PBE0+MBD | 9.3 | 2.1 | -0.67 |
| B2PLYP-D3 | 10.0 | 2.4 | -0.38 |
| ω B97X-D | 10.8 | 2.6 | -0.43 |
| SAPT0 | 9.7 | 2.6 | -0.21 |

4.2.4 C₂ ··· H₂

After analyzing only noble gases, we will start the study of the interaction between homonuclear diatomic gas molecules. Figure 4.15 illustrates the results for the potential energy surface of the C₂ ··· H₂ system computed at different levels of methodologies. It has to be noted that, because of the discrepancy between dispersion-less methods (such as PBE0) and the other results (ω B97X-D and SAPT0), one could expect that the dispersion component of the total interaction energy plays a major role in the understanding of the forces “binding” the two monomers together. In fact, it should be emphasized that, as the probe gas gets smaller, the weight of the attractive terms that contributes to the total interaction energy increases and such discrepancies might become more evident. A closer look at the minimum well region (Figure 4.16) indicates that, despite their close agreement at the peak region, ω B97X-D and SAPT0 results presents a small discrepancy of about 0.5 kcal mol⁻¹ at the 2.5 Å region of the PES. A first hypothesis that could explain such behavior is the limitation of the different treatments of the dispersion term: while SAPT0 computes such component by an *ab initio* procedure, the ω B97X-D dispersion represents the addition of an empirically parametrized energy component after the self-consistent field (SCF) procedure to obtain the Kohn-Sham orbitals and energy.

Finally, Figure 4.17 represent the energy components of the total interaction energy computed at the SAPT0(HF)/jun-cc-pVDZ level. The diffusion energy barrier is a bit higher than 10.0 kcal mol⁻¹ and the exchange term is the most important energy component for the total interaction energy at small distances. Even so, it is not as dominant as the contribution of such term for the limiting case of argon. Hence, dispersion and electrostatics effects are equally important to analyze the behavior of the potential energy

FIGURE 4.15 – $C_2 \cdots H_2$ Potential Energy Surface calculated at different methodologies.FIGURE 4.16 – $C_2 \cdots H_2$ minimum well around the 2.5 \AA region of the PES.

surface as the two monomers are brought together. Moreover, it has to be pointed out an apparently a long-range behavior of the dispersion term when compared to the other

systems studied so far.

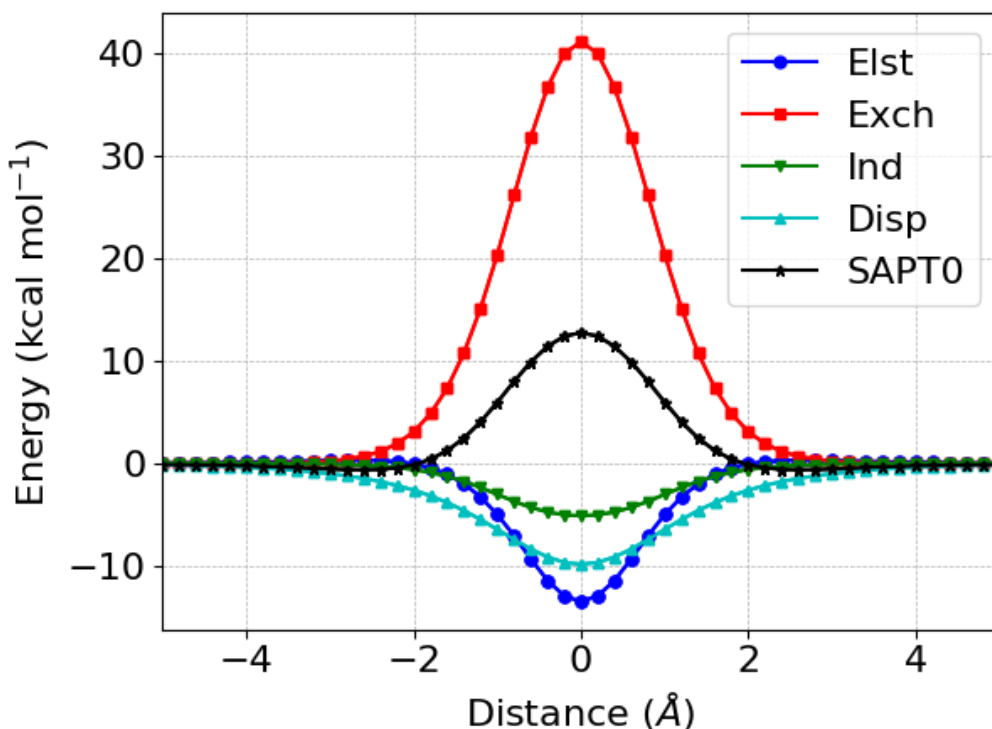


FIGURE 4.17 – $C_2 \cdots H_2$ SAPT0 and energy components PES.

Table 4.4 presents the summarized results for the interaction between the C_2 pore structure and H_2 , obtained at different levels of theory. Here, we show the diffusion energy barrier, the position of the minimum well on the potential energy surface as well as the depth of such minimum. All methods tested resulted in a minimum well around the region between 2.2 Å and 2.6 Å. The diffusion energy barrier maximum deviation was around 2.3 kcal mol⁻¹, corresponding to a deviation of 18% with respect to the SAPT0 value. In this case, we also see a maximum deviation of 0.6 kcal mol⁻¹ for the well depth value with respect to SAPT0.

TABLE 4.4 – Summary for the interaction energy between C_2 and H_2 : diffusion energy barrier (ΔE_{diff}), minimum well position (r_{vdW}) and minimum well depth (ΔE_{vdW})

| Method | ΔE_{diff} (kcal mol ⁻¹) | r_{vdW} (Å) | ΔE_{vdW} (kcal mol ⁻¹) |
|-----------------|---|---------------|--|
| PBE0 | 15.0 | 3.2 | -0.01 |
| PBE0+vdW-TS | 12.9 | 2.4 | -1.23 |
| PBE0+MBD | 12.2 | 2.4 | -0.90 |
| B2PLYP-D3 | 14.9 | 2.4 | -0.76 |
| ω B97X-D | 13.2 | 2.2 | -1.08 |
| SAPT0 | 12.7 | 2.6 | -0.61 |

4.2.5 $C_2 \cdots N_2$

Figure 4.18 illustrates the results for the potential energy surface of the $C_2 \cdots N_2$ system computed at different levels of methodologies. All methodologies that account for the dispersion energy seem to agree at long distances (Figure 4.19), indicating that this component of the total interaction energy seems to be well described by both empirical and *ab initio* approaches. On the other hand, a difference of about $10.0 \text{ kcal mol}^{-1}$ at $z = 0.0 \text{ \AA}$ indicates a poor description of the interaction between N_2 gas and the C_2 pore at short distances. An initial hypothesis to explain the disagreement between DFT and SAPT0 results with respect to the total energy barrier (at $z=0$) would be an incorrect treatment of the induction term in the SAPT0 approach due to significant charge transfer between the two monomers.

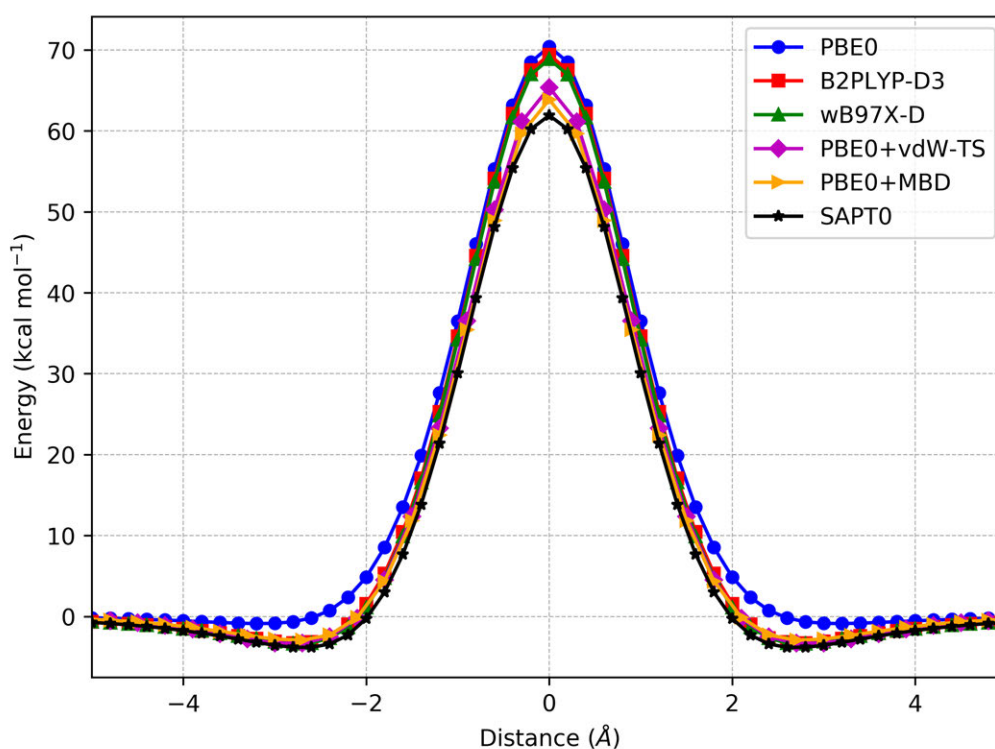


FIGURE 4.18 – $C_2 \cdots N_2$ Potential Energy Surface calculated at different methodologies.

The energy components of the total interaction energy compute at the SAPT (HF)/jun-cc-pVDZ level of theory are shown in Figure 4.20. It is possible to point out that both electrostatics and dispersion effects are equally important in in order to reduce the influence of the $125.0 \text{ kcal mol}^{-1}$ repulsive barrier due to the overlap of the monomers wavefunctions (the exchange term of the total interaction energy). The SAPT approach also predicts a small hump on the induction component can be observed in the green curve of Figure 4.20. This behavior might be explained by the high polarizability of the Nitrogen atoms, since these humps seem to occur at the positions when these atoms are at $z = 0.0 \text{ \AA}$.

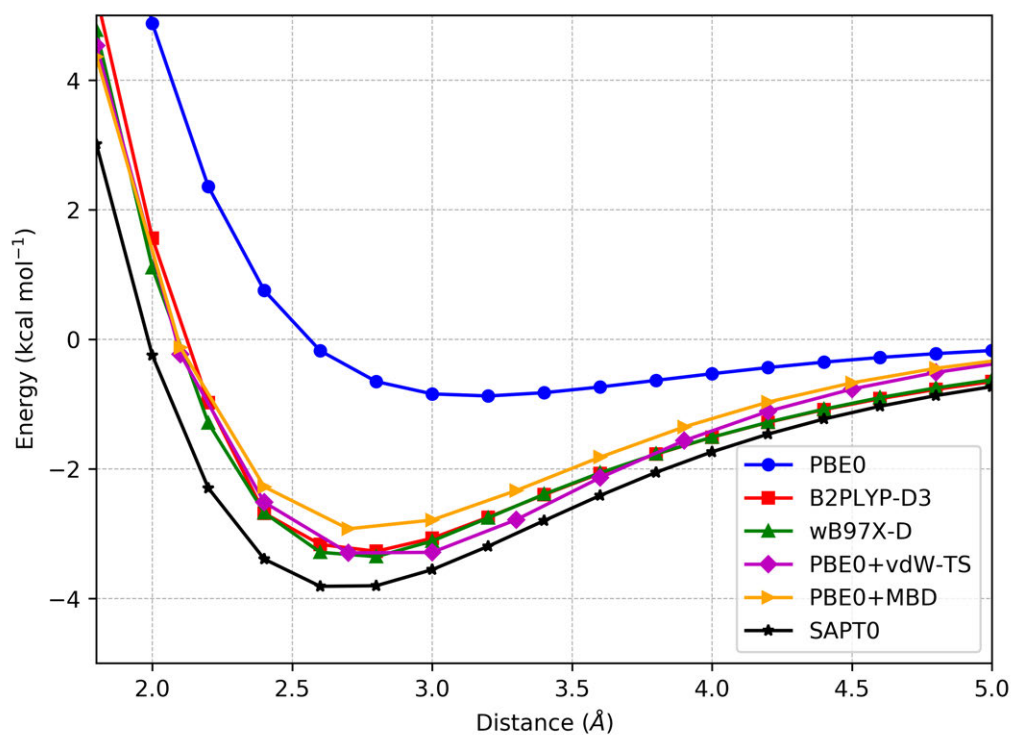


FIGURE 4.19 – $C_2 \cdots N_2$ minimum well around the 2.5 Å region of the PES.

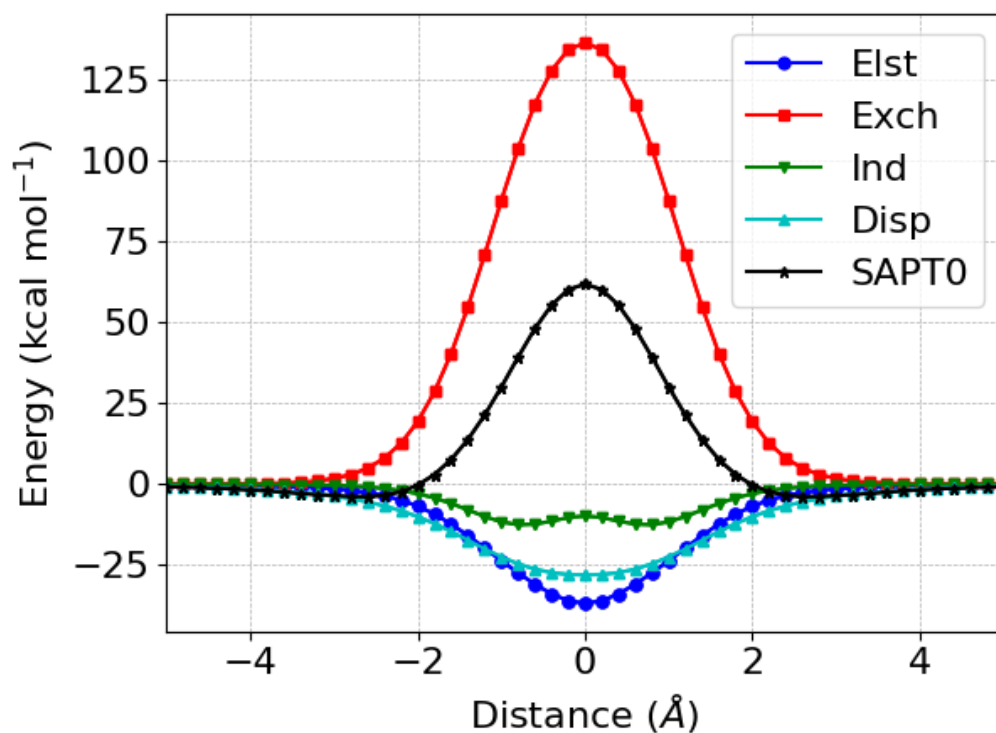


FIGURE 4.20 – $C_2 \cdots N_2$ SAPT0 and energy components PES.

Table 4.5 presents the summarized results for the interaction between the C_2 pore structure and N_2 , obtained at different levels of theory. Here, we show the diffusion energy barrier, the position of the minimum well on the potential energy surface as well

as the depth of such minimum. All methods tested resulted in a minimum well around the region between 2.7 Å and 2.8 Å. The diffusion energy barrier maximum deviation was around 8 kcal mol⁻¹, corresponding to a deviation of 14% with respect to the SAPT0 value. In this case, we also see a maximum deviation of 0.9 kcal mol⁻¹ for the well depth value with respect to SAPT0, if we do not consider the PBE0 result.

TABLE 4.5 – Summary for the interaction energy between C₂ and N₂: diffusion energy barrier (ΔE_{diff}), minimum well position (r_{vdW}) and minimum well depth (ΔE_{vdW})

| Method | ΔE_{diff} (kcal mol ⁻¹) | r_{vdW} (Å) | ΔE_{vdW} (kcal mol ⁻¹) |
|-----------------|---|---------------|--|
| PBE0 | 70.4 | 3.2 | -0.87 |
| PBE0+vdW-TS | 65.4 | 2.7 | -3.30 |
| PBE0+MBD | 63.7 | 2.7 | -2.93 |
| B2PLYP-D3 | 69.4 | 2.8 | -3.27 |
| ω B97X-D | 68.9 | 2.8 | -3.36 |
| SAPT0 | 61.9 | 2.6 | -3.81 |

The C₂⋯N₂ system presents an interesting feature: it can be observed that, at small distances between the two interacting system, some of the DFT values disagree significantly, whereas such disagreement seems to vanish at larger distances. To verify this hypothesis, we analyze the density of states diagram, computed at the ω -B97X-D level of theory, of the interacting C₂⋯N₂ complex and the isolated monomers (Figure 4.21). At small distances, the lowest unoccupied molecular orbital (LUMO) of the dimer seems to be somewhat “contaminated” with orbitals that originally belonged to the N₂ monomer. Such feature is not present at larger distances. Hence, we suspect that this would be related to a charge-transfer between the two interacting system.

At first, we tried to analyze the origins of such charge-transfer issue by means of the SAPT methodology. As presented previously in this work, SAPT’s decomposition of the total interaction energy provides information about the induction energy, which can be divided into a polarization part and a charge-transfer one. By simply performing two separate computations using the dimer and the monomer basis sets, the charge-transfer energy can be estimated by subtracting the induction component related to both computations. Figure 4.22 illustrates the charge-transfer energy associated to the C₂⋯N₂ system as a function of the distance between the pore and the gas molecule. It can be seen that an stabilization of about 8.0 kcal mol⁻¹ is due to this charge-transfer effect. Moreover, Figure 4.22 also shows the LUMO of the dimer system at large and small distances. As expected from the DOS (Figure 4.21), the LUMO of the dimer resembles the LUMO of the pore at large separations, whereas there is a significant mixing between orbitals from the pore structure and the gas molecule at small distance to form the LUMO of the system.

We have also tried to understand such phenomenon by analyzing the difference in

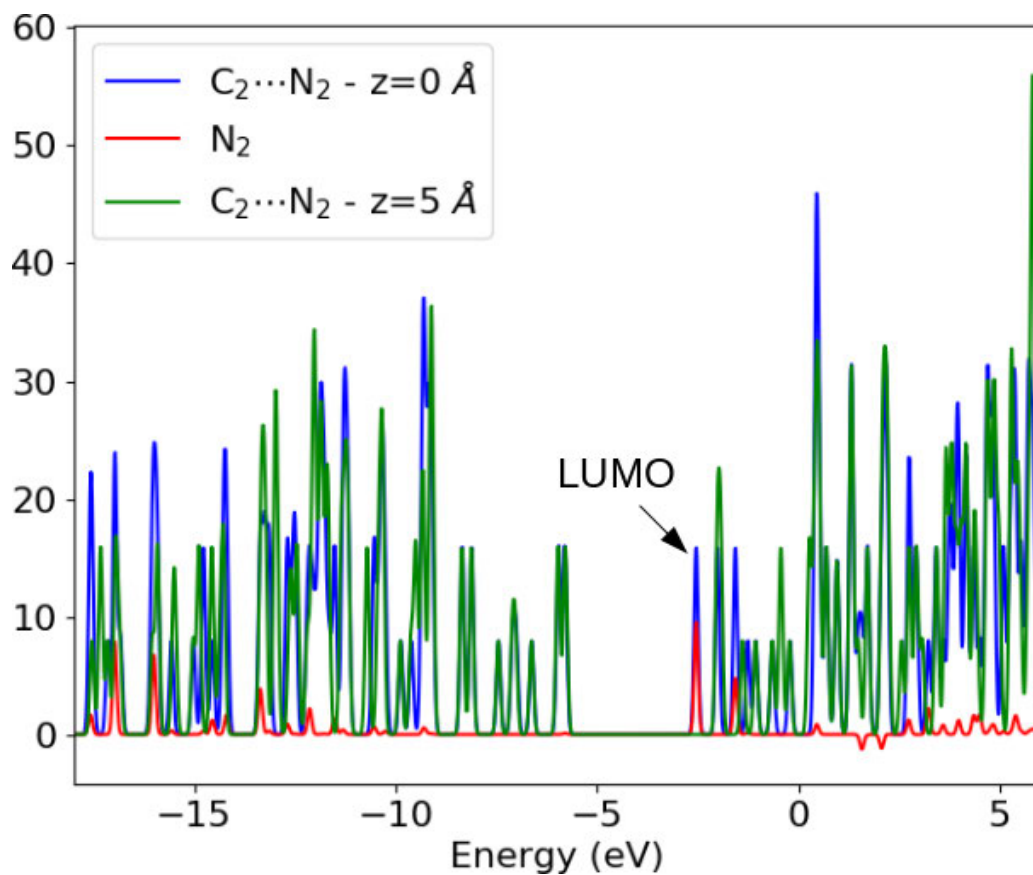


FIGURE 4.21 – ω B97X-D/jun-cc-pVDZ density of states (DOS) diagram of the $C_2 \cdots N_2$ system and its projection on the N_2 orbitals.

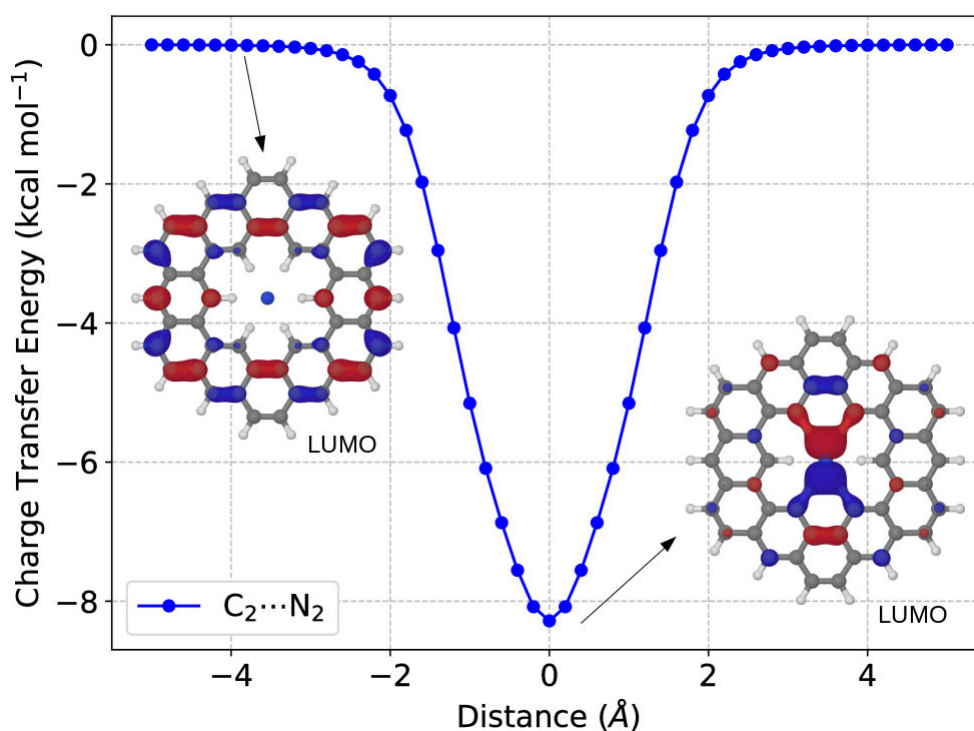


FIGURE 4.22 – SAPT0/jun-cc-pVDZ charge-transfer energy as a function of the distance for the $C_2 \cdots N_2$ system and the LUMO of the dimer at two different distances.

the electronic density distribution of the system and the monomers as a function of the separation between the subsystems. At larger separations, it is reasonable to expect that the difference between the charge density of the dimer and the two monomers should be zero, due to the almost non-interacting character of the dimer at such distance. As the two monomers get closer to each other, one would expect a polarization of the N_2 molecule, building up charge in one of the nitrogen atoms, whilst the other one would lose charge. This behavior is pictured in Figures 4.23a and 4.23b. However, at small distances, Figure 4.23b shows a different behavior. It is worth noticing that, due to the decrease in the electron density between the two monomers, the hypothesis of a covalent bond being formed between the hydrogen of the inner edge of the pore and the nitrogen atoms is not confirmed. On the other hand, we also observe that, at small distances, a polarization of the C-H bond seems to occur on the inner edge of the pore structure. Questions such as the influence of a different functionalization on this edge might arise, but will not be covered in the present study.

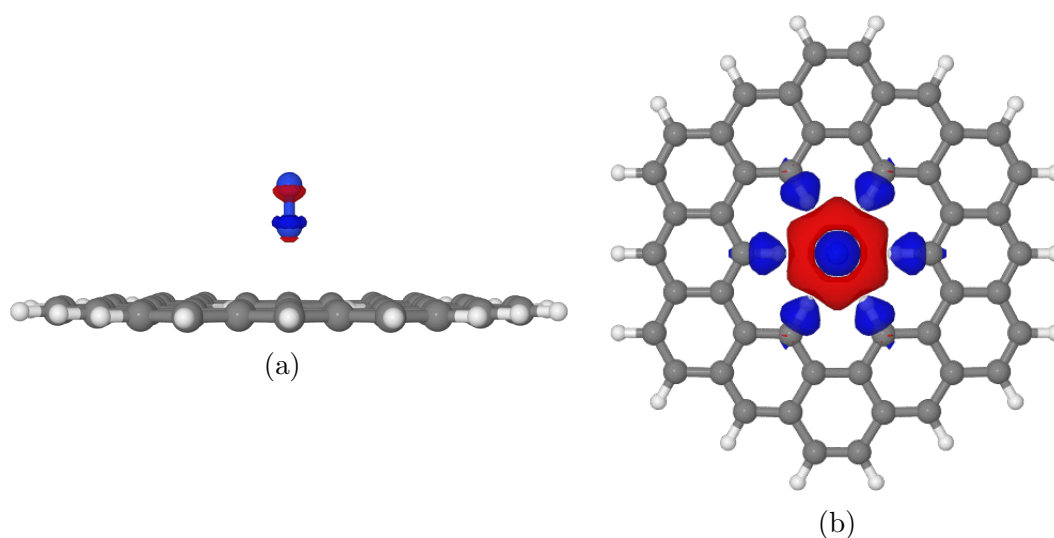


FIGURE 4.23 – ω B97X-D/jun-cc-pVDZ isosurfaces (cutoff of $0.001 e \text{ Bohr}^{-3}$) density difference between the $C_2 \cdots N_2$ and the two monomers: (a) $z = 2.8 \text{ \AA}$; (b) $z = 0.0 \text{ \AA}$. Blue regions indicate a density gain and red regions indicate a density loss.

An alternative way of visualizing the same pattern would be to integrate the electron density and analyze the charge itself as a function of the distance in the z -axis for a given separation between the two monomers, as shown in Figure 4.24. Again, it is possible to notice that the only relevant behavior is the translation of a dipole along the z -axis: a region of positive and negative charge representing the polarization of the N_2 molecule as it gets closer to the pore. However, at closer distances, it is worth pointing out that the build up of positive charge near the plane of the pore, probably due to the polarization of the C-H bonds as noticed previously. Moreover, at $z = 0.0 \text{ \AA}$, the two nitrogen atoms have the same charge and the charge distribution pattern as a whole resembles a quadrupole

distribution.

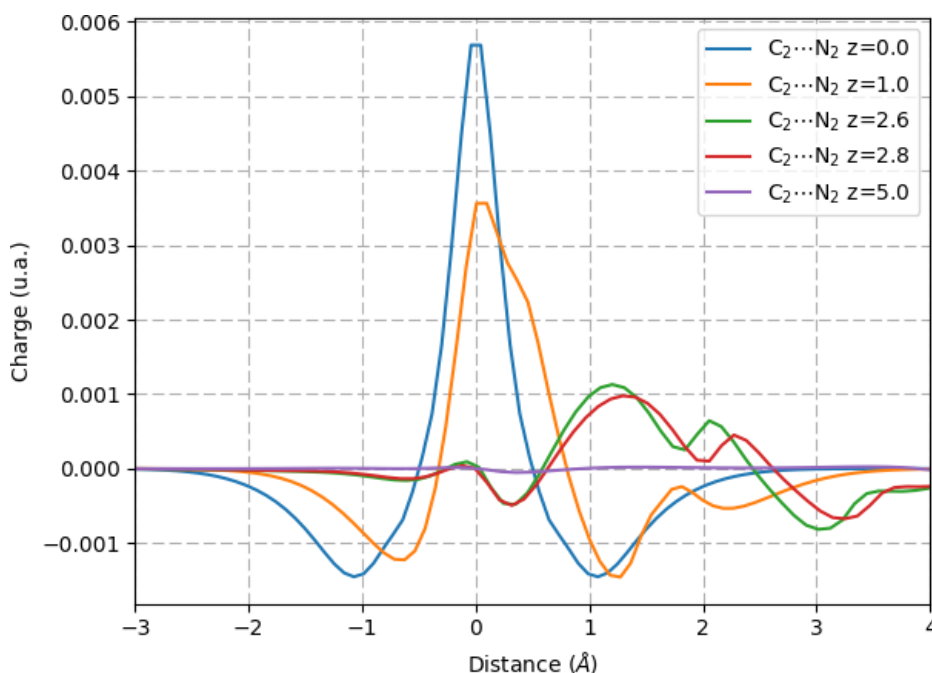


FIGURE 4.24 – Charge distribution on the z -axis as a function of the separation between monomers for the $C_2 \cdots N_2$ system. The ω B97X-D density was used in order to calculate these charge distributions.

Finally, despite the theoretical challenges in correctly describing this charge-transfer issue, a possible technological application of this specific pore-gas system might be suggested due to the mix between the pore and N_2 orbitals when forming the LUMO of the system. Figure 4.25 illustrates the variation of the ω B97X-D/jun-cc-pVDZ HOMO-LUMO gap for different systems involving the C_2 pore structure and several gas molecules. The HOMO-LUMO gap varies significantly only for the $C_2 \cdots N_2$ system. Such feature, if confirmed by experiment, could lead to a device used to optically detect the present of nitrogen gas. Whenever a nitrogen molecule approach the pore, optical absorption and emission characteristics would change appreciably and some sort of gas sensor could be devised.

4.2.6 $C_2 \cdots CO_2$

The last probing gas molecule that will be analyzed is the CO_2 gas. Despite not being a diatomic molecule, it is still an apolar molecule with linear structure, thereby avoiding complications with respect to multiple minimum configurations for diffusion. An important remark is that, for this system, the distance between z refers to the height of carbon atom to the plane of the unrelaxed pore structure. Figure 4.26 illustrates the results obtained with several different computational methods. There is a good agreement between all methodologies tested and charge transfer effects are apparently negligible. A

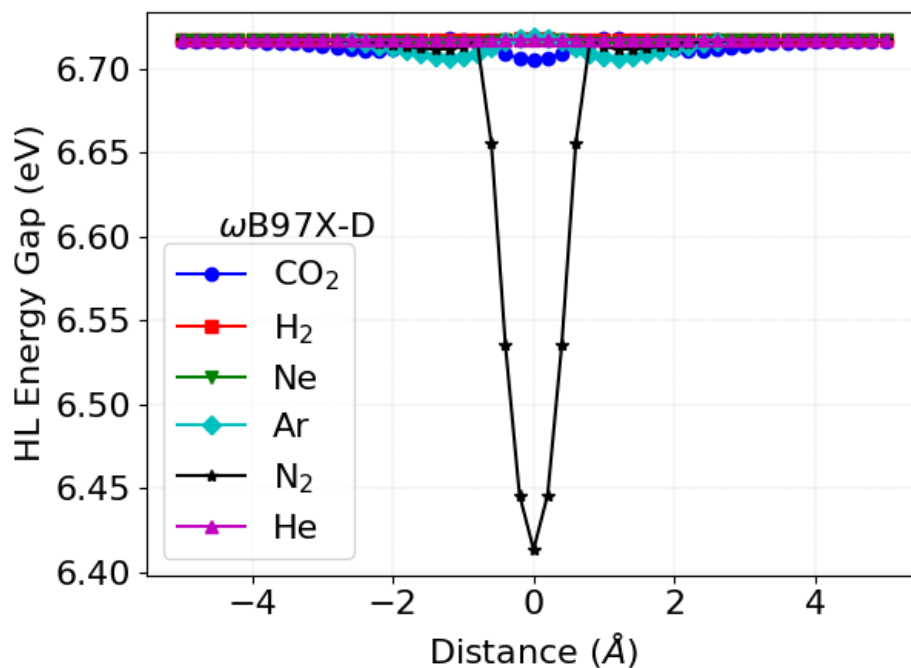


FIGURE 4.25 – HOMO-LUMO gap (in eV) as a function of the separation between the two monomers for the C_2 structure interacting with different gas molecules.

closer look at the minimum well region, as pictured in Figure 4.27, reveals the importance of the addition of dispersion terms for the stabilization of the dimer. PBE0/jun-cc-pVDZ results in a lower minimum well depth (about $3.0 \text{ kcal mol}^{-1}$) compared to other DFTs or SAPT0, which is reasonable since this hybrid functional does not account for the attractive dispersion component of the intermolecular interaction. On the other hand, the PBE0 function overestimated the diffusion energy barrier by approximately the same amount in comparison to the other results.

Figure 4.28 represents the energy decomposition of the total interaction energy of the $C_2 \cdots CO_2$ system. It has to be pointed out that both exchange and electrostatics terms (red and blue curves, respectively) present a significant hump at approximately 1.2 \AA , which coincide with the typical C-O bond distance in CO_2 . Such behavior could be explained by the high electronegativity of the oxygen atom, drawing electron density to itself. The diffusion of CO_2 gas through the pores will be hindered when the oxygen atoms are on the same plane of the pore structure, hence a larger exchange component. Likewise, the same behavior is expected for the electrostatic effects: the higher the electron density, the more relevant the coulombic interaction will be. For this systems, it seems that both electrostatic and dispersion effects play a major role on the nature of the minimum well region, since both energy components present a rather slow damping and can not be neglected after 2.0 \AA .

Table 4.6 presents the summarized results for the interaction between the C_2 pore

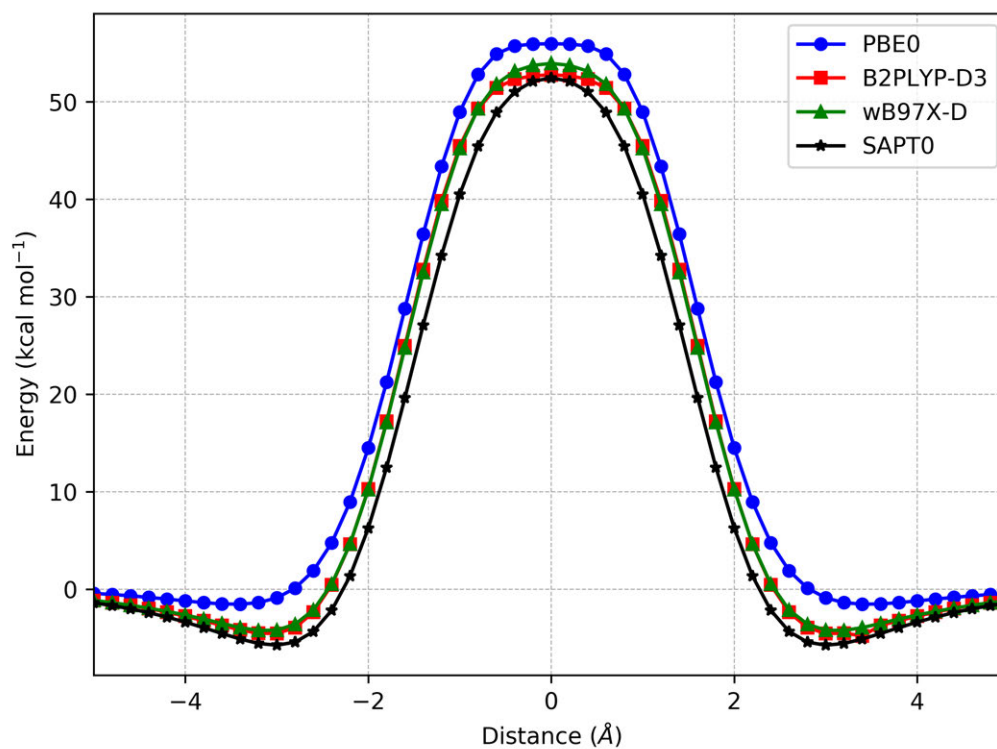


FIGURE 4.26 – $C_2 \cdots CO_2$ Potential Energy Surface calculated with different methodologies.

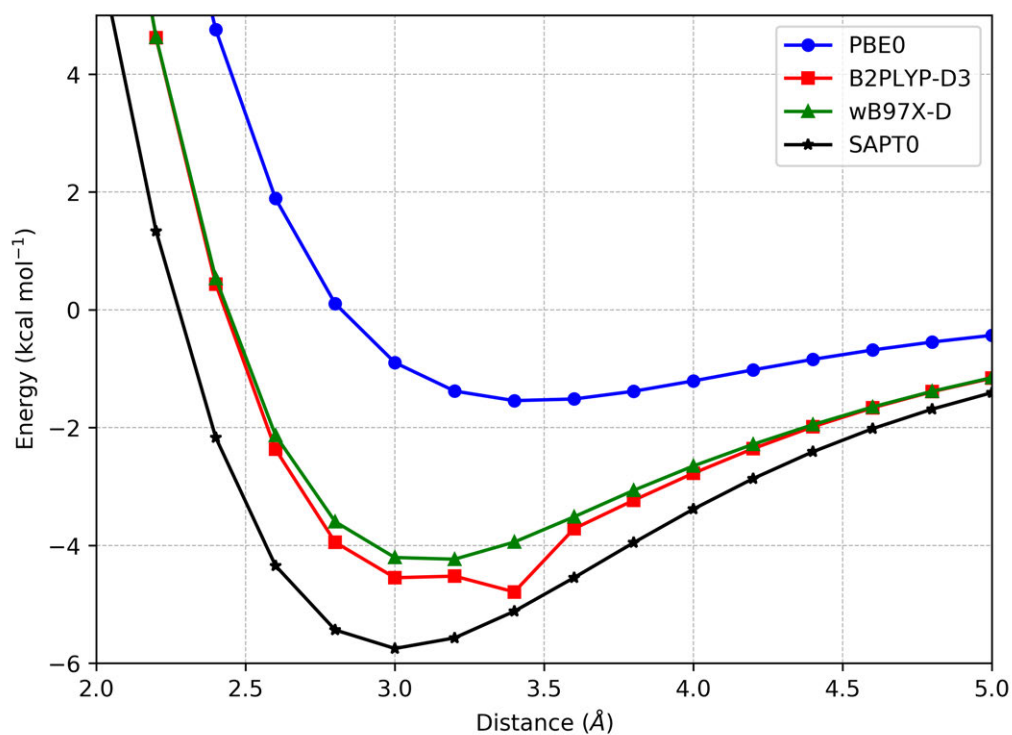
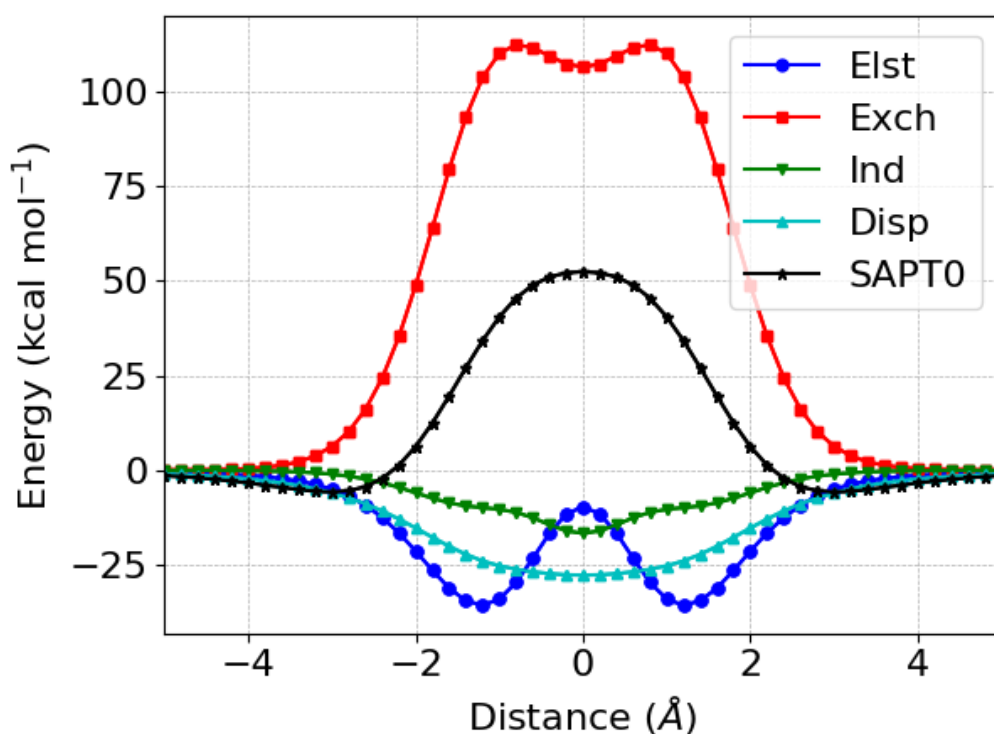


FIGURE 4.27 – $C_2 \cdots CO_2$ minimum well around the 3.0 \AA region of the PES.

structure and CO_2 , obtained at different levels of theory. Here, we show the diffusion energy barrier, the position of the minimum well on the potential energy surface as well

FIGURE 4.28 – $C_2 \cdots CO_2$ SAPT0 and energy components PES.

as the depth of such minimum. All methods tested resulted in a minimum well around the region between 3.0 Å and 3.4 Å. The diffusion energy barrier maximum deviation was around 4 kcal mol⁻¹, corresponding to a deviation of 8% with respect to the SAPT0 value. In this case, we also see a maximum deviation of 1.0 kcal mol⁻¹ for the well depth value with respect to SAPT0, if we do not consider the PBE0 result.

TABLE 4.6 – Summary for the interaction energy between C_2 and CO_2 : diffusion energy barrier (ΔE_{diff}), minimum well position (r_{vdW}) and minimum well depth (ΔE_{vdW})

| Method | ΔE_{diff} (kcal mol ⁻¹) | r_{vdW} (Å) | ΔE_{vdW} (kcal mol ⁻¹) |
|-----------------|---|---------------|--|
| PBE0 | 56.0 | 3.4 | -1.54 |
| B2PLYP-D3 | 52.8 | 3.4 | -4.79 |
| ω B97X-D | 53.9 | 3.2 | -4.23 |
| SAPT0 | 52.4 | 3.0 | -5.75 |

5 Chemical Doping

5.1 Motivation

Another strategy that could be used in order to modulate several properties of a given material is chemical doping or substitutional defects. For instance, replacing carbon atoms by boron or nitrogen allows modulation of the position of the frontier energy levels by the introduction of holes or electrons into the system, which would also reflect on properties as the energy gap, charge distribution and polarizability (TANG *et al.*, 2013; WANG *et al.*, 2014). It is undeniably that this strategy could lead to a remarkable range of new features and, in our case, might improve the efficiency of nanoporous membranes. In this chapter, our aim is to analyze how substitutional defects could be used in order to induce different permselectivity properties for porous membranes using the kekulene (C_2) as the host molecule to apply chemical doping. Here we focus on the substitution of carbon atoms bonded to hydrogen that are placed at the inner and outer diameters of the pore structure. Three different categories are proposed with respect to the type of heteroatom are proposed. First, carbon atoms were substituted only by nitrogen centers. A second category includes structure based on the substitution by boron atoms. Finally, the third category represents the pores in which both nitrogen and boron were used as a replacement for carbon atoms. The simple fact that both boron and nitrogen have atomic radii different from that of carbon might have large effect on the pore size, resulting, consequently, in different diffusion energy barriers. However, the chemical environment is also being significantly altered, as indicated by the inclusion of local dipole moments on the pore structure. Although previous studies have already explored the chemical doping strategy (ZHU *et al.*, 2015a; WANG *et al.*, 2017; QU *et al.*, 2017), their approach does not account for the geometrical and chemical effects in a separate fashion. Hence, our objective is to quantify how these modifications on the electronic structure of system contribute to the overall interaction energy and its components. To avoid geometrical distortions caused by the introduction of dopants, we have kept fixed geometrical parameters of the pore. They are identical to those presented in Figure 4.1, *i.e.*, the distance between the inner hydrogen atoms remain 3.64 Å. Finally, this part of the study also does not account for structural relaxation as the gas molecule and the pore are brought together.

5.2 Nitrogen substituted structures

The structures obtained by replacing some carbon atoms from the internal and external edges of Kekulene (C_2) by nitrogen atoms are presented in Figure 5.1. In this particular setting, nitrogen, having an extra π electron and being more electronegative than carbon, would be able to pull to itself more electron density. Moreover, its van der Waals radius is also smaller than carbon's. Hence it is expected that, in principle, these systems would show a lower energy barrier towards H_2 diffusion compared to the C_2 structure, especially if these nitrogen centers were to occupy the inner edge of the kekulene structure. Figure 5.1 illustrates the results for the total interaction energy between these N-doped pores and the H_2 gas molecule. It is possible to notice two distinct groups. The first group is characterized by a higher diffusion energy barrier and corresponds to the pristine C_2 pore and the doped structures in which some N atoms are introduced only at the external periphery of the C_2 pore (C_2-N_{ext}). The second group of pore molecules, which have an energy barrier of about 3 kcal mol^{-1} , corresponds to those obtained by doping the C_2 pore at the inner edge (C_2-N_{int}) and also by the doubly substituted system (C_2-NN). In this case, the prediction matches the computed results: the difference between the energy barriers between the two groups is at least $8.0 \text{ kcal mol}^{-1}$, with the doped structures where N atoms occupy the inner edge having the lower energy barriers. This large difference might reflect the influence of N atoms to the effective pore size based on the electron density and also to the chemical affinity of the pore structure. Moreover, one can notice that the introduction of N atoms at the external edge of the pore has a secondary role with respect to the molecular interactions and this effect becomes more visible for the second group of doped structures, since in this case the difference in the diffusion barrier between C_2-N_{int} and C_2-NN is about $2.0 \text{ kcal mol}^{-1}$.

An analysis of the energy components that contribute towards the total interaction energy is presented in Figure 5.3. We see that, while the exchange component, which we have already shown to be closely related to the physical size of the pore (Figure 5.3a) largely contributes to the repulsive character of the energy barrier, the electrostatics, induction and dispersion components act in order to counterbalance such influence. Again, we see that the major contributing factor for the $8.0 \text{ kcal mol}^{-1}$ energy difference aforementioned comes from the exchange-repulsion term. The C_2 and C_2-N_{ext} presents an exchange term almost $8.5 \text{ kcal mol}^{-1}$ higher than their C_2-N_{int} and C_2-NN counterparts. This also reflects our prediction that nitrogen is more capable of pulling electron density to itself, resulting in a less crowded pore center. Despite this significant difference in the exchange component, Figure 5.3b shows that there is almost no difference between the electrostatic energy component for the four N-substituted system. Induction (Figure 5.3c) and dispersion (Figure 5.3d) components reveal an interesting pattern. As discussed previously, both components are related to the the ability of each pore system to polarize

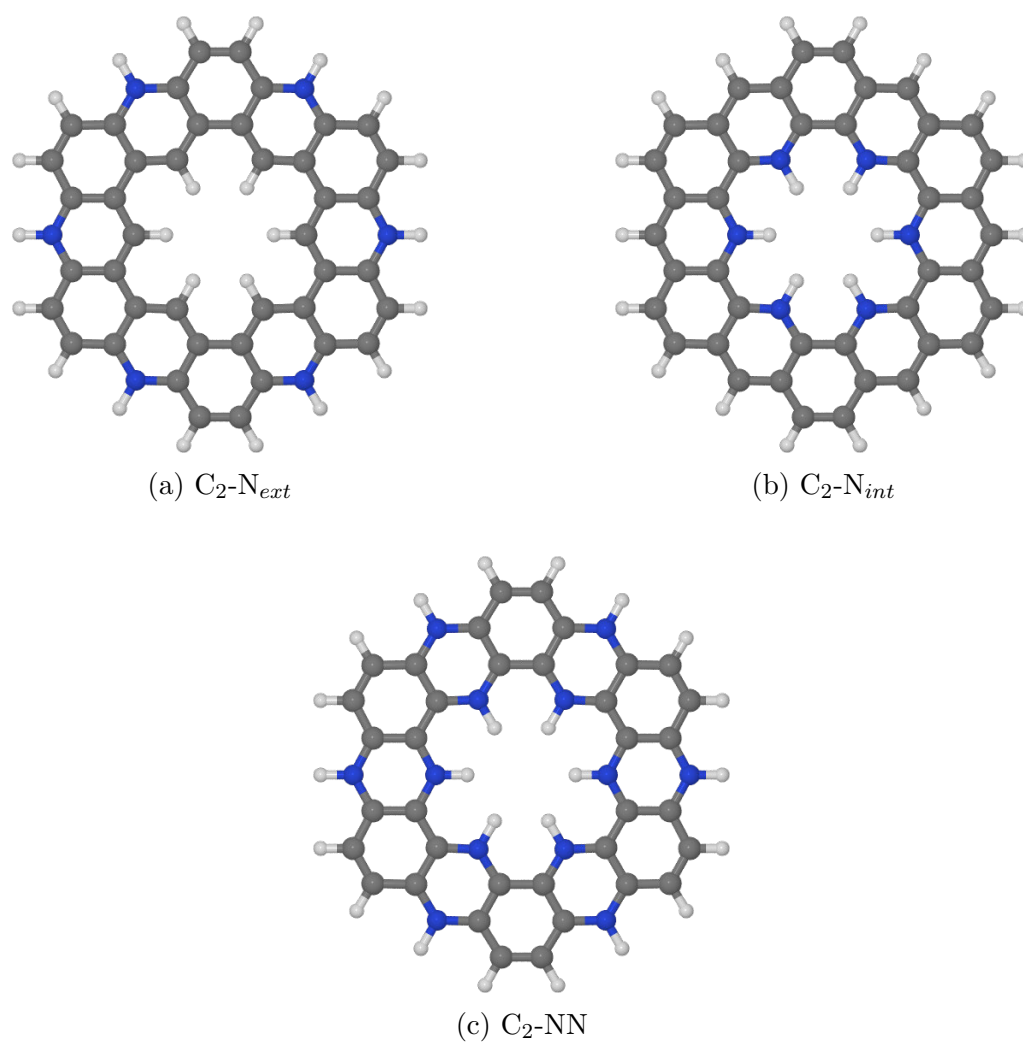


FIGURE 5.1 – Structures for the N-substituted pores based on the kekulene (C_2 backbone): (a) Substitution on the external edge (C_2-N_{ext}); (b) Substitution on the internal edge (C_2-N_{int}); (c) Substitution on both edges (C_2-NN).

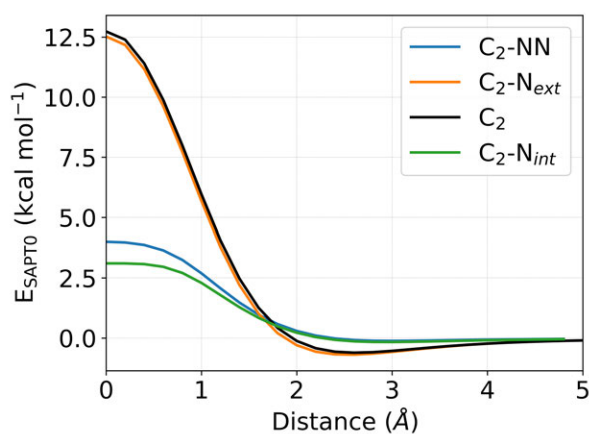


FIGURE 5.2 – Total interaction energy between H_2 and the N-substituted pores

under the influence of the electric field generated by the hydrogen molecule. In this case, the behavior of the induction component is the opposite of the one shown by the dispersion component. While the systems that contain nitrogen in the inner diameter of the pore present an induction component around $1.5 \text{ kcal mol}^{-1}$ lower in energy than the systems that only have carbon atoms in their innermost edge, the dispersion component for the later group (C_2 and C_2-N_{ext}) is $2.0 \text{ kcal mol}^{-1}$ lower than for the former (C_2-N_{int} and C_2-NN).

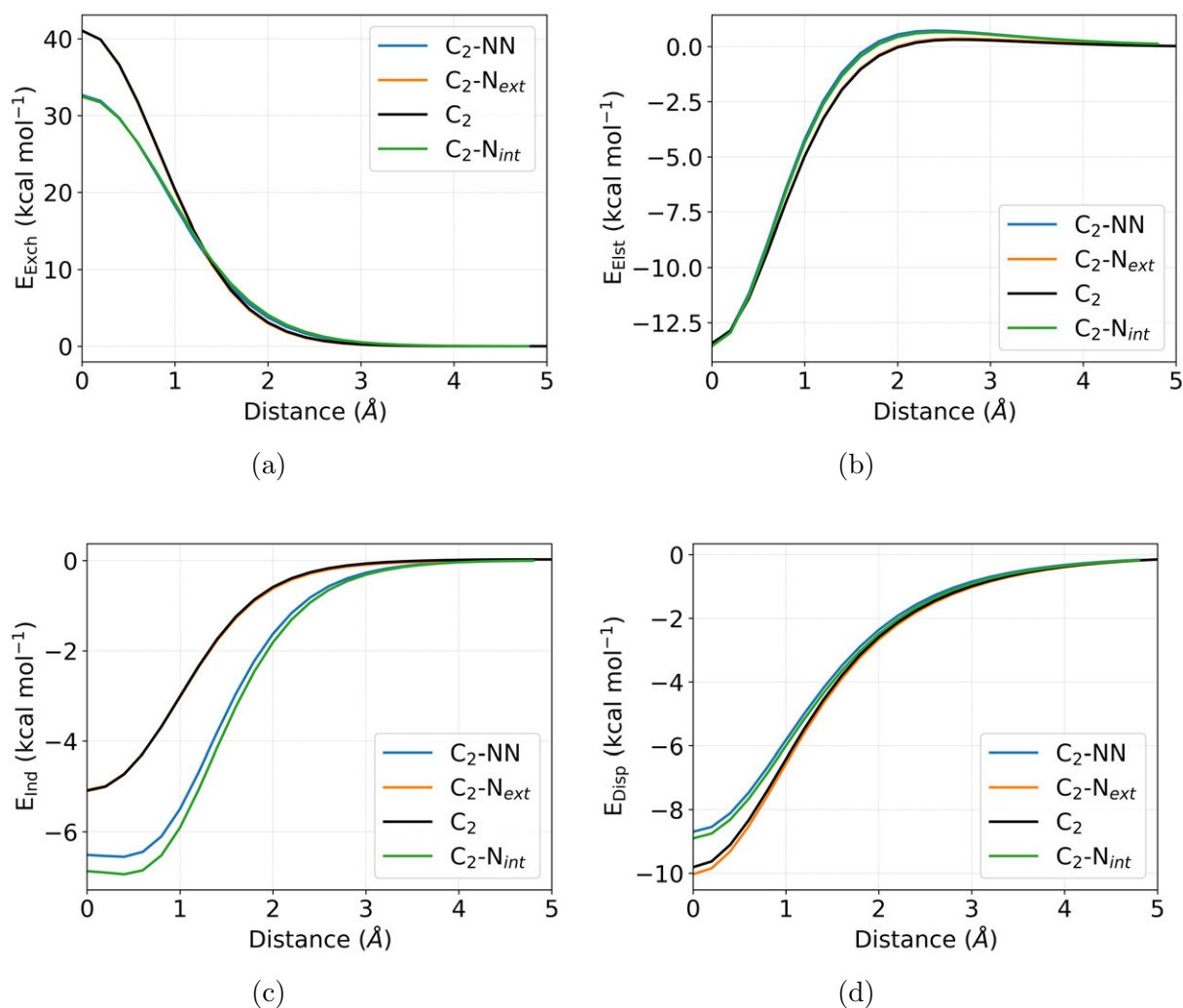


FIGURE 5.3 – Components of the total interaction energy for the B-substituted systems: (a) Component of the interaction energy due to intermolecular exchange; (b) Component of the interaction energy due to electrostatics; (c) Component of the interaction energy due to induction; (d) Component of the interaction energy due to dispersion.

We have also performed the NCI index and the density difference analysis described in chapter 3 for the C_2 and C_2-NN systems. Figure 5.4 shows the NCI plots of the reduced density gradient versus the signed density as well as the NCI isosurfaces for distances of 0 \AA , 2.6 \AA and 5.0 \AA between the C_2 structure and the H_2 gas. It is worth noticing that, in comparison to the C_2 -square and C_2 -pent topologies, even when the pore and the

gas molecule are far apart, these plots reveal the influence not only of the intramolecular interactions involving the hexagon units of C_2 , but also from the interaction of the internal hydrogen atoms, which is originated both from dispersive and repulsive effects. Moreover, as the two systems are brought together, the attractive component, which is indicated by the blue-green peak around $x = -0.02$ u.a., also plays an increasing role in order to describe the interaction between the two systems. This behavior is shown in both graphs: there is the appearance of a small blue peak in Figure 5.4e and the darker green color of the isosurface between the two hydrogen, as illustrated in Figure 5.4f. Finally, it is interesting to note that such feature is accompanied by two new regions of strong repulsion between the two system. In this sense, we see that the interaction is mostly a local phenomenon and different parts of the pore system, due to their distinct nature and chemical environment, will interact in a unique fashion with the H_2 molecule.

The previous analysis was also applied to the C_2 -NN system (Figure 5.5). In this case, according to the results reported above, one can see that the influence of the repulsive effects is less significant for the interaction. The other effects, on the other hand, could not be grasped so easily by the NCI analysis. A possible hypothesis is that the overall shape of the electronic density of the system might not be significantly influenced by the addition of 12 π electrons on a system that already has a total of 312 electrons. Figure 5.6 shows that it is difficult to measure the differences between the two pores systems using the overall density at 0.0 Å, even though the C_2 -NN is able to polarize more the H_2 molecule when the two systems are separated by 5.0 Å (Figure 5.7), due to a higher electrostatic potential generated by its overall charge. Although it is not describe in the literature, a possible extension of the NCI index only to the π electrons of the system might be useful in order to evaluate the main differences on the behavior of the interaction between the gas molecule and the pore systems.

5.3 Boron substituted structures

Similarly, it is possible to replace some carbon atoms from the internal and external edges of Kekulene (C_2) by boron atoms (Figure 5.8). These structures, following the same name scheme used previously, will be denoted by C_2 - B_{ext} , C_2 - B_{int} and C_2 -BB. Similarly to the N-doped case, one can identify in Figure 5.9 the existence of two clear groups, which can be differentiated by the the position of the heteroatom (boron in this case). However, in this case, the behavior is opposite to that observed for the N-doped system. The group presenting the higher diffusion energy barrier is characterized by the substitution of carbon atoms by boron at the inner edge. The doped pores having boron atoms in their external diameter present a total interaction energy around 10.0 kcal mol⁻¹ lower than the first group. Interestingly, the energy difference the energy difference between C_2 -NN

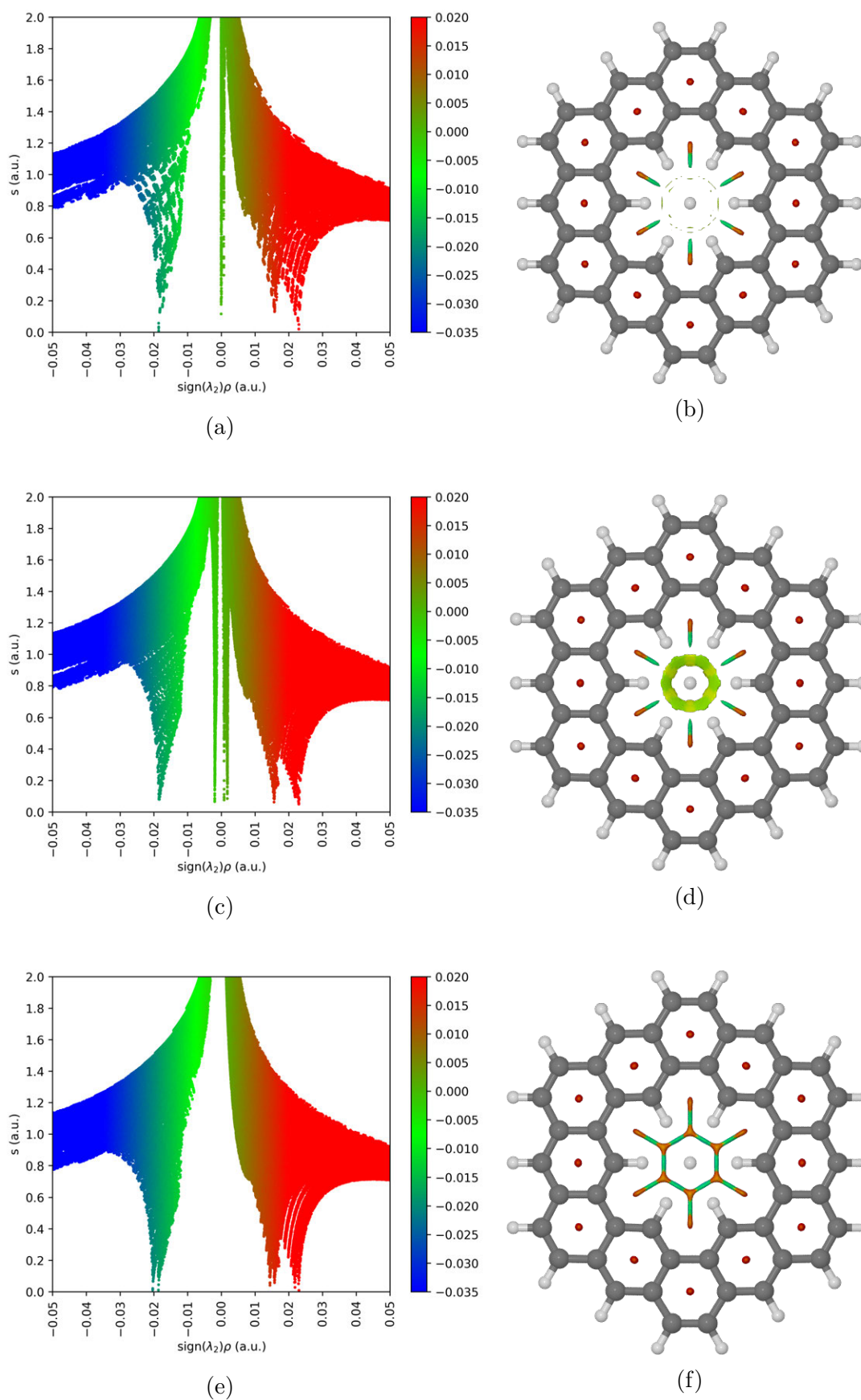


FIGURE 5.4 – NCI analysis for the C_2 pore structure at different separation distances between the monomers: (a) NCI plot for a distance of 5.0\AA ; (b) NCI isosurface for a distance of 5.0\AA ; (c) NCI plot for a distance of 2.6\AA ; (d) NCI isosurface for a distance of 2.6\AA ; (e) NCI plot for a distance of 0.0\AA ; (f) NCI isosurface for a distance of 0.0\AA .

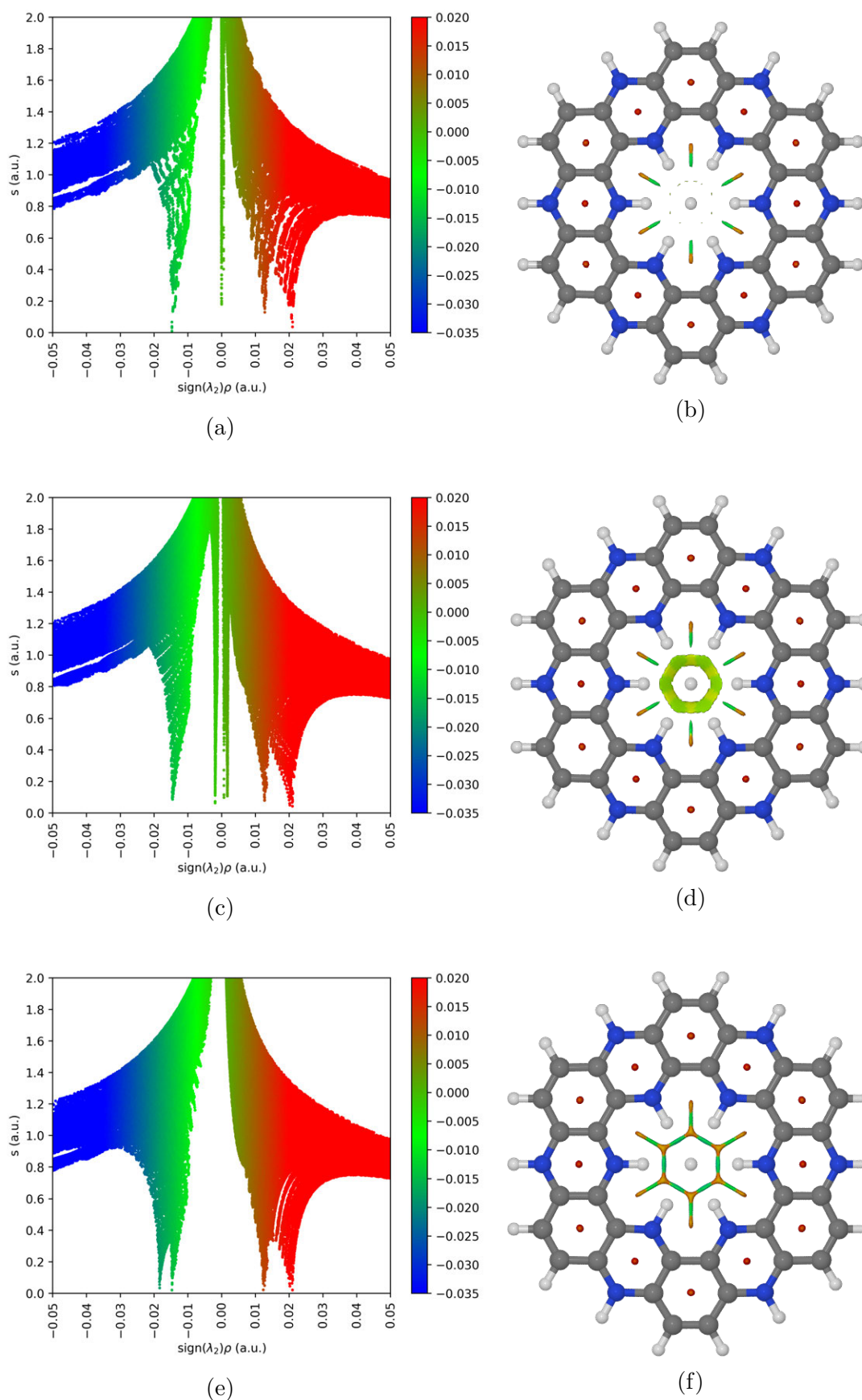


FIGURE 5.5 – NCI analysis for the C_2 -NN pore structure at different separation distances between the monomers: (a) NCI plot for a distance of 5.0\AA ; (b) NCI isosurface for a distance of 5.0\AA ; (c) NCI plot for a distance of 2.6\AA ; (d) NCI isosurface for a distance of 2.6\AA ; (e) NCI plot for a distance of 0.0\AA ; (f) NCI isosurface for a distance of 0.0\AA .

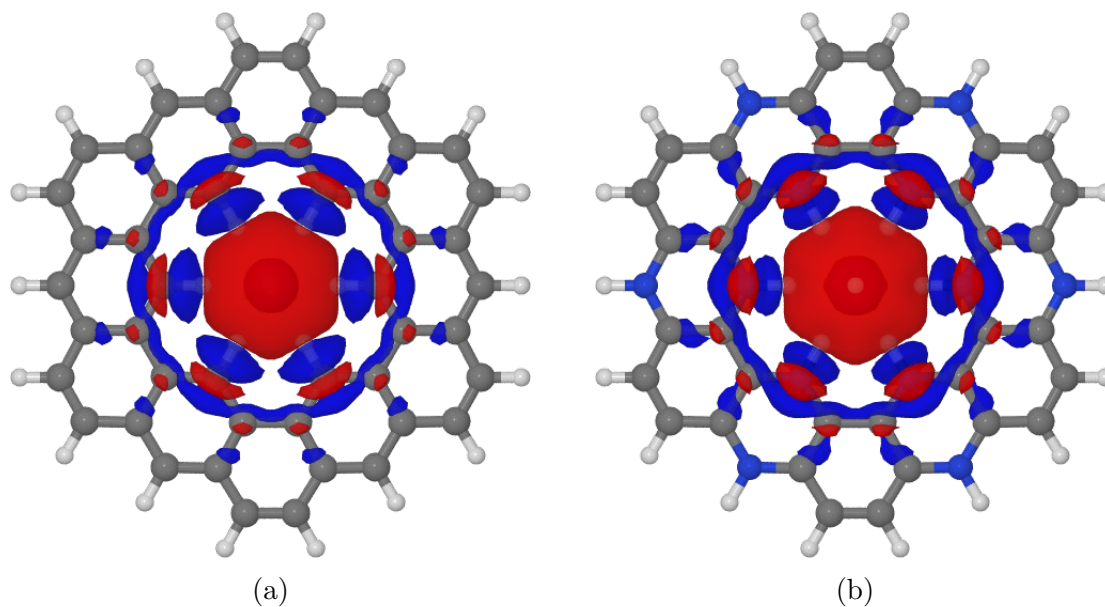


FIGURE 5.6 – Density difference isosurfaces for a separation distance of 0.0 \AA between the pore and the gas: (a) C_2 pore system; (b) C_2 -NN pore system.

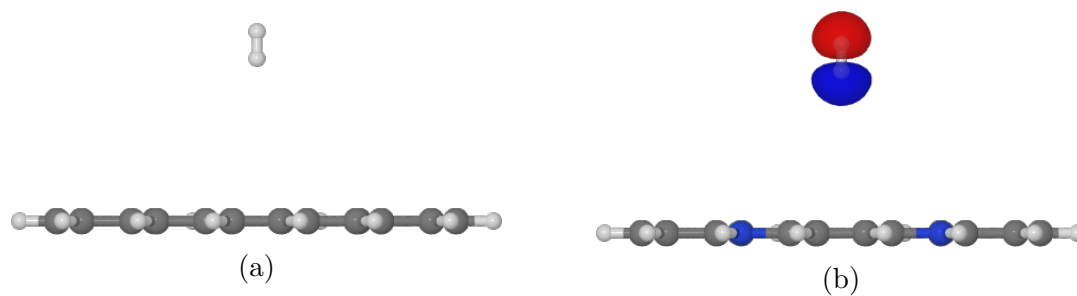


FIGURE 5.7 – Density difference isosurfaces for a separation distance of 5.0 \AA between the pore and the gas: (a) C_2 pore system; (b) C_2 -NN pore system.

and C_2 -BB is around $20.0 \text{ kcal mol}^{-1}$, which indicates how useful doping schemes could be in order to enhance permselectivity properties of nanoporous membranes.

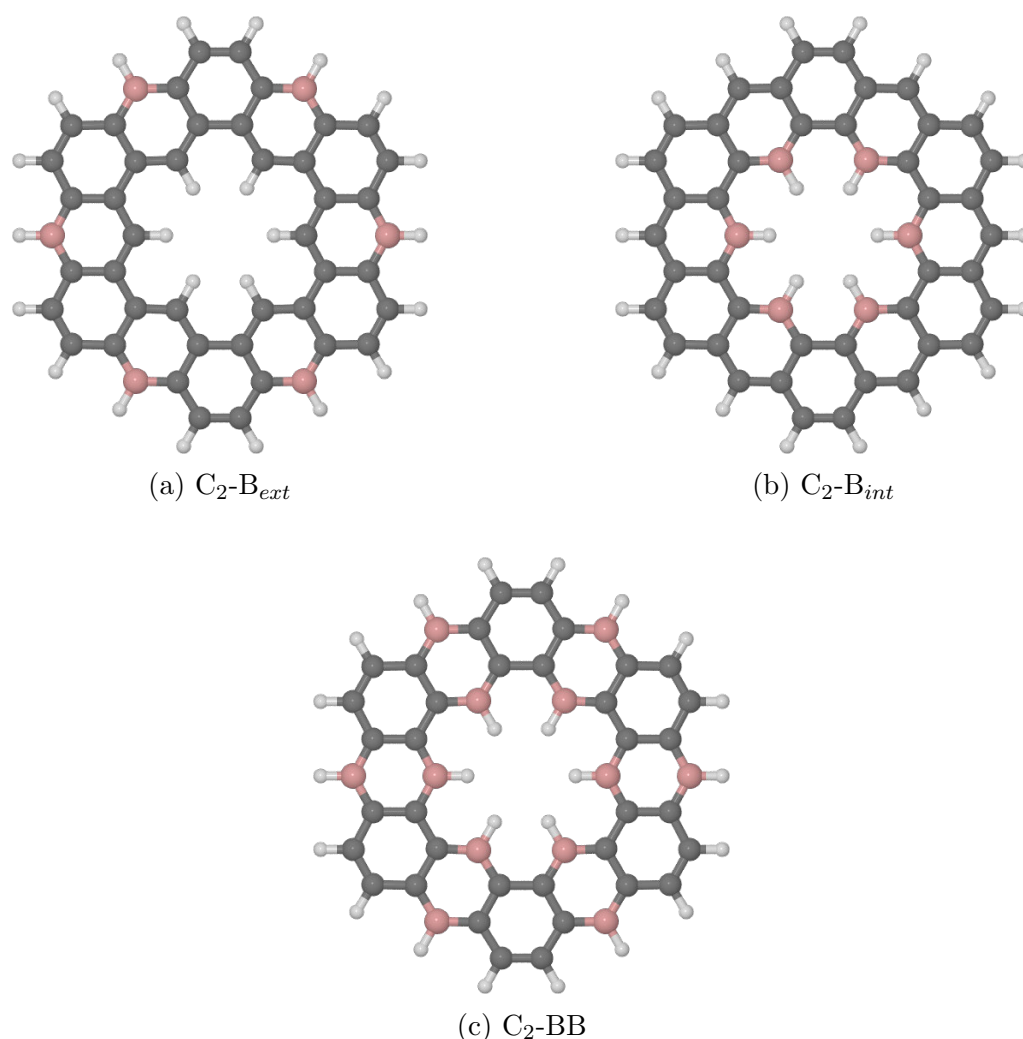


FIGURE 5.8 – Structures for the B-substituted pores based on the kekulene (C_2 backbone): (a) Substitution on the external edge (C_2 - B_{ext}); (b) Substitution on the internal edge (C_2 - B_{int}); (c) Substitution on both edges (C_2 -BB).

For these B-doped structures, we were able to obtain the energy components for the interaction between each pore and the H_2 molecule (Figure 5.10). An interesting fact is that the difference in the total interaction energy between the two groups corresponds almost exclusively to the difference in the exchange component (Figure 5.10a). The induction component (Figure 5.10c) also contributes to a difference of $1.0 \text{ kcal mol}^{-1}$, whereas the other terms (electrostatics and dispersion) would not be enough to differentiate between the group characterized by boron atoms in the inner edge (C_2 -BB and C_2 - B_{int}) from the other that contains the (C_2 and C_2 - B_{ext}). Here, it is clear the weight of the exchange-repulsive to describe the diffusion process. Similarly to what was discussed for the $C_2 \cdots Ar$ system on chapter 4, one can see that, due to a larger value of exchange, which was also expected by the fact that boron has a larger van der Waals radius compared

to carbon, the attractive components only play a secondary role, despite their importance towards the stabilization of the dimer.

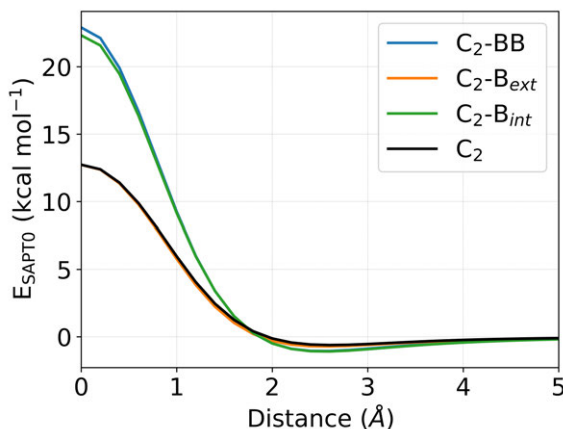


FIGURE 5.9 – Total interaction energy between H_2 and the B-substituted pores

5.4 Mixed BN substituted structures

Finally, we present the structures obtained by mixing both doping schemes, *i.e.*, replacing some carbon atoms from the internal and external edges of Kekulene (C_2) by boron and nitrogen atoms (Figure 5.11). In this case, we did not perform a thorough analysis, given that it would depend on several factors, such as the charge separation between both edges, the strength of the dipole moment introduced by the BN pair and the balance between electron donor and acceptor regions of the molecule. Figure 5.12 shows the results for the total interaction energy between these five porous systems and the H_2 molecule. Due to the mixed effects of the B and N substitution strategies, we now see four distinct groups. The curve lower in energy represent the system in which boron and nitrogen dopants are introduced at the outer and innermost pore edges, respectively (Figure 5.11a). It is worth noticing that, in comparison to the C_2-N_{int} and C_2-NN systems, the introduction of the B centers in the structure leads to a marginally higher diffusion energy barrier. Furthermore, the chemical modification of C_2 with B atoms in the inner edge contributes to a higher barrier as well. In this case, even the alternation scheme between B and N dopants (Figures 5.11d and 5.11e) is not enough to bring the diffusion energy barrier back to a value similar to the one presented by the non substituted structure (C_2).

The difficult posed by the complete analysis of all the effects that contribute towards the total interaction energy is shown in Figure 5.13. Apparently, no clear trend for the ordering of the energy barriers between the groups previously mentioned, even though the the C_2-BN (Figure 5.11a) and C_2-NB structures (Figure 5.11b) represents the two

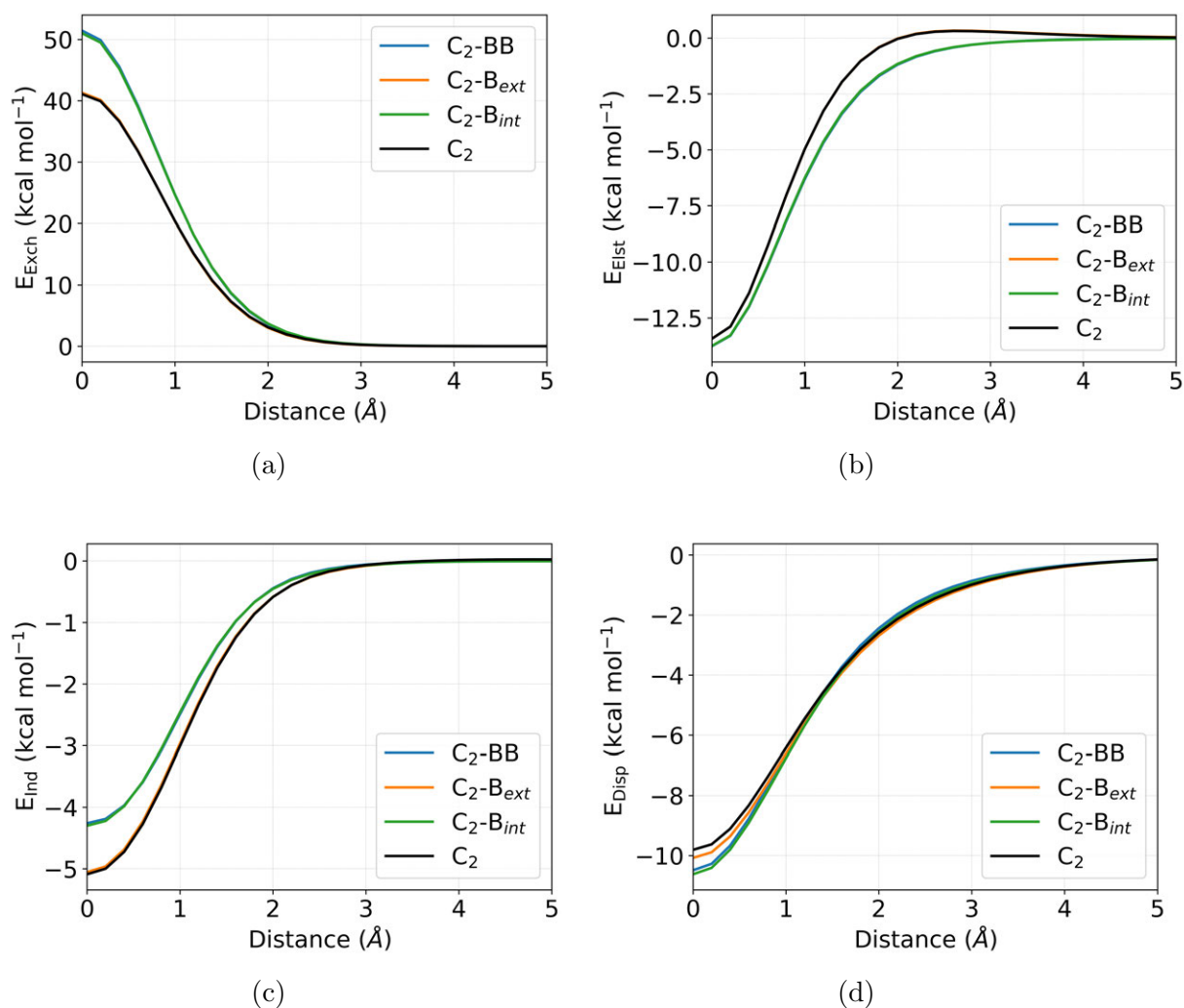


FIGURE 5.10 – Components of the total interaction energy for the B-substituted systems: (a) Component of the interaction energy due to intermolecular exchange; (b) Component of the interaction energy due to electrostatics; (c) Component of the interaction energy due to induction; (d) Component of the interaction energy due to dispersion.

limiting cases that follows the expected behavior with respect to the effective pore size, *i.e.*, the amount of electron density penetration into the pore region. This is also reflected by the similarity between the curves representing the total interaction energy for the C₂ (black) and C₂-NB_{alt}^{ext} (green) in Figures 5.12 and 5.13. Even though we used the double substitution scheme in C₂-NB_{alt}^{ext}, its internal edge remains composed only by carbon atoms and, in this sense, the chemical environment felt by the H₂ molecule is similar to that created by the C₂ pore.

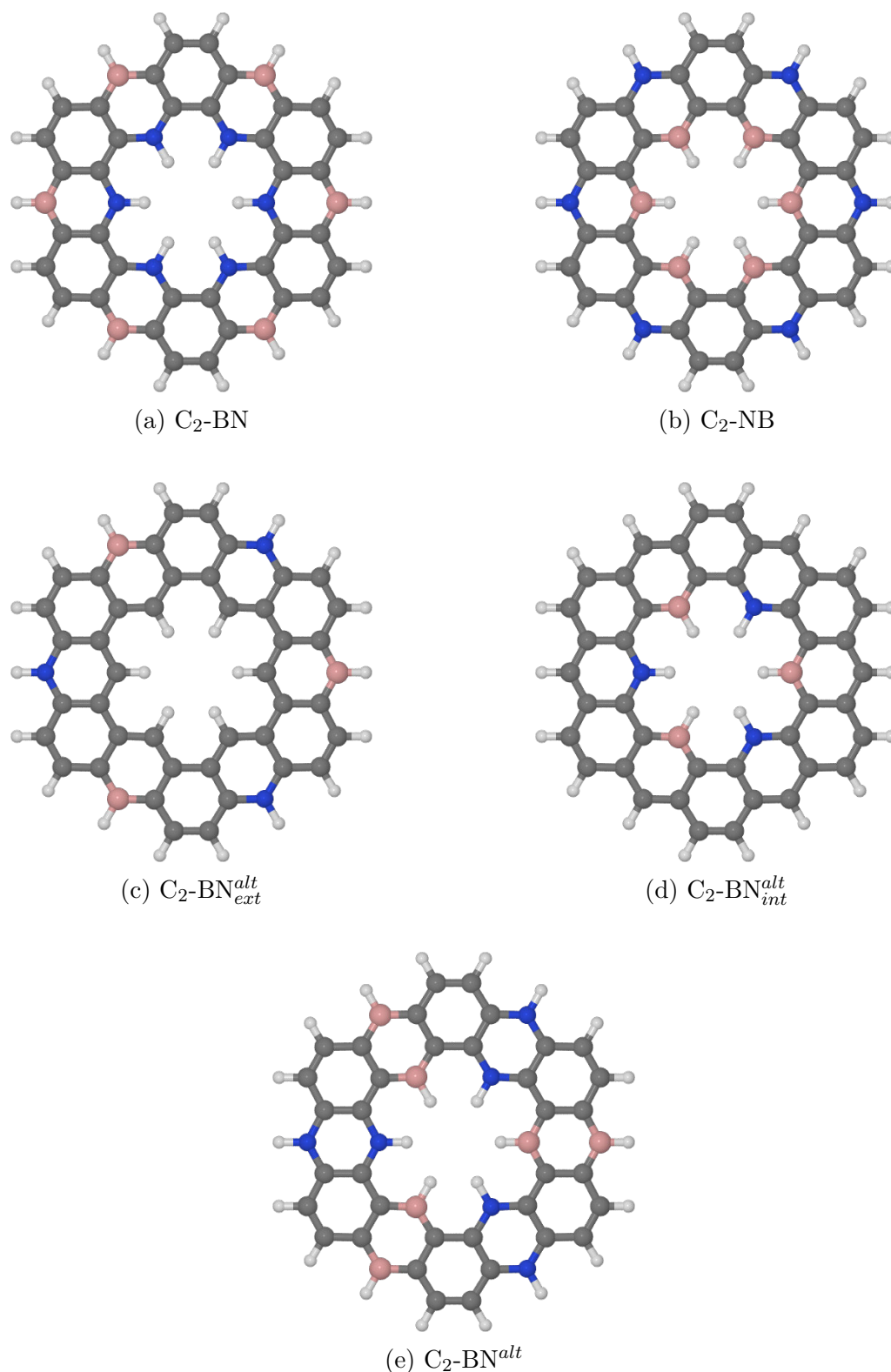


FIGURE 5.11 – Structures for the BN-substituted pores based on the kekulene (C_2 backbone): (a) B-substitution on the external edge and N-substitution on the internal edge (C_2 -BN); (b) N-substitution on the external edge and B-substitution on the internal edge (C_2 -NB); (c) Alternated BN-substitution on external edge (C_2 -BN_{ext}^{alt}); (d) Alternated BN-substitution on internal edge (C_2 -BN_{int}^{alt}); (e) Alternated BN-substitution on both edges (C_2 -BN^{alt}).

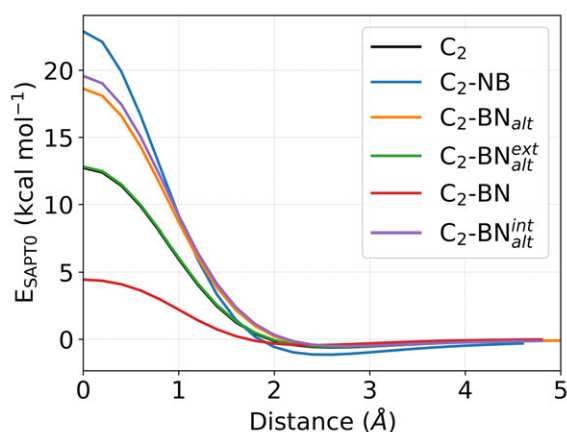
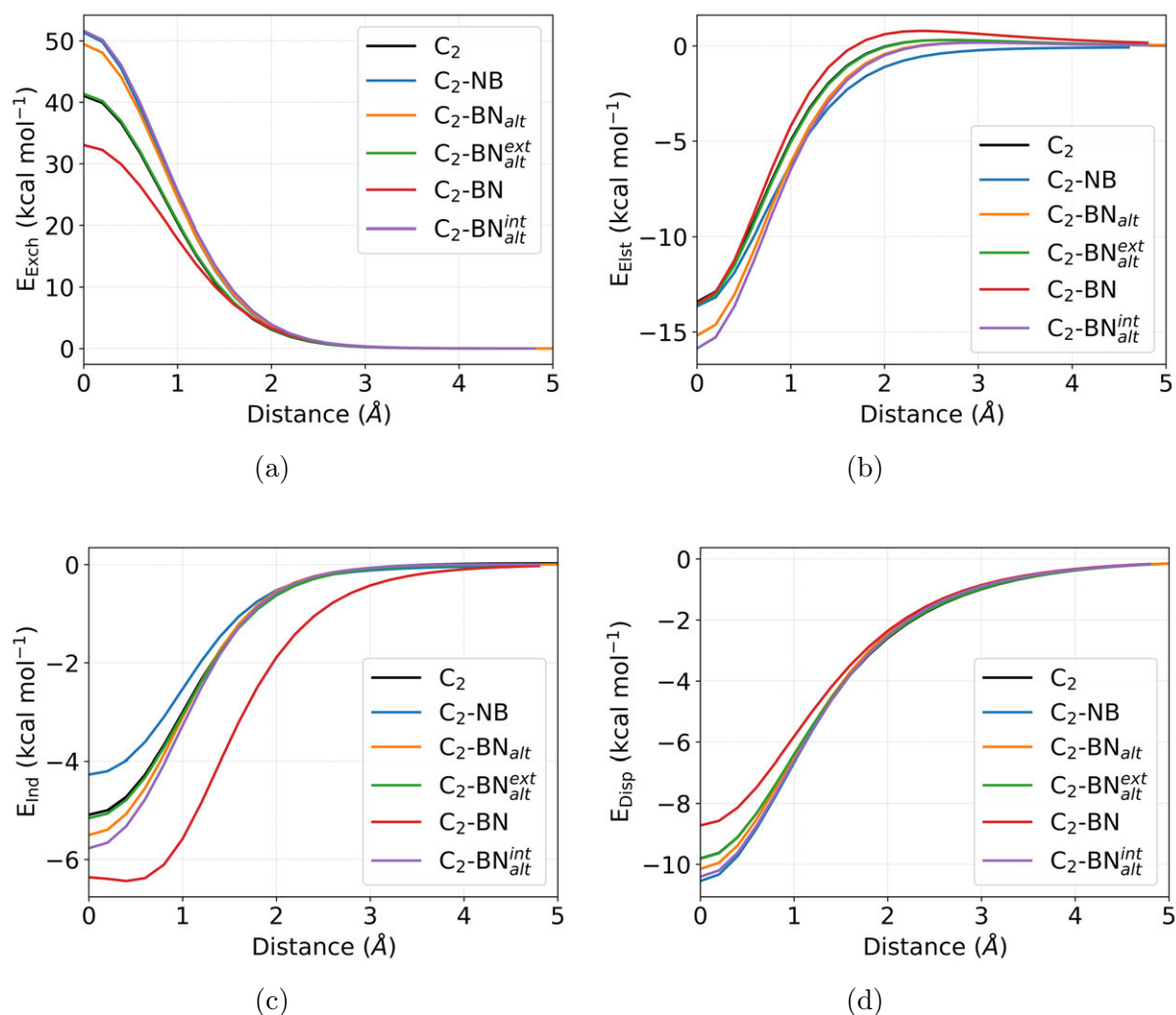
FIGURE 5.12 – Total interaction energy between H_2 and the BN-substituted pores

FIGURE 5.13 – Components of the total interaction energy for the BN-substituted systems: (a) Component of the interaction energy due to intermolecular exchange; (b) Component of the interaction energy due to electrostatics; (c) Component of the interaction energy due to induction; (d) Component of the interaction energy due to dispersion.

6 Conclusions

In the present work, we have proposed a thorough analysis of the main factor that contribute towards the diffusion energy barrier of a gas molecule through a porous membrane. The reported literature on this subject, despite being abundant, does not describe how one could systematically modify the pore structure in order to enhance selectivity and permeability properties for a target gas molecule. Moreover, and of crucial importance, is that most of previous works based their search for “optimal” structures mainly based on the geometrical ideal that a larger pore would lead to a smaller diffusion barrier. Even though most authors acknowledge the problem associated to the measurement of the size of the pore, which is inherent to the quantum mechanical description of our problem, a deep discussion regarding how such feature affects the diffusion mechanism through a pore is still missing. In this sense, our study focus on two possible strategies on how one could change the diffusion energy barrier, while keeping a controllable geometrical pore size; first, we analyze the effects of topological changes in the diffusion energy barrier. Then, we investigate, within a given topology, effects such as the choice of methodology to compute the energy barrier and the target gas molecule. Finally, sticking with a single topology, we analyze, without accounting for structural relaxation, the effects of chemical doping from the substitution of carbon atoms on the inner and outer pore diameters by hetero atoms such as nitrogen and boron.

The first part of the study aimed to shed light into the mostly accepted idea that pore size is the only factor that should be taken into account in order to design efficient porous membranes towards applications related to the separation of the components of a given mixture. Quantum-chemical computations on a size-reduced molecular model of two graphene-based membranes (C_2 -square and C_2 -pent) revealed that, in this case, the smaller pore (C_2 -pent) presented a energy barrier towards diffusion of H_2 1.0 kcal mol⁻¹ lower than its analogue (C_2 -square). Despite this apparently modest difference, estimates of selectivity and permeance indicate a 5-fold improved performance for the fused pentagon membrane. We were able to show that this initially unexpected behavior suggests a mechanism of compensation between the non-covalent interactions that account for the total interaction energy. Despite playing a role of paramount importance and being the most significant component that accounts for the diffusion energy barrier between a

pore system and a gas molecule, exchange-repulsion, which is deeply connected to the idea of pore size, might not be enough to account for all effects involved in the diffusion process. In this sense, this work suggests that special attention should be given to the analysis of electron delocalization and charge distribution, factors that counterbalance the repulsive influence due to pore size and provide a rationalization for the behavior of the remaining energy components (electrostatics, induction and dispersion). This full picture provides a conceptual basis to understand the complex set of intermolecular interactions involved in the sieving process which is essential to promote new guidelines for a intelligent design of efficient molecular sieves.

In the second part part of the present work, we studied the interaction of several gas molecules, such Argon (Ar), Neon (Ne), Helium (He), H₂, N₂, and CO₂ with a pore structure based on the Kekulene molecule (C₂), using different density functionals. In a first approximation, geometry relaxation effects arising from the mutual interaction between the gas species and the pore structure were not take into account, the obtained potential energy barriers can be considered as a superior limit for the energetics of the gas permeance. A systematic comparison between different density functionals and the SAPT0 methodology has been performed, unveiling the role played by each meaningful component (electrostatic, exchange, induction and dispersion) of the total interaction energies to the formation of the difusion energy barrier. For this C₂ system, it has been pointed out that, due to steric hindrance caused by the hydrogen atoms that crowd the pore region, the exchange component of the total interaction energy is not only highly repulsive, but compromises the efficiency of such pore structure in industrial applications focused on gas separation. Nevertheless, it seems to be suitable for He and H₂ separation, based on the fact that these gas molecules present a diffusion energy barrier lower than 15.0 kcal mol⁻¹ (Table 6.1). Moreover, it has to be pointed out some evidences for significant charge transfer between the two monomers involved in the C₂⋯N₂ system at shorter distances. This could be explained by a non-negligible mix between the virtual orbitals of each monomer and should be object of a further investigation regarding the behavior of the induction component.

TABLE 6.1 – Summary for the SAPT0/jDZ interaction energy between C₂ and different gas molecules: diffusion energy barrier (ΔE_{diff}), minimum well position (r_{vdW}) and minimum well depth (ΔE_{vdW})

| Method | ΔE_{diff} (kcal mol ⁻¹) | r_{vdW} (Å) | ΔE_{vdW} (kcal mol ⁻¹) |
|-----------------|---|---------------|--|
| Ar | 84.7 | 2.6 | -1.83 |
| Ne | 25.0 | 2.8 | -0.30 |
| He | 9.7 | 2.6 | -0.21 |
| H ₂ | 12.7 | 2.6 | -0.61 |
| N ₂ | 61.9 | 2.6 | -3.81 |
| CO ₂ | 52.4 | 3.0 | -5.75 |

The third part of the study focused on the influence of chemical doping, especially the substitution of carbon atoms on the inner and outer diameters of each pore system by boron and nitrogen centers, on the total interaction energy between the porous structure and the H_2 molecule. Without account for structural relaxation effects, we propose a total of 12 different pores, divided into three groups. The first group comprises the kekulene molecule (C_2) and its N-doped derivatives (C_2-N_{ext} , C_2-N_{int} and C_2-NN). For these systems, it is interesting to notice that the lowest diffusion energy barrier arises for the system containing nitrogen atoms at the inner edge, due to the fact that such centers are responsible to pull the electron density to themselves, leading to a less crowded pore area. Moreover, the introduction of nitrogen atoms at the outermost diameter does not seem to affect the diffusion energy barrier in a significant manner. The NCI analysis is also useful in order to help us visualize the structural differences between the C_2 system and its N-substituted counterparts. For instance, the NCI analysis shows us that steric/repulsive effects are less dominant for the C_2-NN pore in comparison with the kekulene pore. The second group contains the B-doped derivatives of kekulene. In this case, it is possible to observe the opposite behavior when compared to the N-substituted group. The inclusion of boron atoms in the inner edge of the pore leads to a higher diffusion energy barrier. Finally, the third group is formed by structures obtained by a mixed BN-doping scheme and, in this case, we see that it is difficult to isolate the individual effects of B and N, even though the influence of the boron in the inner edge seems to be more significant than that of nitrogen in the same position. More importantly, this part of the study showed us that it is possible to tailor and obtain a wide range of diffusion energy barriers while keeping the same topological structure and exploring the effects of doping schemes.

In summary, the present work shed light into a few puzzling questions involving the diffusion process through porous nanomembranes. Using a molecular model as a pore, we have shown that geometrical pore size might not be enough to describe the diffusion process, given that, at the nanoscale, polarization effects might play an important role to counterbalance the repulsive influence posed by pore size. We also analyzed how different levels of methodology could influence the energy results for several gas molecules. An investigation of the effects of doping schemes in order to modify the diffusion energy barrier was also carried out. Despite our attempt to unveil several aspects leading to a rational design of porous membranes, a few other questions remain unanswered. The first and most obvious concerns the extension of our findings to periodical systems, in which we would also have to take into account factors such as the distance between pore replicas. Moreover, our analysis is based on a static picture for a dynamical process. In this sense, molecular dynamics and a statistical analysis could be used in order to assess the most significant conformations for the complex systems and then apply a more rigorous methodology to study such “frames”.

Bibliography

AMBROSETTI, A.; SILVESTRELLI, P. L. Gas separation in nanoporous graphene from first principle calculations. **Journal of Physical Chemistry C**, v. 118, n. 33, p. 19172–19179, 2014. ISSN 19327455.

BADER, R. F. W. A quantum theory of molecular structure and its applications. **Chemical Reviews**, v. 91, n. 5, p. 893–928, 1991.

BECKE, A. D. Density-Functional Exchange-Energy Approximation with Correct Asymptotic Behavior. **Physical Review A**, v. 38, p. 3098–3100, set. 1988.

BLANKENBURG, S. *et al.* Porous Graphene as an Atmospheric Nanofilter. **Small**, WILEY VCH Verlag, v. 6, n. 20, p. 2266–2271, oct 2010. ISSN 16136810.

BLUM, V. *et al.* Ab initio molecular simulations with numeric atom-centered orbitals. **Computer Physics Communications**, v. 180, n. 11, p. 2175 – 2196, 2009. ISSN 0010-4655.

BRUNETTO, G. *et al.* Nonzero Gap Two-Dimensional Carbon Allotrope from Porous Graphene. **Physical Chemistry Chemical Physics**, v. 116, n. 23, p. 12810–12813, jun 2012. ISSN 1932-7447.

BUNCH, J. S. *et al.* Impermeable atomic membranes from graphene sheets. **Nano Letters**, ACS Publications, v. 8, n. 8, p. 2458–2462, 2008.

CHAI, J.-D.; HEAD-GORDON, M. Long-range corrected hybrid density functionals with damped atom-atom dispersion corrections. **Physical Chemistry Chemical Physics**, The Royal Society of Chemistry, v. 10, p. 6615–6620, 2008.

CRAMER, C. J. **Essentials of Computational Chemistry: Theories and Models**. 2. ed. New Jersey, USA: John Wiley & Sons, 2004.

DUIJNEVELDT, F. B. van *et al.* State of the art in counterpoise theory. **Chemical Reviews**, v. 94, n. 7, p. 1873–1885, 1994.

FISCHBEIN, M. D.; DRNDIĆ, M. Electron beam nanosculpting of suspended graphene sheets. **Applied Physics Letters**, AIP, v. 93, n. 11, p. 113107, 2008.

GRIMME, S. Semiempirical hybrid density functional with perturbative second-order correlation. **The Journal of Chemical Physics**, v. 124, n. 3, p. 034108, 2006.

- GRIMME, S. Density functional theory with London dispersion corrections. **Wiley Interdisciplinary Reviews: Computational Molecular Science**, John Wiley & Sons, Inc., v. 1, n. 2, p. 211–228, mar 2011.
- HELGAKER, T. *et al.* **Molecular Electronic Structure Theory**. New Jersey, USA: John Wiley & Sons, 2004.
- HOHENBERG, P.; KOHN, W. Inhomogeneous electron gas. **Physical Review**, American Physical Society, v. 136, p. B864–B871, Nov 1964.
- JEZIORSKI, B. *et al.* Perturbation Theory Approach to Intermolecular Potential Energy Surfaces of van der Waals Complexes. **Chemical Reviews**, v. 94, n. 7, p. 1887–1930, nov 1994. ISSN 0009-2665.
- JIANG, D.-e. *et al.* Porous Graphene as the Ultimate Membrane for Gas Separation. **Nano Letters**, v. 9, n. 12, p. 4019–4024, 2009. ISSN 1530-6984.
- JIAO, S.; XU, Z. Selective Gas Diffusion in Graphene Oxides Membranes: A Molecular Dynamics Simulations Study. **ACS Applied Materials and Interfaces**, v. 7, n. 17, p. 9052–9059, may 2015. ISSN 1944-8244.
- JIAO, Y. *et al.* Graphdiyne: a versatile nanomaterial for electronics and hydrogen purification. **Chemical Communications**, v. 47, n. 43, p. 11843, 2011. ISSN 1359-7345.
- JIAO, Y. *et al.* Modelling carbon membranes for gas and isotope separation. **Physical Chemistry Chemical Physics**, v. 15, n. 14, p. 4832, 2013. ISSN 1463-9076.
- JOHNSON, E. R. *et al.* NCI : revealing non-covalent interactions. **Journal of American Chemical Society**, v. 132, n. 18, p. 6498–6506, 2010. ISSN 0002-7863.
- KOHN, W.; SHAM, L. J. Self-consistent equations including exchange and correlation effects. **Physical Review**, American Physical Society, v. 140, p. A1133–A1138, Nov 1965.
- LEE, C. *et al.* Development of the Colle-Salvetti Correlation-Energy Formula into a Functional of the Electron Density. **Physical Review B**, v. 37, p. 785–789, jan. 1988.
- LEENAERTS, O. *et al.* Graphene: A perfect nanoballoon. **Applied Physics Letters**, v. 93, n. 19, p. 10–13, 2008. ISSN 00036951.
- LI, G. *et al.* Architecture of graphdiyne nanoscale films. **Chemical Communications**, The Royal Society of Chemistry, v. 46, p. 3256–3258, 2010.
- LI, Y. *et al.* Two-Dimensional Polyphenylene: Experimentally Available Porous Graphene as a Hydrogen Purification Membrane. **Chemical Communications**, v. 46, n. 21, p. 3672, 2010. ISSN 1359-7345.
- LIBRETEXTS. **The Electromagnetic Spectrum**. 2018. [https://chem.libretexts.org/Textbook_Maps/Physical_and_Theoretical_Chemistry_Textbook_Maps/Map%3A_Physical_Chemistry_\(McQuarrie_and_Simon\)/13%3A_Molecular_Spectroscopy/13-01._Different_Regions_of_the_Electromagnetic_Spectrum_Are_Used_to_Investigate_Different_Molecular_Processes](https://chem.libretexts.org/Textbook_Maps/Physical_and_Theoretical_Chemistry_Textbook_Maps/Map%3A_Physical_Chemistry_(McQuarrie_and_Simon)/13%3A_Molecular_Spectroscopy/13-01._Different_Regions_of_the_Electromagnetic_Spectrum_Are_Used_to_Investigate_Different_Molecular_Processes). Accessed: 2018-06-02.

- LIN, Y. S. *et al.* Long-Range Corrected Hybrid Density Functionals with Improved Dispersion Corrections. **Journal of Chemical Theory and Computation**, v. 9, n. 1, p. 263–272, jan 2013. ISSN 15499618.
- LIU, H. *et al.* Selectivity trend of gas separation through nanoporous graphene. **Journal of Solid State Chemistry**, Elsevier, v. 224, p. 2–6, 2015. ISSN 1095726X.
- LU, T.; CHEN, F. Multiwfn: A multifunctional wavefunction analyzer. **Journal of Computational Chemistry**, v. 33, n. 5, p. 580–592, 2012. ISSN 01928651.
- MA, Z. *et al.* Computational prediction of experimentally possible g-C₃N₃ monolayer as hydrogen purification membrane. **International Journal of Hydrogen Energy**, Elsevier Ltd, v. 39, n. 10, p. 5037–5042, 2014. ISSN 03603199.
- MARUYAMA, M.; OKADA, S. Two-Dimensional sp² Carbon Network of Fused Pentagons: All Carbon Ferromagnetic Sheet. **Applied Physics Express**, v. 6, n. 9, p. 095101, sep 2013. ISSN 1882-0778.
- MENG, Z. *et al.* Graphdiyne as a High-Efficiency Membrane for Separating Oxygen from Harmful Gases: A First-Principles Study. **ACS Applied Materials and Interfaces**, v. 8, n. 41, p. 28166–28170, 2016. ISSN 19448252.
- MØLLER, C.; PLESSET, M. S. Note on an Approximation Treatment for Many-Electron Systems. **Physical Review**, v. 46, p. 618–622, out. 1934.
- NEESE, F. Software Update: the ORCA Program System, Version 4.0. **Wiley Interdisciplinary Reviews: Computational Molecular Science**, v. 8, n. 1, p. e1327, jan 2018. ISSN 17590876.
- OYAMA, S. *et al.* Theory of hydrogen permeability in nonporous silica membranes. **Journal of Membrane Science**, v. 244, n. 1-2, p. 45–53, nov 2004. ISSN 03767388.
- PAPAJAK, E.; TRUHLAR, D. G. Convergent partially augmented basis sets for post-hartree-fock calculations of molecular properties and reaction barrier heights. **Journal of Chemical Theory and Computation**, v. 7, n. 1, p. 10–18, 2011.
- PARKER, T. M. *et al.* Levels of Symmetry-Adapted Perturbation Theory (SAPT). I. Efficiency and Performance for Interaction Energies. **The Journal of Chemical Physics**, v. 140, n. 9, p. 094106, mar 2014. ISSN 1089-7690.
- PARRISH, R. M. *et al.* Psi4 1.1: An open-source electronic structure program emphasizing automation, advanced libraries, and interoperability. **Journal of Chemical Theory and Computation**, v. 13, n. 7, p. 3185–3197, jul 2017. ISSN 1549-9618.
- PERDEW, J. P. *et al.* Generalized gradient approximation made simple. **Physical Review Letters**, American Physical Society, v. 77, p. 3865–3868, Oct 1996.
- PERDEW, J. P. *et al.* Rationale for Mixing Exact Exchange with Density Functional Approximations. **The Journal of Chemical Physics**, v. 105, p. 9982–9985, dez. 1996.
- PERDEW, J. P. *et al.* Prescription for the design and selection of density functional approximations: More constraint satisfaction with fewer fits. **The Journal of Chemical Physics**, v. 123, n. 6, p. 062201, 2005.

- QU, Y. *et al.* Efficient hydrogen isotopologues separation through a tunable potential barrier: The case of a C₂N membrane. **Scientific Reports**, Springer US, v. 7, n. 1, p. 1–7, 2017. ISSN 20452322.
- ROCHELLE, G. T. Amine Scrubbing for CO₂ Capture. **Science**, v. 325, n. 5948, p. 1652–1654, sep 2009. ISSN 0036-8075.
- SAVIN, A. *et al.* ELF: The Electron Localization Function. **Angewandte Chemie International Edition**, v. 36, n. 17, p. 1808–1832, 1997. ISSN 05700833.
- SCHRIER, J. Helium separation using porous graphene membranes. **Journal of Physical Chemistry Letters**, v. 1, n. 15, p. 2284–2287, aug 2010. ISSN 19487185.
- SINT, K. *et al.* Selective Ion Passage through Functionalized Graphene Nanopores. **Journal of American Chemical Society**, American Chemical Society, v. 130, n. 49, p. 16448–16449, dec 2008. ISSN 0002-7863.
- SMITH, D. G. A. *et al.* Revised damping parameters for the d₃ dispersion correction to density functional theory. **The Journal of Physical Chemistry Letters**, v. 7, n. 12, p. 2197–2203, 2016.
- SUK, M. E.; ALURU, N. R. Water Transport through Ultrathin Graphene. **Journal of Physical Chemistry Letters**, v. 1, n. 10, p. 1590–1594, may 2010. ISSN 1948-7185.
- SZABO, A.; OSTLUND, N. S. **Modern Quantum Chemistry: Introduction to Advanced Electronic Structure Theory**. New York, USA: Dover Publications, 1996.
- TANG, Q. *et al.* Graphene-related nanomaterials: tuning properties by functionalization. **Nanoscale**, v. 5, n. 11, p. 4541, 2013. ISSN 2040-3364.
- TAO, Y. *et al.* Tunable Hydrogen Separation in Porous Graphene Membrane: First-Principle and Molecular Dynamic Simulation. **ACS Applied Materials and Interfaces**, v. 6, n. 11, p. 8048–8058, 2014. ISSN 19448252.
- TKATCHENKO, A. *et al.* Accurate and efficient method for many-body van der waals interactions. **Physical Review Letters**, American Physical Society, v. 108, p. 236402, Jun 2012.
- TKATCHENKO, A.; SCHEFFLER, M. Accurate molecular van der waals interactions from ground-state electron density and free-atom reference data. **Physical Review Letters**, American Physical Society, v. 102, p. 073005, Feb 2009.
- WANG, X. *et al.* Heteroatom-doped graphene materials: syntheses, properties and applications. **Chem. Soc. Rev.**, Royal Society of Chemistry, v. 43, n. 20, p. 7067–7098, 2014. ISSN 0306-0012.
- WANG, Y. *et al.* Two-Dimensional Covalent Triazine Framework Membrane for Helium Separation and Hydrogen Purification. **ACS Applied Materials and Interfaces**, v. 8, n. 13, p. 8694–8701, apr 2016. ISSN 19448252.
- WANG, Y. *et al.* Exploration of nanoporous graphene membranes for the separation of N₂ from CO₂ : a multi-scale computational study. **Physical Chemistry Chemical Physics**, Royal Society of Chemistry, v. 18, n. 12, p. 8352–8358, 2016. ISSN 1463-9076.

WANG, Y. *et al.* Theoretical investigation of gas separation in functionalized nanoporous graphene membranes. **Applied Surface Science**, Elsevier B.V., v. 407, p. 532–539, 2017. ISSN 01694332.

WEIGEND, F.; AHLRICHS, R. Balanced Basis Sets of Split Valence, Triple Zeta Valence and Quadruple Zeta Valence Quality for H to Rn: Design and Assessment of Accuracy. **Physical Chemistry Chemical Physics**, v. 7, n. 18, p. 3297–3305, 2005. ISSN 1463-9076.

YANG, Y. *et al.* Tunable C₂N Membrane for High Efficient Water Desalination. **Scientific Reports**, Nature Publishing Group, v. 6, n. 1, p. 29218, 2016. ISSN 2045-2322.

ZHANG, H. *et al.* Tunable Hydrogen Separation in sp-sp² Hybridized Carbon Membranes: A First-Principles Prediction. **Journal of Physical Chemistry C**, v. 116, n. 31, p. 16634–16638, aug 2012. ISSN 1932-7447.

ZHU, L. *et al.* C₂N: an excellent two-dimensional monolayer membrane for He separation. **Journal of Materials Chemistry A**, Royal Society of Chemistry, v. 3, n. 42, p. 21351–21356, 2015. ISSN 2050-7488.

ZHU, L. *et al.* Theoretical Prediction of Hydrogen Separation Performance of Two-Dimensional Carbon Network of Fused Pentagon. **ACS Applied Materials and Interfaces**, v. 7, n. 51, p. 28502–28507, 2015. ISSN 19448252.

ZHU, Z. Permeance Should Be Used to Characterize the Productivity of a Polymeric Gas Separation Membrane. **Journal of Membrane Science**, v. 281, n. 1-2, p. 754–756, sep 2006. ISSN 03767388.

Annex A - Published Works

1. CARDOSO, D. V. V., CUNHA, L. A., SPADA, R. F. K., FERRAO, L. F. A., ROBERTO-NETO, O., MACHADO, F. B. C., Thermochemical and kinetics studies of the $\text{CH}_3\text{SH} + \text{S} (^3\text{P})$ hydrogen abstraction and insertion reactions, **Journal of Molecular Modeling**, v. 20, n. 9, p. 2449, 2014, ISSN 1610-2940.
2. CARDOSO, D. V. V., CUNHA, L. A., SPADA, R. F. K., PETTY, C. A., FERRAO, L. F. A., ROBERTO-NETO, O., MACHADO, F. B. C., Thermochemical and Kinetics of $\text{CH}_3\text{SH} + \text{H}$ Reactions: The Sensitivity of Coupling the Low and High-Level Methodologies, **Journal of Physical Chemistry A**, v. 121, n. 2, p. 419-428, 2017.
3. MOURA, S. L., FAJARDO, L. M., CUNHA, L. A., SOTOMAYOR, M. P. T., MACHADO, F. B. C., FERRAO, L. F. A., PIVIDORI, M. I., Theoretical and experimental study for the biomimetic recognition of levothyroxine hormone on magnetic molecularly imprinted polymer, **Biosensors and Bioelectronics**, v. 107, p. 203-210, 2018, ISSN 0956-5663.
4. CUNHA, L. A., FERRAO, L. F. A., MACHADO, F. B. C., PINHEIRO JR, M., On the importance of non-covalent interactions for porous membranes: unraveling the role of pore size, 2018 (Submitted).

FOLHA DE REGISTRO DO DOCUMENTO

| | | | |
|---|--------------------------------|---|-------------------------|
| 1. CLASSIFICAÇÃO/TIPO DM | 2. DATA 04 de julho de 2018 | 3. DOCUMENTO Nº DCTA/ITA/DM-038/2018 | 4. Nº DE PÁGINAS 101 |
| 5. TÍTULO E SUBTÍTULO: Intermolecular Interactions in Molecular Models of Porous Graphene: Insights on Permeability and Selectivity | | | |
| 6. AUTOR(ES): Leonardo dos Anjos Cunha | | | |
| 7. INSTITUIÇÃO(ÕES)/ÓRGÃO(S) INTERNO(S)/DIVISÃO(ÕES): Instituto Tecnológico de Aeronáutica – ITA | | | |
| 8. PALAVRAS-CHAVE SUGERIDAS PELO AUTOR: Grafeno; Forças Intermoleculares; Permeabilidade; Seletividade; Estruturas bidimensionais; Físico-Química; Física | | | |
| 9. PALAVRAS-CHAVE RESULTANTES DE INDEXAÇÃO: Grafeno; Forças Intermoleculares; Permeabilidade; Estruturas bidimensionais; Físico-Química; Física | | | |
| 10. APRESENTAÇÃO: <input checked="" type="checkbox"/> Nacional <input type="checkbox"/> Internacional ITA, São José dos Campos. Curso de Mestrado. Programa de Pós-Graduação em Física. Área de Física Atômica e Molecular. Orientador: Francisco Bolivar Correto Machado; coorientador: José Maximiano Pinheiro Júnior. Defesa em 20/06/2018. Publicada em 2018. | | | |
| 11. RESUMO: Molecular engineering of porous membranes represents the frontier technology in gas separation processes. Owing to its intrinsic single-atomic layer thickness, nanoporous graphene allotropes are a promising class of compounds that fits the requirements for enhanced permeance and selectivity properties towards an specific target. Issues such as control of chemical stability and homogeneity of pore size and density grant an increasing central role to molecular modeling tools to guide the development of more efficient nanoporous devices. Previous works have provided some insight on possible strategies to devise pore structures for specific purposes. Their strategy, despite exploring different aspects such as structural changes, topological modification and functionalization, relied mostly on the influence of an ambiguous definition of pore size. The main goal of this master dissertation is to shed light into the nature of the diffusion mechanism and, more importantly, understand and quantify the influence of pore size in this process. The novelty of this work relies on the physical decomposition of the total interaction energy between gas molecules and molecular pore structures. To this end, the Symmetry-Adapted Perturbation Theory (SAPT) methodology was explored. Based on this analysis, effects such as electron delocalization, charge distribution and polarization could contribute towards a mechanism that counterbalances the influence of the pore size. A second part of the study consisted on a comparative analysis between SAPT results and energy barriers computed at the density functional theory level. To this end, we have explored the interaction between a pore size and several gas molecules. It is interesting to notice that, for some systems, mixing of orbitals of each monomer might lead to unexpected results due to charge-transfer effects. Finally, we have also applied SAPT to explore the effects of chemical doping as a strategy for tailoring the total interaction energy. The set of presented analysis aims to provide a meaningful picture posed by the diffusion process, emphasizing the importance of energy decomposition analysis (EDA) methods in order to comprehend such mechanism. The set of investigations present in this work provides a conceptual basis to understand the complex set of intermolecular interactions involved in the sieving process which is essential to promote new guidelines for a rational design of efficient molecular sieves. | | | |
| 12. GRAU DE SIGILO: <input checked="" type="checkbox"/> OSTENSIVO <input type="checkbox"/> RESERVADO <input type="checkbox"/> SECRETO | | | |